LARGE PLASTIC DEFORMATION AND SHEAR LOCALIZATION OF CRYSTALS

Written by

Awni Abu-Saman

Supervised by
J. Ronda, D.Sc.

October, 2000

Thesis submitted for the Degree of Ph.D.

Department of Mathematics and Applied Mathematics
University of Cape Town
Private bag, Rondebosch 7701.

ACKNOWLEDGMENTS

This work was done under the supervision of Jacek Ronda (D.Sc.) whom I would like to thank for his guidance, suggestions and support during the research.

I would like gratefully acknowledge a support provided from the FRD/UCT Center for Research in Computational and Applied mechanics (CERECAM) for funding part of this research and for making the computational facilities available. In this regard I would like to express my gratitude to Prof. J. B. Martin, Prof. B. D. Reddy, and Mr. Shaun Courtney.

I would like to thank the UCT for funding a part of this research.

I would like also thank Prof. R. B. Pecherski from the Polish Academy of Sciences for cooperation and providing papers and data for numerical simulation.

I'm also gratefully acknowledging the assistance and help from M.Sc. Graeme J. Oliver and M.Sc. Belete Chernet, my colleagues from the Department of Mathematics and Applied Mathematics.

I would like to thank my parents for their unlimited support. I like to thank my wife Manal and my sons for their patience, cooperation and support during the research. I also like to thank my friends from the Department of Mathematics and Applied Mathematics Arthur Phaswana, Justin Munganga, and Andre Botma for their support and for making my stay in the department more easy and educational.

ABSTRACT

This thesis is an attempt to study single crystals deformation and the implication of shear banding in single crystals.

Taylor's type rate dependent model developed by Peirce and Asaro is used to simulate shear localization of face centered cubic (fcc) and body centered cubic (bcc) metals deforming by crystallographic slip over crystallographic slip systems. This is associated with Peirce's forward gradient semi-implicit time dependent integration scheme.

Localized deformations of rate dependent single crystals subject to plane strain compression analyzed numerically. The crystal geometry is idealized in terms of a planar double model. Two crystal geometries are modeled. One is a planar model of an (fcc) crystal undergoing primary-conjugate slip. The second geometry models a (bcc) crystal.

The extremal surface phenomenological model for describing large plastic deformations, that has been developed recently by Pecherski, is also considered here for application to simulate large plastic strain effects and shear localization in crystals. This model is based on the mechanism of crystallographic slip and micro-shear banding by means of a double shearing system, where an additional double-shearing system is used to approximate the effect of active micro-shear bands. A time independent scheme with internal variables has been developed for integrating the constitutive equations.

The material models have been implemented into the finite element software ABAQUS, where specific user material subroutines "UMAT" have been written to integrate the constitutive equations. The material model implementation is based on the implicit solution of stress-strain relations. The tangent moduli of the constitutive equations are consistent with the integration scheme. Numerical results of rate dependent and extremal surface models are analyzed and compared.

The results for the rate dependent constitutive relations show that the initial orientation, the geometry, and the strain rate sensitivity of the crystal influence both the onset of shear band formation and orientation of the bands. It appears from the finite element computations for the extremal surface model that the model predicts localized plastic deformation at the appropriate strain levels and orientations.

TABLE OF CONTENTS

CHAPTER ONE 1
INTRODUCTION 1

CHAPTER TWO
CRYSTALLITE DEFORMATION 7
2.1 Introduction 7
2.2 Sliding 8
2.3 Dislocations 12
2.4 Mechanisms of Plastic Deformation 15
2.5 Deformation Texture 17
2.6 Shear Bands 19

CHAPTER THREE
MATERIAL RATE DEPENDENT MODEL 22
3.1 Introduction 22
3.2 Material Modeling 22
3.3 Evaluation of Resolved Shear Stress 27
3.4 Method of Solution to the Finite Element Equation 30

CHAPTER FOUR
EXTREMAL SURFACE PHENOMENOLOGICAL MODEL 31
4.1 Introduction 31
4.2 Basic Notations 32
4.3 Basic Constitutive Equations 32
4.4 Finite Element Formulation 35
4.4.1 Algorithm of Evaluation of the Equivalent Plastic Strain 35
4.4.2 Evaluation of the Tangent Moduli 39

CHAPTER FIVE
RESULTS OF FE SIMULATIONS 42
5.1 Introduction 42
5.2 Plane strain compression of Al-Cu fcc and bcc single crystals. 42
5.3 Channel Die compression of a copper single crystal. 65

CHAPTER SIX
CONCLUSIONS 78

APPENDIX A
CRYSTALLITE SLIP SYSTEMS. 81

APPENDIX B
MATRIX AND VECTOR REPRESENTATIONS OF TENSORS 85

BIBLIOGRAPHY 87

LIST OF FIGURES

FIGURE	PAGE
Fig. 2.1 Sliding over a certain slip system in the direction indicated by the arrow.	9
Fig. 2.2 Schematic diagram of glide occurring in the direction **e** in a cylinder shape crystal.	9
Fig. 2.3 Gliding on planes $\{1\bar{1}0\}$, $\{2\bar{3}1\}$, $\{1\bar{2}1\}$ in the slip direction <111>.	10
Fig. 2.4 Slip in the positive direction along the system (**m, n**).	10
Fig 2.5 Schematics showing a primary and a conjugate slip planes (a) The idealized model. (b) The real three-dimensional geometry. (c) The plane geometry.	11
Fig. 2.6 An axial force **F** applied to a crystal of cross section area A.	12
Fig. 2.7a Edge dislocation in an elastic block.	13
Fig. 2.7.b Screw dislocation in an elastic block.	13
Fig. 2.8 Dislocation loop.	14
Fig. 2.9 Screw part $\mathbf{b}_s$ and the edge part $\mathbf{b}_e$ of Burgers vector **b** at an arbitrary place of the dislocation loop.	14
Fig. 4.1 Geometry shows the double shear system in the extremal surface model.	33
Fig. 4.2(a) The closest-point projection of the pivot stress onto a yield surface in the case of nonlinear kinematics hardening	36
Fig. 4.2(b) The closest-point projection of pivot stress onto the yield surface in the case of nonlinear isotropic hardening.	36
Fig.5.1 The initial lattice orientation of an Al-Cu (fcc) single crystal model.	43
Fig. 5.2 The boundary conditions applied to the Al-Cu single crystal model.	43

Fig.5.3 Deformed meshes from the finite element calculation of the (fcc) crystal for the rate dependent model. (a) ε_{22}=0.0, (b) ε_{22}=0.083, (c) ε_{22}=0.108, (d) ε_{22}=0.156. 47

Fig. 5.4 (a) Contours of accumulated slip; (b) contours of equivalent strain; (c) contours of lattice rotations; (d) contours of the von Mises stress, for the strain value ε_{22}=0.083 for an Al-Cu (fcc) deformed crystal shown in Fig. 5.3(b) for the rate dependent model. 48

Fig. 5.5 (a) Contours of accumulated slip; (b) contours of equivalent strain; (c) contours of lattice rotations; (d) contours of the von Mises stress, for the strain value ε_{22}=0.108 for an Al-Cu (fcc) deformed crystal shown in Fig. 5.3(c) for the rate dependent model. 49

Fig. 5.6 Contours of accumulated slip; (b) contours of equivalent strain; (c) contours of lattice rotations; (d) contours of the von Mises stress for the strain value ε_{22}=0.156 for an Al-Cu (fcc) deformed crystal shown in Fig. 5.3(d) for the rate dependent model. 50

Fig. 5.7 Deformed finite element meshes for the (bcc) crystal for the rate dependent model. (a) ε_{22}=0.083, (b) ε_{22}=0.108, (c) ε_{22}=0.156, (d) ε_{22}=0.26. 53

Fig. 5.8 (a) Contours of accumulated slip; (b) contours of equivalent strain; (c) contours of lattice rotations; (d) contours of the von Mises stress, for the strain value ε_{22}=0.083 for the (bcc) deformed crystal shown in Fig. 5.7(a) for the rate dependent model. 54

Fig. 5.9 (a) Contours of accumulated slip; (b) contours of equivalent strain; (c) contours of lattice rotations; (d) contours of the von Mises stress. for the strain value ε_{22}=0.108 for the (bcc) deformed crystal shown in Fig. 5.7(b) for the rate dependent model. 49

Fig. 5.10 (a) Contours of accumulated slip; (b) contours of equivalent strain; (c) contours of lattice rotations; (d) contours of the von Mises stress, for the strain value ε_{22}=0.156 of the (bcc) deformed crystal shown in Fig. 5.7(c) for the rate dependent model. 56

Fig. 5.11(a) Contours of accumulated slip; (b) contours of equivalent strain; (c) contours of lattice rotations; (d) contours of the von Mises stress, for the strain value ε_{22}= 0.26 of the (bcc) deformed crystal shown in Fig. 5.7(d) for the rate dependent model. 57

Fig. 5.12 Deformed finite element meshes of Al-Cu crystal for the extremal surface model. (a) ε_{22}=0.083, (b) ε_{22}=0.108, (c) ε_{22}=0.156, (d) ε_{22}=0.26. 60

Fig. 5.13 (a) Contours of accumulated slip; (b) contours of equivalent strain; (c) contours of nett fraction; (d) contours of the von Mises stress, for the strain value ε_{22}=0.083 for an Al-Cu (fcc) deformed crystal shown in Fig. 5.12(a) for the extremal surface model. 61

Fig. 5.14(a) Contours of accumulated slip; (b) contours of equivalent strain; (c) contours of nett fraction; (d) contours of the von Mises stress, for the strain value ε_{22}=0.108 for an Al-Cu (fcc) deformed crystal shown in Fig. 5.12(b) for the extremal surface model. 62

Fig. 5.15(a) Contours of accumulated slip; (b) contours of equivalent strain; (c) contours of nett fraction; (d) contours of the von Mises stress, for the strain value ε_{22}=0.156 for the Al-Cu (fcc) deformed crystal shown in Fig. 5.12(c) for the extremal surface model. 63

Fig. 5.16 (a) Contours of accumulated slip; (b) contours of equivalent strain; (c) contours of nett fraction; (d) contours of the von Mises stress, for the strain value ε_{22}= 0.26 for an Al-Cu (fcc) deformed crystal shown in Fig. 5.12(d) for the extremal surface model. 64

Fig. 5.17 A copper single crystal in the channel die. 66

Fig. 5.18 Boundary conditions applied to the copper single crystal deformed in a channel die. 66

Fig. 5.19 The initial lattice orientation for a copper single crystal. 67

Fig. 5.20 Deformed finite element meshes for a copper single crystal for the rate dependent model. (a) ε_{22}=0.00, (b) ε_{22}=0.164, (c) ε_{22}= 0.255, (d) ε_{22}=0.58. 69

Fig. 5.21 (a) Contours of accumulated slip; (b) contours of equivalent strain; (c) contours of lattice rotations for the strain ε_{22}=0.164 for a deformed copper crystal shown in Fig. 5.20(b) for the rate dependent model. 70

Fig. 5.22 (a) Contours of accumulated slip; (b) contours of equivalent strain; (c) contours of lattice rotations for the strain ε_{22}=0.255 for a deformed copper crystal shown in Fig. 5.20(c) for the rate dependent model. 71

Fig. 5.23 (a) Contours of accumulated slip; (b) contours of equivalent strain; (c) contours of lattice rotations for the strain ε_{22}= 0.58 for a deformed copper crystal shown in Fig. 5.20(d) for the rate dependent model. 72

the rate dependent model. 72

Fig. 5.24 Deformed finite element meshes for a copper single crystal for the extremal surface model, for various values of strain (a) ε_{22}=0.164, (b) ε_{22}=0.255, (c) ε_{22}=0.58. 74

Fig. 5.25 (a) Contours of accumulated slip; (b) contours of equivalent strain; (c) contours of nett fraction for the strain ε_{22}=0.164 for a deformed copper crystal shown in Fig. 5.24(a) for the rate independent model. 75

Fig. 5.26 (a) Contours of accumulated slip; (b) contours of equivalent strain; (c) contours of nett fraction for the strain ε_{22}=0.255 for a deformed copper crystal shown in Fig. 5.24(b) for the rate independent model. 76

Fig. 5.27 (a) Contours of accumulated slip; (b) contours of equivalent strain; (c) contours of nett fraction for the strain ε_{22}=0.58 for a deformed copper crystal shown in Fig. 5.24(c) for the rate independent model. 77

Fig. A.1 Two slip directions $\mathbf{m}^i$ and slip plane normals $\mathbf{n}^i$ in the crystals idealized by two slip systems. 81

Fig. A.2 Examples showing lattice directions in a two-dimensional lattice. 82

Fig. A.3 The direction [*uvw*] in relation to its components along the crystallographic axis. 82

Fig. A.4 Plane (001) intercepts z-axis at unity and *x*-and *y*-axes at infinity. 83

Fig. A.5 Three-dimensional lattice, the (311) family of planes. 83

Fig A.6 Gliding of the (fcc) crystal on the crystallographic plane (111) in the <110> slip direction. 83

LIST OF TABLES

TABLE	PAGE
Table 2.1 Crystallographic indices	8
Table 3.1 Algorithm of the user subroutine UMAT in ABAQUS for the rate dependent model.	29
Table 4.1 Algorithm of evaluation of the equivalent plastic strain for the concept of kinematics of crystal deformation.	38
Table 4.2 Evaluation of $(\overset{**}{\gamma}\ \Delta t)$ for the extremal surface concept of crystal deformation	39
Table 5.1 Material elastic constants used for crystal simulations in terms of material yield limit τ_o.	43
Table 5.2 Material parameters for the Al-Cu (fcc) crystal simulation.	44
Table 5.3 The accumulated shear strain, the equivalent strain and the lattice rotation in the localized zone for various logarithmic strains of the Al-Cu (fcc) crystal using the rate dependent model.	45
Table 5.4 Material parameters for the (bcc) single crystal simulation.	51
Table 5.5 an accumulated shear strain, an equivalent strain and a lattice rotation in the shear band zone for various logarithmic strains of the bcc crystal simulation for the rate dependent model.	52
Table 5.6 an accumulated shear strain, an equivalent strain and the nett fraction in a shear band zone for various values of the strain for a single crystal simulation with the extremal surface model.	58
Table 5.7 Elasticity constants used for the simulation with copper single crystal.	65
Table 5.8 Material parameters for the copper single crystal simulation for the rate dependent constitutive material model.	67
Table A.1 Example of 12 {111}<110> (fcc) slip systems in terms of the rotation angle θ.	84

LIST OF SYMBOLS

- $\mathbf{m}$ Vector of a slip system direction,
- $\mathbf{n}$ Normal vector to a slip system direction,
- ρ Dislocation density,
- τ^{α} Critical resolved shear stress on slip system α,
- $\mathbf{F}$ Deformation gradient tensor,
- $\mathbf{E}$ Elastic part of the deformation gradient tensor,
- $\mathbf{P}$ Plastic part of the deformation gradient tensor,
- $\mathbf{L}$ Eulerian velocity gradient,
- $\mathbf{L}^{p}$ Plastic part of Eulerian velocity gradient,
- $\gamma^{\bullet\alpha}$ Rate of shearing on the specific slip system α,
- γ Accumulated plastic shearing,
- $\overset{\nabla}{\tau}$ Material rate of Kirchhoff stress.
- $\overset{\nabla^{*}}{\tau}$ Jaumann rate of Kirchhoff stress τ,
- g^{α} Current slip system strength or hardness of specific slip system α,
- $\dot{a}$ Reference shear rate representing the compressive strain rate,
- h_{o} Initial hardening rate,
- τ_{s} Saturation strength.
- $\mathbf{Q}$ Material rotation increment,
- $\mathbf{S}$ Deviatoric stress tensor,
- $\mathbf{E}$ Deviatoric strain tensor,
- $\mathbf{C}=C_{ijkl}$ Material elastic matrix,
- υ Poisson's ratio,
- G Shear modulus,
- $\bar{\mathbf{N}}$ Unit vector normal to a yield surface,
- f_{net}^{ms} Nett fraction parameter,
- $1=\delta_{ij}$ Second-rank identity tensor,
- $\otimes$ Outer product of two tensors,
- : Inner product or contraction of tensors.

CHAPTER ONE

INTRODUCTION

The main aim of this work is to study and implement models of large plastic deformations, that rigorously account for arbitrarily large strains and rotations of both the material and the lattice within individual grains. Special consideration will be given to the plastic rotation accompanying large plastic deformations, which are the main cause for the evolution of textures in polycrystalline materials and the formation of shear bands accompanying the large plastic deformations. Large plastic deformation means true strains above five percent, with no upper limit except the maximum strains that can be achieved in metal forming processes such as rolling and wire drawing at room temperature.

The most important kinematic assumption of the continuum theory of the large plastic deformations (the multiple decomposition of the deformation gradient, which leads in turn to the additivity of deformation rates) as in the case of classical plasticity, has been proposed by Kroener [52] on the basis of structural considerations. This has been incorporated by Lee [54]. During twenty years since this publication, many attempts have been made to justify this assumption and to construct on this basis the continuous plasticity of large deformations [20], [21], [22], [67], [77], [78], and [84]. Most of the work on phenomenological models up to date is done with the help of this assumption.

The assumption on multiplicative decomposition has led naturally to the problem of basic rotations (the orthogonal part of the plastic deformation gradient). Lubarda and Lee have proposed in [57] a kinematic way of calculation of this rotation by means of other kinematic quantities of the continuous model) at least under certain simplifying kinematic assumptions. This idea has been developed and culminated in the axiomatic formulation of Simo [86]. Simultaneously, Kratochvil [50], [51] has speculated on the macroscopic constitutive relation for those rotations. The phenomenological speculations have had a structural origin and have been connected with the appearance of evolution of microstructure in polycrystals. Similar propositions have been then made by Dafalias *et al.* [28], Dienes [30], Loret [56], Paulun and Pecherski [70], [71].

On the other hand, the presence of additional local degrees of freedom, following from plastic rotations, has led to models with certain fields such as directors. Green and Naghdi [35] have constructed for this reason a multipolar continuum with plastic behaviour, while the plastic continuum with directors has been proposed by Mandel [59].

Unfortunately, the phenomenological approach to the problem of large plastic deformations suffers not only from doubts concerning the kinematic foundations of the model, such as the assumption on the multiplicative decomposition. This approach has no thermodynamic foundations. The classical works of Hill and Rice [41], [42] have shown the role-played in plasticity by various potentials, which should have a thermodynamic origin. Kleiber *et al.* [46], Meixner [61] and others have tried to find this origin; however, the systematic thermodynamic approach up to the standards of modern continuum thermodynamics fails entirely. Some progress has been achieved only in the case of visco-plastic materials by Perzyna [77] and materials with internal variables by Beevers [16].

Changes of microstructure (in particular, the evolution of deformation textures) are not accounted for in the above mentioned models of large plastic deformations. A few attempts to construct a macroscopic constitutive relation for plastic rotations have not solved that problem either. However, for more than 70 years physicists are working on structural models of plastic deformations, which include plastic rotations in a very natural way. This type of modelling has started approximately in 1924 with works of Sachs [81], Taylor [89], [91] and Schmid [82]. Taylor and Quinney [88], [90], and Huber and Schmid [43] have made attempts to describe the behaviour of polycrystals by means of a certain volume averaging procedure.

The pioneer work by Taylor [92] initiated a study of preferred orientations taken by a crystallite through the deformation process and building structural models. The slip mechanism of some fcc materials, especially aluminium, was studied and few structural models [92], [91] were developed for large plastic deformation. Microstructural mechanisms of deformation operating on the grain level were also analyzed. This analysis helped to determine polycrystal behaviour through identifying polycrystal response with some appropriate average of the response of its constituent grains. This work produced useful insight into the progress in studying texture and polycrystal strain hardening behaviour. Taylor considered grains of polycrystals, which undergo about the same strain. In his formulation the selection of slip systems, required to produce an arbitrary strain increment, was not necessarily unique, and for fcc crystals with 12 common slip systems is generally non-unique. The lattice rotations depend on the choice of a slip system, and therefore the developing crystallographic textures are also non-unique. The problem arises from the fact that for the non-unique choice of active slip systems the constitutive stress-strain relation is also non-unique.

Taylor made a physically intuitive assumption that all possible combinations of active slip systems assure minimization of cumulative shears. He assumed that all slip systems are hardened equally and they have the same shear strength. Taylor's model is still the most important one in the description of metals, and quantities defined in his model still get attention in experimental and analytical investigations.

The disadvantage of structural models is that they are numerically expensive. They were for a long time not implemented numerically until the appearance of the new generation of fast computers.

Peirce *et al.* [74] developed rate independent analysis for non-uniform deformation modes in a ductile single crystal. His work is based on a rate independent constitutive model for crystallographic slip. Lattice kinematics was shown to be of particular importance in promoting non-uniform plastic flow. The problem of rate independent theories comes from the loss of uniqueness of a mode of slip that has a choice of actively yielding slip systems. This problem has a particular concern in rate independent crystalline plasticity, especially in texture analysis of polycrystals, where the specification of the slip mode is necessary in calculating rotations of a lattice and grain. Within the rate independent idealization of slip, the uniqueness of the choice of active slip systems depends on kinematics, crystal's strain hardening and stress state. The uniqueness is not guaranteed when more than five linearly independent slip systems are potentially active even for prescribed deformations. This agrees with [92], where Taylor noted that an increment of incompressible plastic strain requires five linearly independent slip systems, with more than five available slips. The kinematics of straining does not, in general, uniquely specify a particular set of slips. On the other hand, Wilkins [100] indicated that rate dependent formulation allows the unique determination of slipping rate on each slip system and relate slipping rates directly to the stress state.

In rate dependent formulations, proposed by Peirce and Asaro [75], [9], there is no division of slip systems into active and inactive sets. Instead, slip on all slip systems occurs at a rate, which depends on the current stress and hardening properties.

Asaro and Needleman [10] developed an elastic-plastic, rate dependent polycrystalline model for low temperatures in which crystallographic slip is the sole mechanism for the deformation within the individual crystals. They follow Taylor's concept [92] to predict the global response of a polycrystal and assume that all grains have equal volume, and that the deformation gradient within each grain has uniform value throughout the crystallite aggregate. Peirce, Asaro and Needleman [74], [75], [10] carried out experimental and computational work to study texture and shear band evolution in single and polycrystalline materials. They utilized the semi-implicit integration procedure [75], which is numerically expensive, especially when the actual three-dimensional crystal geometry is used.

Previous studies of plastic deformations indicate that for a variety of metals and alloys the initially quasi-homogeneous mode of plastic deformation is often replaced by inhomogeneous deformation involving some form of shear-banding. The study of shear bands indicated their importance and difficulty in understanding of shear band formation. Many analytical and numerical models have been employed to study shear band initiation [5], [11], [12], [14], [15], [17], [36], [72], [73], [74], [98]. One of the more difficult aspects of developing these models is the formulation of material constitutive relations, which adequately characterize behaviour of a material and permit plastic flow localization at realistic strain levels. Shear bands are an important feature of a deformed crystal structure and bear the major part of deformation process at large plastic strains. A variety of papers [29], [36], [72], [73] are devoted to the investigation of the structure of shear bands. However, little is known about the nature

of shear bands, especially about mechanisms of initiation and propagation [72]. A question of major importance is the relation between a crystal structure and mode of macroscopic shear bands and their precursors as well as the continuum plasticity used to discuss their overall geometry and significance in texture development.

Deve and Asaro in [29] stated that, in large plastic deformation of polycrystalline materials, shear bands play an important part in the deformation process and shear localization progressively replaces the current deformation process by slipping and/or twinning.

Asaro and Needleman [10] developed Taylor's model to study shear localization and textures in metals. Later Becker [13], [14], [15] used the same formulation as Asaro and Needleman [10] to define a constitutive behaviour of finite elements, assuming that a stiffness matrix for each element is determined by the average of stiffness matrices for eight crystal orientations. Becker [14], [15] has also carried out some calculations for a single crystal as well as for polycrystals with the full fcc crystal geometry of twelve slip systems. Becker applied the semi-implicit integration procedure, developed by Peirce [75]. Mathur and Dawson [60] used the Taylor-type model in a finite element analysis of a rolling process. However, the approach of Mathur and Dawson [60] is somewhat different in that they used an Eulerian finite element model and the effects of texture evolution were incorporated by an itterative process involving integration of the crystal model along streamlines.

Anand, Bronkhorst, and Kalidindi [5], [18] also used the Taylor-type model for large deformation polycrystalline plasticity to carry out some experimental and computational work to study evolution of texture and shear band formation in plain strain compression of initially isotropic copper. They used the actual slip system structure for fcc material. Their results of the finite element calculations are in much better agreement with experiments, but at a substantially higher computational expense. The capabilities of Taylor-type models were modified *via* the Ahzi, Asaro and Lee [3] description for aggregates of low symmetry materials (i.e., for crystal classes that have less than five independent slip systems).

Predictions from the polycrystals model of Asaro and Needleman [10] concerning the evolution of texture in simple shear of fcc polycrystals have been compared by Harren *et al.* [38] against the experimental work of Williams [102] on previously rolled copper. These authors have found that the first-order features of Williams [102] experimentally determined textures were captured by Asaro and Needleman [10] Taylor-type polycrystal model. Harren and Asaro [37] also attempt to evaluate the performance of the Taylor-type model of Asaro, Needleman and co-workers [75], but this time by comparison against finite element simulation of polycrystalline aggregates.

Tvergaard and Needleman [95] studied shear band localization using a band model involving polycrystalline aggregates; one representing the material inside the potential band and the other the material outside. They obtained the aggregate constitutive response from the generalized Taylor-type polycrystal model developed by Asaro and Needleman [10]. Needleman and Ortiz [65] found that grain boundaries in polycrystals could act as both barriers to, and source of, shear bands. Computational studies of crystal plasticity, material instabilities such as shear bands, and fracture

mechanisms have made major contributions to the current understanding of the mechanical behaviour of materials. Some of these accomplishments are documented in Ortiz [69] and Tvergaard [96].

Incorporation of a length scale is needed to predict shear bandwidth. This is of importance because the post-localization response is closely tied to the width of the localized region. Prediction of shear bandwidths has spawned a large literature on continuum theories that contain a length scale. Accounting for heat condition can introduce a length scale, e.g., Zhou *et al.* [108]. Strain gradient constitutive theories explicitly introduce a material parameter with the dimensions of length, e.g., [4], [104].

Zbib [103], [106] and Zhu *et al.* [107] addressed the issue of length scale associated with a number of small-scale phenomena in plasticity. The problem is formulated within two frameworks, a continuum (macro-scale) framework and dislocation (micro scale) framework. Within the theory of single crystal plasticity, the overall effect of dislocation glide is embedded into the model through a set of slip planes, defining the geometry of slip. However, the intensity of plastic deformation along each of the slip systems is viewed as an internal variable and modeled using a phenomenological theory. The theory has been employed by a number of investigations to examine various phenomena, In particular, shear banding in single crystals as well as polycrystals. In their analysis it was shown that the size of the shear band depends critically on the mesh size which is in agreement with results obtained by Deve and Asaro [29] and Watanabe [98]. The problem has been addressed by introducing strain gradient terms into the constitutive equations for the flow stress.

Pecherski's theoretical study [72], [73] on the basic physical mechanisms of micro-shear banding lead to a formulation of a phenomenological model of plastic flow accounting for micro-shear bands, and model the effect of micro-shear bands. He used the Huber-Mises yield criterion to approximate the extremal surface. A double-shearing system, normal to the flow plane, is used to represent contribution of active micro-shear bands. Pecherski in [72] proposed the nett fraction parameter to approximate the contribution of the shear bands in the plastic deformation process, and a crystalline parameter to approximate the mean orientation of micro-shear bands.

In this paper, mechanisms of large plastic deformation in metals are studied, in particular in fcc and bcc materials. The structural model proposed by Peirce and Asaro [75] is used to define the constitutive behaviour of the finite element assemblage to study shear localization and texture evolution in metals. The model proposed by Pecherski [72], based on the concept of a double shearing system, is studied. This model is associated with an internal variable numerical algorithm.

The second chapter is devoted to the description of the phenomenological background of the plastic deformation process. The basic factors, which play an important role in the deformation process of crystalline materials, are discussed. The basic notions related to the kinematics of sliding, dislocation, and some features of deformation textures are described. The plastic mechanisms are discussed and graphs illustrate the effect of these factors, and how they are related to the deformation process. Propagation and nature of shear bands are presented briefly.

The third chapter contains an extensive presentation of Taylor's rate type structural model, developed further by Peirce, Asaro and Needleman [10], [75] using Lee's decomposition of deformation gradient. In this model, slipping over slip systems is considered to be the sole mechanism of plastic deformation. The kinematics of a single crystal deformation is discussed together with the constitutive rate dependent equations and the kinematic hardening rule. The rate dependent model is implemented into ABAQUS [1], [2] as the User Material subroutine "UMAT" to observe the development of shear localization during compression process of Al-Cu and copper crystals. The "UMAT" subroutine allows the user to implement specific constitutive relations into ABAQUS.

The fourth chapter is devoted to study of a concept of shear banding. Pecherski's model of large plastic deformations, based on the mechanism of micro-shear banding with a double shearing system, is also implemented into ABAQUS as a UMAT subroutine using an internal variable algorithm. An additional double-shearing system is used to approximate the effect of active micro-shear bands.

The fifth chapter is devoted to presentation of numerical results. The rate dependent constitutive equations are used for simulation of a compression problem for a single fcc and bcc crystal with double slip systems, and different geometries. Results obtained by using the algorithm described in Chapter Four for integration of the extremal surface constitutive relations for single crystals are also shown there. Results obtained for Pecherski's extremal surface simulations are compared with those obtained for the rate dependent model.

CHAPTER TWO

CRYSTALLITE DEFORMATION

2.1 INTRODUCTION

The aim of this chapter is to describe the phenomenological background of the plastic deformation process. Basic concepts which play an important role in the plastic deformation process will be discussed together with the slip systems of crystals and the texture deformation of crystalline materials. The discussion and examples will be concentrated on fcc and bcc crystalline materials.

In the theory of large plastic deformations it is assumed that advanced deformations are produced by mechanism of crystallographic multiple slip. The Schmid law is used for assessment of the initiation of slip on a particular slip system. Sections 2.2 and 2.3 are devoted to explaining the process of dislocation sliding on slip systems. Microscopic properties of fcc lattice and basic notations used to denote the crystallographic slip systems are also described there.

Various processes occur in deformation of a crystalline body and thus a precise identification of a deformation process that can take place under particular conditions is important. Section 2.4 describes the characteristics of the various deformation processes, stress-strain curves of fcc crystalline materials, and types of hardening.

Section 2.5 describes deformation textures due to plastic deformation of a body. A definition of deformation textures is given together with a brief discussion of texture features.

Propagation of shear bands and its physical nature are described in Section 2.6. An overview of studies on shear localization in shear bands is given.

2.2 SLIDING

Metals deform plastically by a sliding process that was firstly discovered by Reusch in 1867. All crystals would yield plastically at a sufficiently high temperature [34]. Crystals of many metals, the alkali halides and some other non-metals such as graphite or crystals of inert gases yield plastically at very low temperature.

The constitutive framework that will be used to analyze the development of shear bands in Al-Cu and copper single crystals is a viscoplastic (or rate dependent plastic), finite strain, crystallographic slip theory. Within the single crystal framework, the plasticity is described solely by continuum shear flows that occur along the various slips systems of the crystal.

When large shear forces are applied to a crystal, it can yield in the plastic manner under the following conditions: such forces are large enough and applied long enough, then a crystal shape can alter permanently.

Definition 2.1: Sliding is defined as the translation of one part of a crystal with respect to other parts without any change in the volume of the crystal. It takes place in a particular direction on a specific crystallographic plane.

The orientation of crystal planes is known by their *Miller indices* [79], [97] which are defined as follows: To determine indices for the plane **P**, find its intercepts with the axes along the basis vectors $\boldsymbol{a}, \boldsymbol{b}$, and $\boldsymbol{c}$. Let these intercepts be x, y, and z. Usually x is fractional multiple of a, y a fractional multiple of b, and so forth. We form the fractional triplet

$$\left(\frac{x}{a}, \frac{y}{b}, \frac{z}{c}\right),$$

that can be inverted to the triplet

$$\left(\frac{a}{x}, \frac{b}{y}, \frac{c}{z}\right),$$

and then reduced to a similar one having the smallest integers by multipling by a common factor. This last set is called the *Miller indices* of the plane and is indicated by (hkl) (see Fig.(A.5) in Appendix **A**).

The basic notations used for crystallographic slip planes and directions are contained in Table 2.1.

Table 2.1 Crystallographic indices

crystallographic direction	[uvw]
symmetry related directions	<uvw>
plane	(hkl)
symmetry related plane	{hkl}

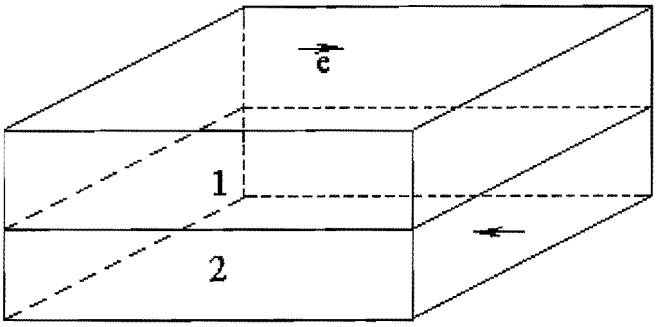

Fig. 2.1(a)

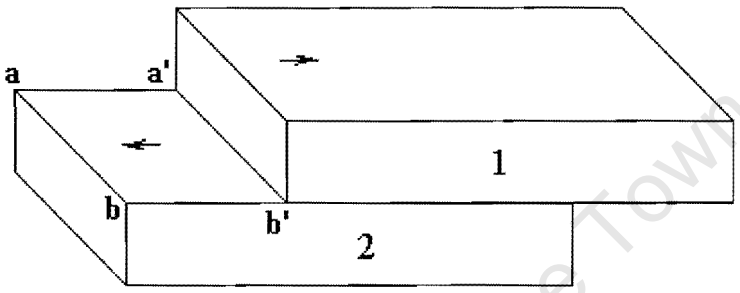

Figure 2.1(b) Sliding over a certain slip plane in the direction indicated by the arrow

The kinematics of sliding is shown in Figs.(2.1) and (2.2). The shape of a crystal can change but neither its volume nor the orientation of a crystal. The process of sliding produces steps on a crystal surface aa'b'b shown in Fig.(2.1(b)). These steps can be seen in optical microscope as slip lines.

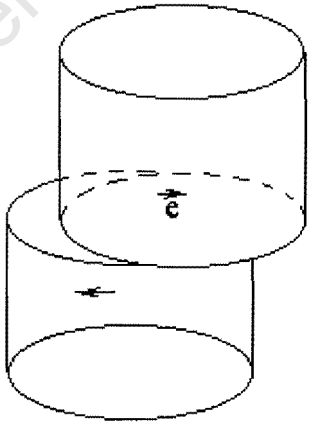

Figure 2.2 Schematic diagram of glide occurring in the direction **e** in a cylinder shape crystal.

Each slip system of the crystal is defined by the orthogonal pair of unit vectors (**m**,**n**), where **m** represents the slip direction, and **n** is the unit vector normal to the slip plane. The single slip system produces exactly the same deformation as slip on **-n** in the direction **-m**. Schematic diagram illustrating the different slip planes with their slip directions in a cubic crystal is shown in Fig.(2.3).

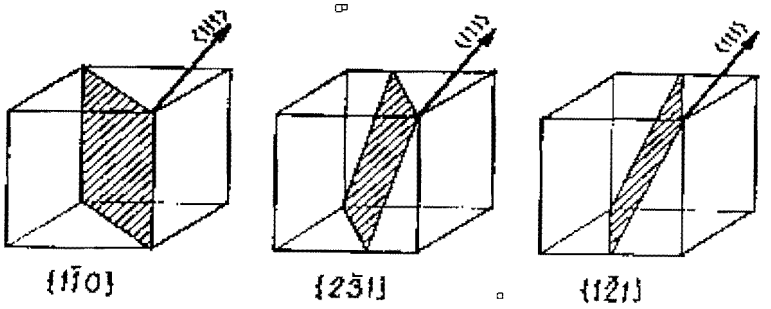

Figure 2.3 Gliding on planes $\{1\,\bar{1}\,0\}$, $\{2\,\bar{3}\,1\}$, $\{1\,\bar{2}\,1\}$ in the slip direction <111>.

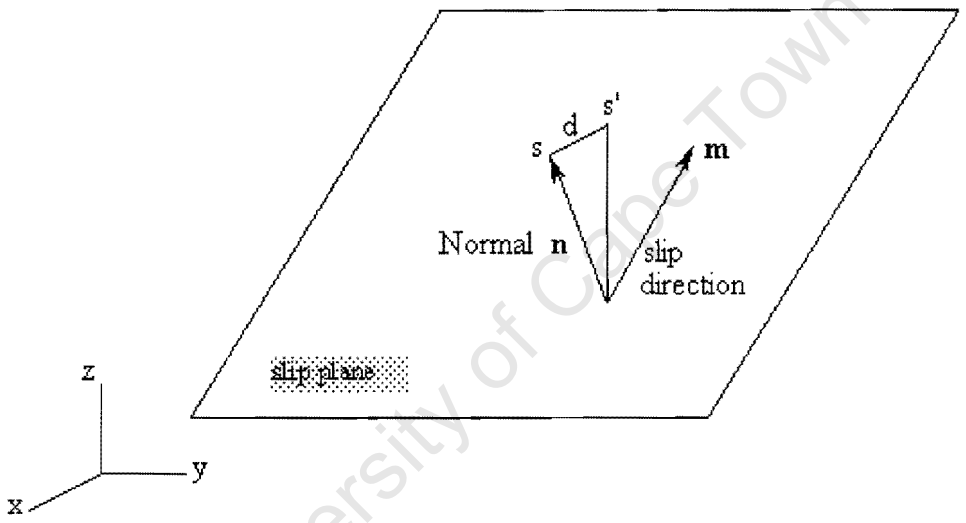

Figure 2.4 Slip in the positive direction on the system (**m**,**n**)

The slip system (**m**,**n**) in Fig.(2.4) is taken to be capable to operate in either a positive or negative sense so that on the plane of normal **n** slip can proceed in either the direction **m** or in the direction –**m**. The deformation produced by a slip in the direction **m** is just the reverse of that produced by a slip in the direction **-m**. In Asaro's [8] rate dependent formulation and computations, all slip systems are considered as potentially active as long as the resolved shear stress is greater than zero. It is neither necessary nor convenient to consider $(\mathbf{m}^\alpha, \mathbf{n}^\alpha)$ and $(-\mathbf{m}^\alpha, \mathbf{n}^\alpha)$ as separate slip systems on each of which only positive slip is allowed. Thus the corresponding plastic strain rate $\dot{\gamma}^\alpha$ will be negative only if the corresponding resolved shear stress τ^α on the slip system α is negative.

Carrying out the finite element calculations with the actual three-dimensional crystal geometry, with 12 slip systems for fcc crystals is time consuming and the computational expenses are high. The finite element studies in this dissertation are carried out using the model shown in Fig.(2.5(c)) that represents an idealized plane double slipping crystal. The geometry is chosen to represent the nearly symmetric primary-conjugate mode of slip that is typically predominant in deformed crystals. For the Al-Cu and copper crystals we take the angle from the tensile axis to be 30° to serve as fcc crystal model [79]. For the (bcc) crystal simulation, we assume the angle from the tensile axis to be 60° [79]. The actual geometry of primary-conjugate slip is shown in Fig.(2.5(b)). The planar model is less constrained than the actual three-dimensional crystal geometry.

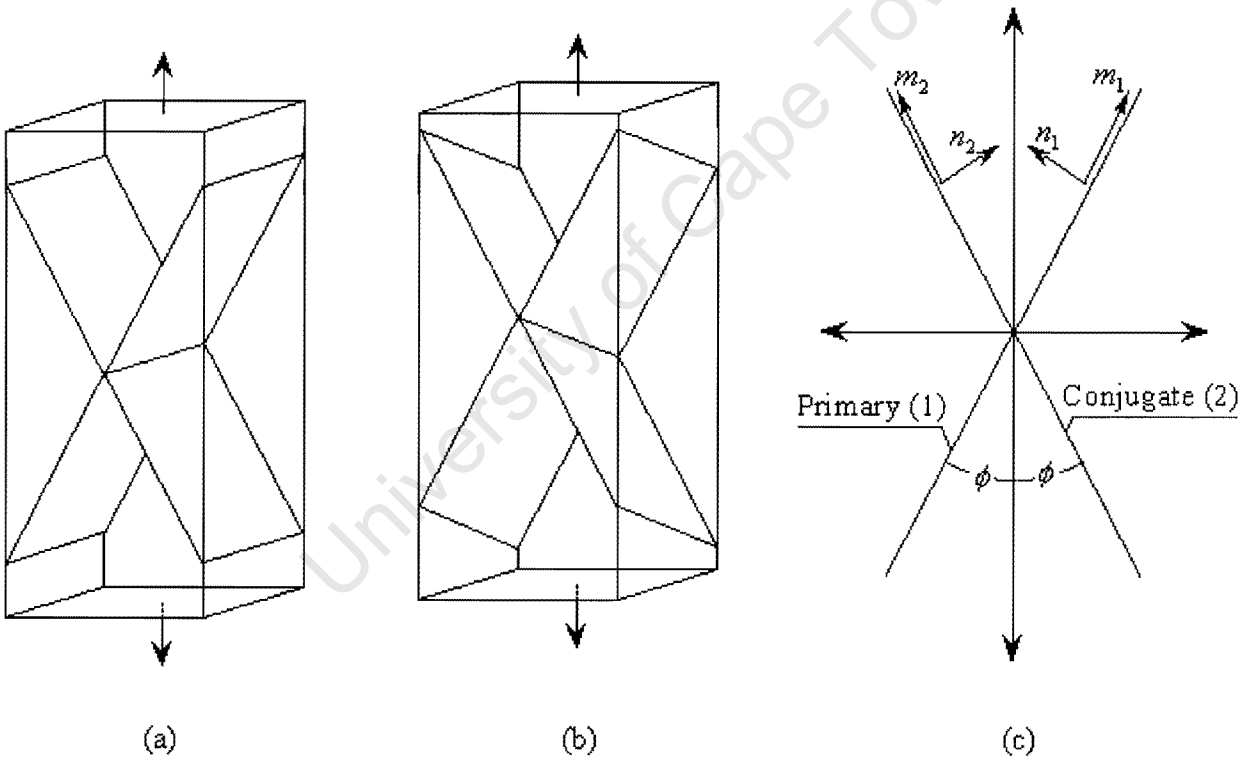

Figure 2.5 Schematics showing double conjugate slip planes (a) The idealized model. (b) The real three-dimensional geometry. (c) The plane geometry.

The critical stress for initiation of slip on a particular slip system (for a given temperature), can be determined by Schmid's law.

Schmid's law: When an axial force F is applied to a crystal with a cross section area A, *the resolved shear stress* τ *tending to produce slip on a plane* defined by angles θ and α is given by $\tau = (F/A)\cos\theta\cos\alpha$, where angles θ and α are shown in Fig.(2.6).

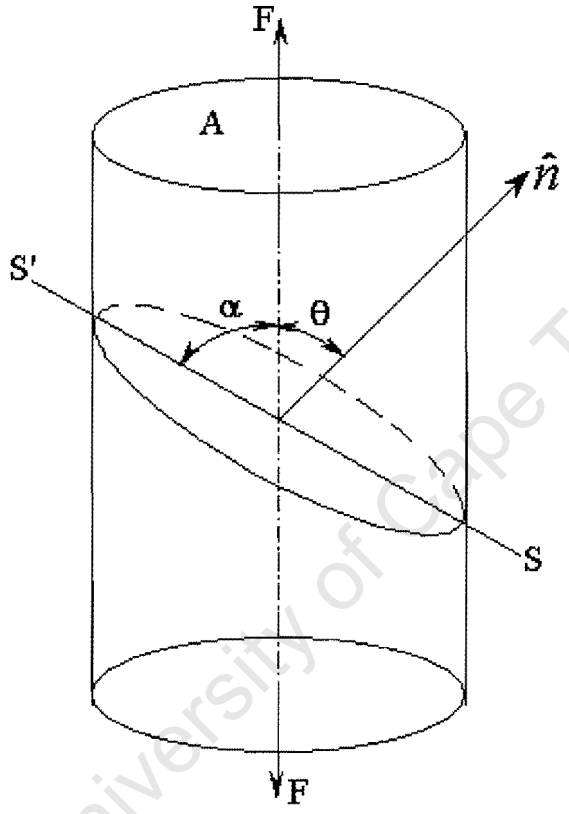

Figure 2.6 An axial force F applied to a crystal of cross section area A

According to Schmid's law, slip occurs when the resolved shear stress τ attains some critical value τ_c called the critical resolved shear stress. It was found experimentally [79], [97] that distinct slip systems in a single crystal require different stresses for their activation.

2.3 DISLOCATIONS

The mechanism of deformation presented in Section 2.2 shows that large deformations of metals are possible due to slipping on slip planes. When glide occurs in a real crystal, all atoms above the slip plane don't move simultaneously over those below. At any given time some of the atoms have moved into their new positions where others have not yet done so. The displacement of the upper block of crystal relative to the lower one varies from one region of the slip plane to another.

Dislocation lines separate regions where slip has occurred and regions where slip has not occurred. Hence in order to study the rate dependent material model in Chapter 3, we investigate some properties of dislocations.

In 1934 Taylor, Orwan and Polanyi first and independently proposed the existence of line defects or dislocations, which marked boundaries between slipped and unslipped regions of crystallographic plane. Slip, propagated by an advance of gliding dislocations into unslipped areas, involves an appropriate amount of bond breaking and reforming of broken bonds behind an advancing dislocation.

Definition 2.3: The dislocation density ρ is defined as the total length of dislocation lines in a unit volume of material.

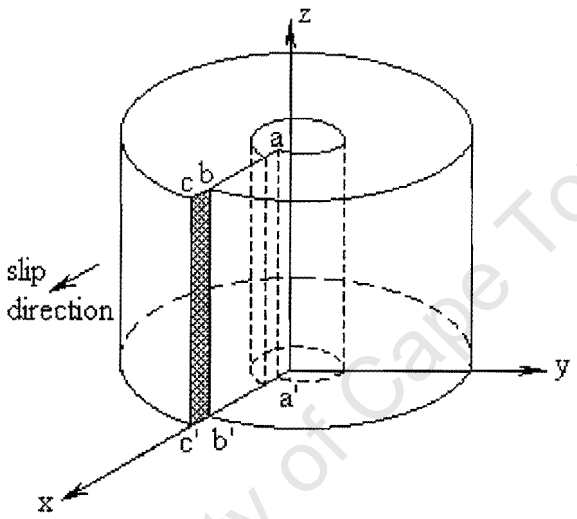

Figure 2.7(a) Edge dislocation in an elastic block

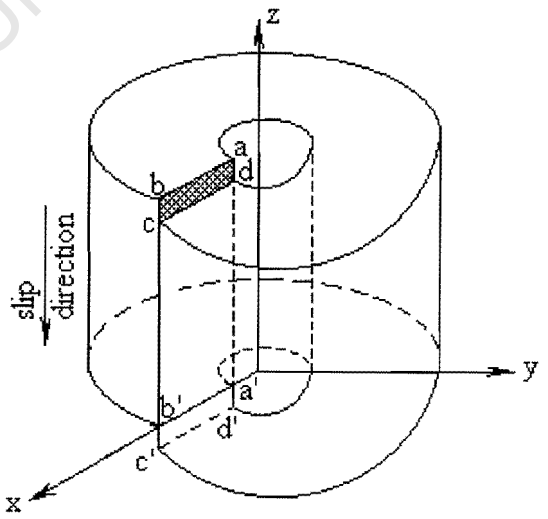

Figure 2.7(b) Screw dislocation in an elastic block

From the geometrical point of view, a dislocation is considered to be a line defect of a crystal lattice. These lines may either end up on crystal faces or they form closed loops inside of a crystal. In the case of straight dislocation lines whose ends emerge on crystal faces, one can distinguish between edge and screw dislocations Fig.(2.7). The direction of slip, indicated in this figure, corresponds with a so-called Burgers vector **b**. It is obvious that a line of an edge dislocation is orthogonal to this vector and in the case of a screw dislocation its line is parallel to the Burgers vector.

In general a dislocation should not be only parallel or orthogonal to the Burgers vector, but it may be oriented in any direction. A dislocation may even take a curve-like shape or be a closed loop, the Burgers vectors being constant along the dislocation line [97].

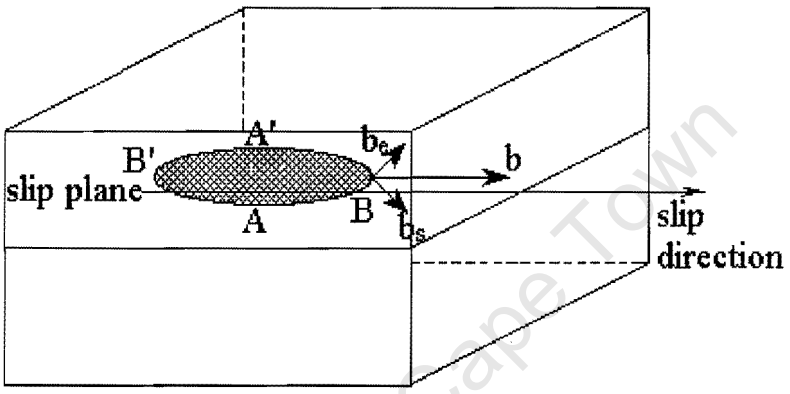

Figure 2.8 A dislocation loop

In the case of a closed loop dislocation, the region of deformation ABA'B' shown in Fig.(2.8) lies entirely within a crystal. The loop comprises a mixture of edge and screw dislocations to various degrees. At points A and A' it is a pure screw dislocation and at B and B' it is a pure edge dislocation. Fig.(2.9) shows the screw part $\mathbf{b}_s$ and the edge part $\mathbf{b}_e$ of Burgers vector **b** at an arbitrary place of the loop.

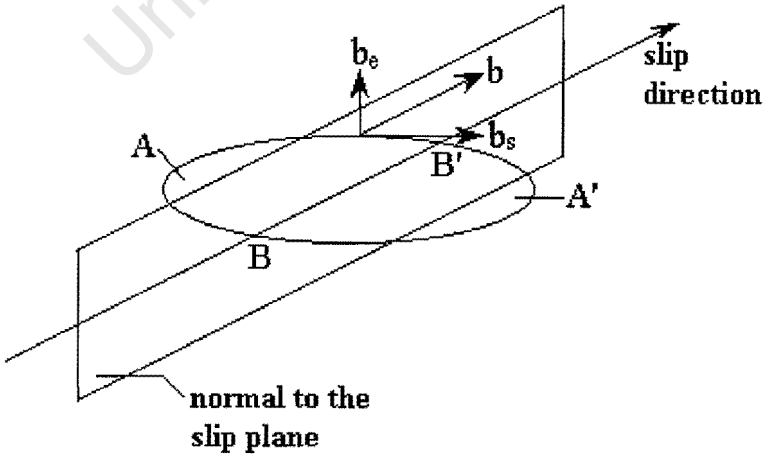

Figure 2.9 The screw part $\mathbf{b}_s$ and the edge part $\mathbf{b}_e$ of Burgers vector **b** at arbitrary place of a dislocation loop

Within the crystal lattice, plastic deformation occurs through movement of dislocation [34]. There are two distinct types of deformation mechanisms: a dislocation can glide on slip planes, or it can both glide and climb out of a slip plane, where only an edge dislocation can climb. The gliding on slip systems may appear due to dislocation motions as well as to their multiplication. Crystals normally contain aggregate number of dislocations even before their plastic deformation. The approximate length of the dislocation line in 1 cm^3 is 10^{-6} cm, although a wide variation is possible for various materials. A motion of dislocations on a slip system faces various obstacles, e.g. increase of a resistance force, which may stop the entire motion. At lower temperatures, where the stresses tend to be higher, dislocations move by glide. Under these conditions there are some factors that contribute to the magnitude of the yield stress.

2.4 MECHANISMS OF PLASTIC DEFORMATION

Elastic deformation, on the microscopic scale, is produced by small recoverable displacements of atoms, forming a crystal lattice, from their equilibrium positions. Plastic deformations are caused mainly by permanent relative slip of neighboring planes of atoms.

The following notions are necessary to describe infinitesimal deformations in the frame of the classical theory of plasticity:

1. yield condition that specifies the stress state for which plastic flow first begins,
2. stress-strain incremental constitutive equation that determines a plastic deformation,
3. hardening rule that describes the evolution of yield surface due to plastic deformation.

In large plastic deformation, the above aspects of plasticity play an equally important role in addition to other factors like the plastic anistropy and texture evolution which are related to plastic rotations. Texture evolution is related to the presence of vertices in the yield surface. The vertex structure of the yield surface, which is implied by the discrete nature of crystallographic slip, seems to be the key feature of plastic material response for the localization of plastic deformations (at least under low strain rates [52]).

The distribution of dislocations induced by large plastic deformations is an important factor in the change of stress-strain relations. It is known that such redistribution yields hardening both on the microlevel (diminishing of dislocation mobility) and on the macroscopic level. The studies on yield surfaces indicate the existence of:

1. isotropic hardening, where the elastic range of stresses expands uniformly in the stress space, the yield surface maintaining its shape, center and orientation,
2. kinematic hardening, where the origin of coordinates shifts in the stress space.

When crystalline materials are deformed at a constant rate of strain, the initial elastic behavior gives way to plastic yielding. There are several different processes involved in crystalline plasticity. An important requirement in a study of deformations

is therefore to identify the precise process occurring under selected conditions. In order to achieve this goal the usual method is to:

- examine and tabulate characteristics of various deformation processes,
- develop constitutive relations that describe the rate of flow in terms of internal parameters,
- construct a pictorial representation of constitutive relations in the form of deformation mechanism maps to deduce the precise set of conditions where each individual mechanism dominates.

The plastic deformation mechanism has two parts:

- lattice mechanism occurring within the crystalline lattice that is not associated with the presence of grain boundaries,
- boundary mechanism where deformations are associated with boundaries.

Taylor and Elam presented the shear stress-extension curve approximating experimental results in 1925. The first presentation of experimental results within the coordinates: shear stress versus strain was given in the paper by Taylor [87]. The parabolic approximation $\tau=\kappa\varepsilon^{1/2}$ has been proposed later by Taylor in [87].

Various extensions of the classical theories of plasticity to model rate-dependent behavior have been proposed, [6], [37], [60]. The rate-dependent model discussed in Chapter 3, differs from the classical rate independent "J_2 flow theory" by the lack of a yield condition, and loading/unloading criterion. Instead, plastic flow is assumed to occur at all non-zero values of stress, although at low stresses the rate of plastic flow may be immeasurably small. Further, the equivalent plastic strain rate and the material strain hardening are prescribed by an appropriate constitutive function in the rate dependent model, whereas it is determined by the consistency condition in the rate independent model. In the extremal surface model, on the other hand, the J_2 flow theory is assumed for the case when the sole mechanism of crystallographic multiple slip is responsible for plastic deformation. The contribution of active micro-shear bands, with their definite geometric pattern, to rate of plastic deformations is idealized by means of an additional double shearing system, normal to the flow plane.

The rate dependent formulation, discussed in Chapter 3, allows the calculations to be extended over much boarder range of material strain hardening properties and crystal geometry. This makes it possible to explore a correspondingly wider range of physical phenomena, as well as the important effects of material rate sensitivity on crystal plasticity and show the importance of shear localization in the large plastic deformatin of metals.

According to Deve and Asaro [29], in heavily deformed metals, shear localization progressively replaces the current deformation mode. This change in deformation mode contributes to the development of strain induced anistropy and modifies material properties. Therefore, formulation of a model of large plastic deformation appropriate to micro-shear bands is important for constitutive description of inelastic behavior of metals.

The idea of extremal surface is related to the concept of eigenmodes, which has been introduced in [40]. As it is emphasized in [40], the extremal surface is not a single yield surface but is rather an assemblage of yield points for physically distinct states of volume elements, none of which can be reached from any other via purely elastic paths in the stress space. Accordingly, the stress space can be split into the following three regions:

- elastic region enclosed by the elastic limit,
- intermediate region where only very small strains appear and which lies outside the elastic limit but is enclosed by the extremal surface,
- plastic region which lies outside the extremal surface and where larger strains appear (larger compared to those appearing in the intermediate region).

2.5 DEFORMATION TEXTURES

The aim of the texture analysis is to relate crystal orientations to some reference coordinate analysis. Coordinates in metals are usually specified by a production process, e.g. rolling.

The texture is developed during solidification from a melting point, and can be modified later either by deformation at higher or lower temperature or by recrystalization as well as solid phase transformations. The nature of texture is determined by mechanical and thermal history of a specimen. Plastic deformation is an important texture modifying process, usually by crystallographic slip or mechanical twinning.

The development of deformation textures is of great importance not only for a quantitative description of forming process, but also for anisotropy of properties of a product. Crystal orientations can be specified by listing a considerable number of most prominent orientations that are arbitrarily chosen to some. Much more accurate description is given by pole figures [97], which define a non-random crystal orientation distribution. A lattice orientation of grains is usually distributed about the particular orientation or a set of orientations. This type of preferred orientation of grains is called a texture.

Preferred crystal orientations (texture) depend on:

- particular deformation process (rolling, drawing, ... etc.),
- crystal structure of metal,
- temperature.

The following observations are characteristic for all polycrystalline materials:

- A crystal lattice may be permanently re-oriented but not deformed.
- An anisotropy of physical properties very often depends on the orientation distribution or texture of the crystallites in a material.
- The presence of elongated or flatted grains does not always imply a certain texture or even the presence of any texture at all.
- Study of a metallurgical texture, leads to explain its mechanical and thermal history.

- In certain cases, it is possible to minimize texture formation or to develop a desired texture by a controlled schedule of working and annealing.
- The plastic strain near a specimen surface may differ from that in the interior and may produce textures that vary with depth below a surface.
- The symmetry of the preferred orientation tends to match the symmetry of the principal strains, but perturbing properties may be involved that destroy the equality of those two symmetries.
- An orientation of a single crystal during rolling, wire drawing, compression or tensile elongation does not necessarily proceed along a path identical with that for a similarly oriented grain of a polycrystalline matrix.
- Anisotropy of mechanical properties may be influenced as much by elongation or flattened inclusions, voids, or grain boundaries as by preferred orientations of grains.
- Intermediate deformations of many kinds may produce a given change of shape, which may have an effect on the final texture, so that textures can not be uniquely predicted from only the change of shape.
- Pole figures or inverse pole figures are used to describe complex textures, and some preferred orientations are so simple that they can be adequately specified by one or more 'ideal textures'.

The textures of wires are frequently called fiber textures because they resemble the arrangement of oriented molecules and crystallites in fibrous materials, bcc metals have invariably a simple [110] fiber texture after cold drawing.

Textures in rolled (or extruded) sheet can be described in an approximate way by choosing one or two "ideal orientations" involving the plane (*hkl*) that lies parallel to the plane of the sheet and the direction [*uvw*] that lies in the rolling direction. Although the orientations found in greatest frequency can be specified in this way, i.e. by writing (*hkl*)[*uvw*], the details of the scatter about these ideal orientations can be specified by listing considerable number of less prominent orientations that are to some extent arbitrarily chosen.

Much more accurate description is given by the pole figures, which give the density distribution of a few sets of poles [*uvw*] on a map. The development of computer programs for plotting those figures has led to the expansion of this method as a standard way of reporting the experimental data.

In the case of cold rolling, (bcc) lattice produces the texture in which [110] directions of the grains lie along the direction of rolling and (001) planes lie in the plane of the rolled sheet. A fcc metal with a low enough stacking fault energy, when rolled at a low enough temperature, develops a texture with {110}<112> components.

2.6 SHEAR BANDS

Plastic deformation of metal crystals has long been known to occur by the development of discrete shear slip steps visible on the surface of the polished specimen with a light microscope or even by the naked eye as one or more sets of

parallel fine lines called slip lines. The application of higher magnification by means of the electron microscope shows that what appears as a line, or at best a narrow slip band in the light microscope, can be resolved by the electron microscope as discrete slip lamellae. These lamellae result from microscopic shear movements along well-defined crystallographic planes that are referred to as slip or glide planes. According to Neuhauser [68], the slip line corresponds to each slip step in the slip band, which is supposed to be produced by the movement of closely correlated dislocations in a moving dislocation group. Several slip lines are thus clustered to form a slip band.

A number of studies have shown that for a variety of metals and alloys the initially quasi-homogeneous plastic deformation is often replaced at a large strain by inhomogeneous deformation involving some form of shear banding [97]. Shear bands are the important feature of a deformed structure and appear to account for a major part of deformation at large plastic strains.

A lot of studies have been done to analyze the structure of shear bands [5], [14], [15], [17], [36], [72], [73], [74], but the physical nature and the structure of shear bands has not yet been completely explained, especially, the initiation and propagation mechanisms of micro-shear bands across grain boundaries.

A shear band seems to be an entirely natural outcome of large-strain deformation. Earliest tensile experiments on metallic specimens have already shown that initially homogeneous plastic deformation gives rise to flow localization into shear bands whose orientation is determined by compatibility conditions between them and the crystal matrix.

With regard to their dimensions, shear bands seem to appear at two different scales:

Microscopic shear bands

This type of shear bands extend through one or a few grains producing large shear strains, and form clusters or packets with width of approximately 0.1 μm. It appears on size-scale that encompasses groups of discrete dislocations or twins. On the larger size-scale that encompasses several microns to typical grain dimensions, plastic flow usually becomes localized. Micro shear bands are an example of such localization [5], [72].

Sample scale macroscopic shear bands

Shear bands of this type extend through the entire sample.

The concept of shear banding is related to plastic deformations produced by mechanisms of crystallographic slip and/or twinning together with micro-shear. There have been a lot of studies on shear banding, but the physical nature of the initiation and propagation of micro-shear bands is not completely described. Korbel [47] described the micro-shear bands as a kind of self-induced deformation mode. Anand and Spitzig [5] stated that they set in after reaching a certain critical state of loading or deformation represented by the critical value of flow stress or equivalent strain.

Localized deformation is the tendency of real materials due to variations in local flow stresses. In this sense, they appear as the result of local instability of the development of plastic deformations. This is in contrast to some other instability like the Luders bands, which are connected with the onset of the new physical mechanism, e.g. rapid multiplication of dislocations. Shear bands result from a bifurcation of a plastic deformation field. These instabilities are inhibited by local hardening of the slip systems and may be promoted by textures, which are connected with inter-granular softening.

Experiments in the field of shear localization have been rather empirical in nature primarily because of the lack of a consistent analytical framework, which could guide an experimentalist. The present theories of plasticity can only predict the initiation but not evolution of shear localization from a homogeneous state. However, it has been found out, that in general shear bands are not oriented along the characteristic curves of the hyperbolic system of equations derived from equilibrium equations and the yield conditions. It means that they do not follow stress characteristics, i.e. they are not oriented along the slip lines of the classical slip line theory. Instead, they are oriented parallel to the characteristic curves associated with the loss of elipticity of the system of partial differential equations obtained by substituting the rate-type constitutive equations into the equilibrium equations. These are velocity characteristics, which usually do not coincide with stress characteristics.

During the past 25 years, there has been intensive work by Asaro and co-authors [8], [9], [10], [29], [36], [74], [75] to understand the micro- and macro-mechanics of shear band forming during uniaxial and plane strain tension in a single crystal.

Electron microscopy of the structure and crystallography of shear bands and the large-strain computational studies, conducted by using strain rate dependent constitutive theories, show that macroscopically localized shearing is indeed a natural outcome of crystalline slip. In particular, geometrical softening is caused by uniform lattice orientation. In summary, the formation of macroscopically localized shear bands appears to be a natural aspect of plasticity of single crystals of fcc and bcc metals. The bands can form while the materials are strain hardening. The bands are characterized by mis-orientation with respect to active slip systems and in the case of Al-Cu and copper crystals this mis-orientation has been shown to be associated with the "geometrical softening" of the active crystallographic slip systems.

Chang and Asaro [23] pointed out differences in phenomenology related to chemistry and microstructure. Hatherly and Malin [39] have reviewed many of the experimental literature on shear band formation in plane strain compression and plane strain rolling. They also categorized materials into three classes according to stacking fault energy:

Class I	$\gamma \leq 20\ \text{mJ/m}^2$ (low stacking fault energy, SFE)
Class II	$20\ \text{mJ/m}^2 \leq \gamma \leq 40\ \text{mJ/m}^2$
Class III	$\gamma \geq 40\ \text{mJ/m}^2$ (high stacking fault energy, SFE)

According to the study of Gil Sevillano [80] and Harren *et al.*[36] the amount of micro-shear bands and also the size and volume fraction of the micro-shear bands depends strongly on *the Stacking Fault Energy* (SFE) of the material.

In the case of low stacking fault energy, Hatherly and Malin [39] reported that shear bands in polycrystals form symmetric pairs at angle α to the rolling plane, where $18^\circ \leq \alpha \leq 45^\circ$. Bands form in microstructures characterized by previously formed

micro-twins. These bands occur for total logarithmic strain ε larger than 0.5, and develop in density and size until strains reach the level of $\varepsilon > 1.2 \div 1.5$, when the new set of more intensive macroscopic bands occur. These observations seem to be consistent with the study by Embury *et al.* [32] on single crystals of Al-Cu. Embury *et al.* [32] indicate that shear bands appear at compressive strains ε> 0.5 and they are inclined at 10° to the rolling direction. At larger strains in the range of $\varepsilon = 1.2 \div 1.6$, a newly formed generation of macroscopic bands are inclined at $33^\circ \leq \alpha \leq 37^\circ$ to the rolling direction. Embury *et al.* [32] concluded that the substructures formed during early strain increments could be re-arranged with respect to the ongoing deformation and they would become unstable and generate localized slip.

Hatherly and Malin [39] suggest that, in materials of class III in a given volume element, only one set of bands can be formed. Bands are proceeding by the development of micro-bands. Korbel *et al.* [48] have studied this process in crystals of Aluminum alloys. He reported that micro-bands that formed at small strains prior to shear bands, lie on the {111} slip planes, and go through the existing dislocation sub-structure.

For the (fcc) materials of the third case, Pecherski [72] reported that the *Stacking Fault Energy* (SFE) is greater than 40 mJ/m^2, whereas the volume fraction of micro-shear bands is low.

The formation of shear bands in single crystals of Al-Cu and copper subject to plane strain compression is the subject of the present thesis. The phenomenology of shear band formation in such materials is similar to that described for materials with the high *Stacking Fault Energy* (SFE) materials.

CHAPTER THREE

RATE DEPENDENT MATERIAL MODEL

3.1 INTRODUCTION

In this chapter a rate dependent material model for localized deformation in crystalline solids, developed by Peirce et al. [75] is considered following the pioneering work of Taylor [92]. A precise mathematical model of physical concepts are proposed by Hill [40], and Hill and Rice [41] who established a quantitative description of plastic deformation based on crystallographic shearing. Taylor's concept has been developed by Rice and Hill as a general finite deformation elastic-plastic framework for analyzing a deformation of rate independent single crystals. Peirce, Asaro, and Needleman [75] proposed the constitutive laws for rate dependent crystals. The kinematics of deformation of a single crystal is discussed together with constitutive equations for rate dependent crystals and hardening rule. The main equations are derived following Peirce, Asaro, and Needleman [75].

A numerical algorithm with internal variables is provided here for integration of rate dependent constitutive equations of the rate dependent model. The algorithm is implemented into a material user subroutine (UMAT) for the FE program ABAQUS [1], [2].

3.2 MATERIAL MODELING

The basic assumption of the rate dependent model proposed by Peirce *et al.* [75] is that a crystallographic slip is a sole cause of inelastic deformation and a material flows through a crystal lattice via dislocation motion. The lattice itself undergoes elastic deformations and rotations.

Standard notations are used for matrices and tensor operations. Summation over crystallographic slip systems is indicated explicitly while the summation convention is used for Latin indices. Inverses, transposes, and transposed inverses are denoted with a superscripts $^{-1}$, ^{T}, $^{-T}$ respectively. Superposed dots indicate differentiation with respect to time t. Dots and double dots operations are defined as follows:

$$r_i t_i = \sum_{i=1}^{n} r_i t_i$$

$$\mathbf{C} : \mathbf{P} = C_{ijkl} P_{kl},$$

$$\mathbf{P} : \mathbf{D} = P_{ij} D_{ji} = \sum_{i,j=1}^{n} P_{ij} D_{ji},$$

$$\mathbf{P} \circ \mathbf{m} = P_{ij} m_j = \sum_{j=1}^{n} P_{ij} m_j,$$

$$\sigma \cdot \mathbf{P} = \sigma_{ij} P_{jk} = \sum_{j=1}^{n} \sigma_{ij} P_{jk},$$

$$\frac{\partial \tau_{ij}}{\partial x_j} = \sum_{j=1}^{n} \frac{\partial \tau_{ij}}{\partial x_j},$$

where n is the number of slip systems.

Kinematics of elastoplastic materials is based on the assumption of the unique decomposition of the deformation gradient **F** into two parts: the elastic part **E**, and the plastic part **P**, that is written as

$$\mathbf{F} = \mathbf{EP}. \qquad (3.1)$$

This decomposition follows Lee's [54] concept. In reality the elastic distortion of a lattice and plastic flow occur simultaneously. It is obvious that any elastically and plastically deformed current configuration of a crystal can be reached by an imagined sequence of events. A convenient, physically based, way of separating the elastic and plastic deformations is provided.

Plastic component **P** consists only of crystallographic slip on specific slip systems which represents the local plastic deformation gradient. Local elastic deformation gradient **E** accounts for the elastic stretching and rotation in addition to any rigid body rotations. The deformation gradient remaining after elastic unloading and upon returning the lattice to its orientation in the reference state is $\mathbf{P} = \mathbf{E}^{-1} \cdot \mathbf{F}$. In a real process removal of loads alone will not return a lattice to its original state. Thus what remains as a residual after slip is more than just P. The lattice may be permanently reoriented but undeformed.

Kinematics of a single crystal deformation is described in the following manner:

A virgin crystal with an undeformed stress free lattice is imagined to be the reference configuration where each material particle is described by its reference position **X**.

The slip system α of a crystal is defined by the orthogonal pair of unit vectors ($\mathbf{m}^\alpha$, $\mathbf{n}^\alpha$). Vectors $\mathbf{m}^\alpha$ represent α–th slip direction in the reference configuration, and $\mathbf{n}^\alpha$ represents the normal to α–th slip plane in the reference configuration (see Appendix A).

An elastically and plastically deformed crystal in the current configuration is described by the current position **x** of a material particle. Displacement **u** that each material particle undergoes as it moves from the reference state to the current state is **u** = **x** - **X**. Deformation gradient **F** in the current configuration is given by

$$\mathbf{F} = \frac{\partial \mathbf{x}}{\partial \mathbf{X}} = \mathbf{I} + \frac{\partial \mathbf{u}}{\partial \mathbf{X}}.$$

If $\frac{\partial \mathbf{u}}{\partial \mathbf{X}} = 0$ then $\mathbf{F} = \mathbf{I}$, that refers to the case without motion, where $\mathbf{I}$ is the second order identity tensor. In order to reach the current configuration from the reference, one imagines first that the material flows along the various slip systems of a crystal to reach an intermediate configuration, that is described by the plastic deformation gradient $\mathbf{P}$. Eulerian velocity gradient $\mathbf{L}^P$ in the intermediate configuration is written as

$$\mathbf{L}^P = \dot{\mathbf{E}} \cdot \mathbf{P}^{-1} = \sum_\alpha \dot{\gamma}^\alpha \mathbf{n}^\alpha \mathbf{m}^\alpha, \qquad (3.2)$$

where $\gamma^{\bullet\alpha}$ is the rate of shearing on the specific slip system. According to Hill and Rice [41], the plastic deformation gradient $\mathbf{P}$ is obtained by the path dependent integration of Eq. (3.2). From this plastically sheared state, the current configuration is reached by elastic distortion and rigid rotation of a lattice along with its embedded material. This step of deformation is determined by elastic deformation gradient $\mathbf{E}$.

The plastic deformation gradient on the slip system is given by the flow rule

$$\dot{\mathbf{P}} = \mathbf{L}^p \cdot \mathbf{P},$$

where $\mathbf{L}^P$ is the plastic part of the velocity gradient defined by Eq. (3.2).

Following [75] the plastic part of the Eulerian velocity gradient can also be written as

$$\mathbf{L}^P = \mathbf{E} \cdot \dot{\mathbf{P}} \cdot \mathbf{P}^{-1} \cdot \mathbf{E}^{-1} = \sum \dot{\gamma}^\alpha \overset{*}{\mathbf{n}}{}^\alpha \overset{*}{\mathbf{m}}{}^\alpha;$$

where

$$\overset{*}{\mathbf{n}} = \mathbf{E} \circ \mathbf{n}; \quad \overset{*}{\mathbf{m}} = \mathbf{m} \circ \mathbf{E}^{-1}, \qquad (3.3)$$

with rate of shearing $\dot{\gamma}^\alpha$ on specific slip system α, and orthogonal vectors $\overset{*}{\mathbf{n}}{}^\alpha, \overset{*}{\mathbf{m}}{}^\alpha$ representing stretching and rotation of $\mathbf{n}$ and $\mathbf{m}$.

Eulerian velocity gradient $\mathbf{L}$ can be written in terms of total rates of stretching $\mathbf{D}$ and total rate of spin Ω

$$\mathbf{L} = \mathbf{L}^P + \mathbf{L}^e = \mathbf{D} + \Omega,$$

$$\mathbf{L} = [\mathbf{D}^P + \Omega^P] + [\mathbf{D}^e + \Omega^e]$$

where $\mathbf{D}^P$ and Ω^P are total rates of plastic stretching and spin, respectively. They contain contributions due to the plastic shearing, while $\mathbf{D}^e$ and Ω^e are the rates of elastic stretching and spin, respectively, which represent deformations of a lattice and body rotations. Using Eq. (3.3) the plastic deformation rate can be expressed in the form

$$\mathbf{L}^P = \sum_\alpha \dot{\gamma}^\alpha [\mathbf{P}^\alpha + \mathbf{W}^\alpha]$$

where

$$\mathbf{P}^\alpha = \frac{1}{2}(\overset{*}{\mathbf{n}}{}^\alpha \overset{*}{\mathbf{m}}{}^\alpha + \overset{*}{\mathbf{m}}{}^\alpha \overset{*}{\mathbf{n}}{}^\alpha); \quad \mathbf{W}^\alpha = \frac{1}{2}(\overset{*}{\mathbf{n}}{}^\alpha \overset{*}{\mathbf{m}}{}^\alpha - \overset{*}{\mathbf{m}}{}^\alpha \overset{*}{\mathbf{n}}{}^\alpha).$$

The symmetric part of stretching is

$$\mathbf{D}^p = \sum_\alpha \mathbf{P}^\alpha \dot{\gamma}^\alpha \quad ,$$

and the plastic rotation, which is the main cause of textures, is given by

$$\Omega^p = \sum_\alpha \mathbf{W}^\alpha \dot{\gamma}^\alpha \cdot$$

The elastic part of velocity gradient is

$$\mathbf{L}^e = \dot{\mathbf{E}} \cdot \mathbf{E}^{-1} = \mathbf{D}^e + \Omega^e \ . \tag{3.4}$$

Let $\tau^\bullet$ be the material rate of the Kirchhoff stress; then the Jaumann rate of the Kirchhoff stress τ is given by

$$\overset{\nabla^*}{\tau} = \tau^\bullet - \Omega^e \tau + \tau \Omega^e \cdot \tag{3.5a}$$

The Jaumann stress rate in the frame of reference rotating with the material is given by

$$\overset{\nabla}{\tau} = \tau^\bullet - \Omega \tau + \tau \Omega \cdot \tag{3.5b}$$

Subtracting Eq. (3.5a) from Eq. (3.5b), the Jaumann rate of the Kirchhoff stress is

$$\overset{\nabla^*}{\tau} = \overset{\nabla}{\tau} + (\Omega - \Omega^e)\tau - \tau(\Omega - \Omega^e) = \overset{\nabla}{\tau} + \Omega^p \tau - \tau \Omega^p = \overset{\nabla}{\tau} + \sum_\alpha \mathbf{W}^\alpha \dot{\gamma}^\alpha \cdot \tau - \tau \sum_\alpha \mathbf{W}^\alpha \dot{\gamma}^\alpha \ .$$

The Jaumann rate of the Kirchhoff stress $\overset{\nabla^*}{\tau}$ is

$$\overset{\nabla^*}{\tau} = \overset{\nabla}{\tau} + \sum_\alpha \beta^\alpha \dot{\gamma}^\alpha \ ,$$

where β^α has the form $\beta^\alpha = \mathbf{W}^\alpha \cdot \tau - \tau \cdot \mathbf{W}^\alpha$.

Assuming that crystal's elasticity is unaffected by slip, the elastic law takes the form

$$\overset{\nabla^*}{\tau} = \mathbf{C} : \mathbf{D}^e \ ,$$

where $\overset{\nabla^*}{\tau}$ is the Jaumann rate of the Kirchoff stress for a crystal lattice, and $\mathbf{C}$ is the elastic moduli tensor.

Thus the material Jaumann rate of the Kirchhoff stress is

$$\overset{\nabla}{\tau} = \overset{\nabla^*}{\tau} - \sum_\alpha \beta^\alpha \dot{\gamma}^\alpha = \mathbf{C} : \mathbf{D}^e - \sum_\alpha \beta^\alpha \dot{\gamma}^\alpha \ ,$$

The above equation can be written as

$$\overset{\nabla}{\tau} = \mathbf{C} : \mathbf{D} + \sum_\alpha \mathbf{R}^\alpha \dot{\gamma}^\alpha \tag{3.6}$$

where

$$\mathbf{R}^\alpha = \mathbf{C} : \mathbf{P}^\alpha + \beta^\alpha$$

Plastic shearing rate $\dot{\gamma}^\alpha$ for the rate dependent formulation is a function dependent on a current resolved shear stress on slip system α, current slip system strength or hardness g^α, and other parameters determined for a current internal structure. This relationship can be expressed as

$$\dot{\gamma}^{\alpha} = F(\tau^{\alpha}, g^{\alpha}) = \dot{a}^{\alpha} \left[\frac{\tau^{\alpha}}{g^{\alpha}}\right] \left[\left|\frac{\tau^{\alpha}}{g^{\alpha}}\right|\right]^{(1/m)-1}, \qquad (3.7)$$

where τ^{α} represents the current value of the resolved shear stress, and $\dot{a}$ is the shear rate in the reference configuration. Exponent $\frac{1}{m}$ characterizes the material rate sensitivity, which is the same for all slip systems. When m approaches zero, the rate independent response is achieved. In this limit g^{α} may be interpreted as strength τ^{α} of a current slip system. Generally g^{α} for $m \neq 0$ is the strength of a current slip system when the slip system shears at its reference rate $\dot{a}$.

For the rate dependent model, the activity of slip systems is determined by a current stress state and then a slip rate is uniquely determined. This eliminates the ambiguity in choosing which slip system is active.

The slip resistance function g^{α} in Eq. (3.7) depends on the sum of slip magnitudes

$$g^{\alpha} = g^{\alpha}(\gamma), \qquad \gamma = \sum_{\alpha=1}^{n} \int_{0}^{t} \left|\dot{\gamma}^{\alpha}\right| dt.$$

In expression Eq. (3.7), when shearing rate on system α is equal to a compressive strain rate $\dot{\gamma}^{\alpha} = \dot{a}$, the relation between resolved shear stress and strain hardening is given by

$$\text{sign}(\tau^{\alpha}) \left|\frac{\tau^{\alpha}}{g^{\alpha}}\right|^{\frac{1}{m}} = 1.$$

The evolution equation for slip resistance function g^{α} is taken as

$$\dot{g}^{\alpha} = \sum_{\beta} h_{\alpha\beta} \left|\dot{\gamma}^{\beta}\right|, \qquad (3.8a)$$

$$h_{\alpha\beta} = q\,h + (1-q)\,h\,\delta_{\alpha\beta}, \qquad (3.8b)$$

with strain rate hardening $h_{\alpha\beta}$ on system α due to shearing on system β. It depends on the history of deformation and temperature. Parameter q is used to set a level of latent hardening as compared to self-hardening of a slip system. The condition q=1 leads to Taylor's hardening $h_{\alpha\beta} = h$, where h is a function of an accumulated slip. When hardening of a slip system is taken as Taylor's isotropic hardening such that all slip systems of a given crystallite have the same strength, the hardening moduli in Eq.(3.8b) are

$$h_{\alpha\beta}(\gamma) = \frac{\partial\, g(\gamma)}{\partial\, \gamma}\, \mathbf{A},$$

where in the case of double slip systems $\mathbf{A}$ is a 2×2 unit matrix.

Peirce *et al.* [75], [76] in their rate dependent analysis specified $h(\gamma)$ by

$$h(\gamma) = h_{\circ} \sec h^{2}\left(\frac{h_{\circ}\gamma}{\tau_{s} - \tau_{\circ}}\right),$$

where $h_{\circ}$ denotes the initial hardening rate, and τ_{s} is the saturation strength.

According to Schmid's (1928) law (see above): "*A single crystal yields on a particular slip system if the shear stress resolved on the slip plane and slip direction reaches a critical value, called the yield stress on a slip system*". One can determine whether a particular slip system is active or not.

For uniaxial test and tensile axis x_1 the resolved shear stress on slip system α is given by

$$\tau^{\alpha} = \overset{*\alpha}{\mathbf{n}}_1 \overset{*\alpha}{\mathbf{m}}_1 \sigma_{11},$$

where σ_{11} is a tensile stress.

This expression can be generalized for more complex loading conditions. The resolved general shear stress on slip system α is given in terms of Cauchy stress σ by

$$\tau^{\alpha} = \sum_{i=1}^{3}\sum_{j=1}^{3} \overset{*\alpha}{\mathbf{n}}_j \overset{*\alpha}{\mathbf{m}}_j \sigma_{ij}.$$

Orientations evolved with deformation are represented by slip directions $\overset{*\alpha}{\mathbf{m}}$ and normal to the slip planes $\overset{*\alpha}{\mathbf{n}}$.

The absolute value of product $\mathbf{n}_1^{\alpha}\mathbf{m}_1^{\alpha}$ is called the Schmid factor and is expressed by

$$m = \text{abs}\,(\mathbf{n}_1^{\alpha}\mathbf{m}_1^{\alpha}).$$

In the rate dependent formulation there is no explicit yielding, and plastic shearing occurs when a shear stress resolved on a slip system is non-zero. However, for small values of rate sensitivity exponent m, the rate of plastic shearing $\overset{*\alpha}{\dot{\gamma}}$ on system α is very small when the resolved shear stress is less than the yield limit τ_o, so all slip systems in the present formulation are potentially active. Slip systems with positive slip will be considered and thus $\overset{*\alpha}{\dot{\gamma}}$ would have the sign of a resolved shear stress corresponding to slip system α (see Eq. (3.7)). There is no reason to consider conjugate negative slip systems.

3.3 EVALUATION OF RESOLVED SHEAR STRESS

In general, differential evolution equations for stress and deformation resistance can be integrated numerically. Constitutive equations of this type have long been known to be numerically very stiff [76], [83]. The size of time increment is generally restricted by numerical stability requirement [25]. The Euler scheme can be implemented for elastic-viscoplastic problems [7], [24], [93], [109]. This advantage is generally offset by the need for an excessive number of increments when the large deformation analysis is performed.

To overcome the stability restrictions for time increments inherent in the Euler forward scheme, a number of authors [6], [62], [76] have described semi-implicit time-integration scheme, where relevant constitutive functions are approximated by using two-term Taylor's series expansion in the neighborhood of the initial state. These "forward gradient" schemes allow much larger time increments without encountering stability problems or requiring constitutive level iterations. Their shortcoming is that their accuracy can be severely deteriorated by taking large time increments during

periods of rapidly changing conditions. Consequently, it is still necessary to control the size of a time increment very carefully in order to obtain an accurate solution.

The integration of the stress rate equation

$$\overset{\nabla}{\tau} = \mathbf{C}:\mathbf{D} - \sum_{\alpha=1}^{N} \dot{\gamma}^{\alpha} \mathbf{R}^{\alpha}, \tag{3.9}$$

requires small time steps for stable numerical integration, when the slip rate is determined as an explicit function of the current state. Here, the tangent moduli method by Peirce *et al.* [75] is employed to increase the size of the stable time step. In this method a change of shear rate $\dot{\gamma}^{\alpha}$ during the current time increment is estimated. This leads to an expression for a tangent stiffness with improved numerical stability. This numerical procedure, called the forward gradient method [83], [101], [41], is explained in details by Peirce et al. [75] for various constitutive equations. It provides a forward gradient estimate of slip rate, which is based on the Taylor series expansion about a current slip rate.

Following Peirce *et al.* [75], the resulting slip rate is given by

$$\dot{\gamma}^{\alpha} = \dot{f}^{\alpha} + \mathbf{F}^{\alpha}:\mathbf{D}, \tag{3.10}$$

$$\dot{f}^{\alpha} = \sum_{\beta=1}^{N} \mathrm{M}_{\alpha\beta} \dot{\gamma}^{\alpha},$$

$$\mathbf{F}^{\alpha} = \sum_{\beta=1}^{N} \mathrm{M}_{\alpha\beta} \left(\frac{\theta \Delta t \dot{\gamma}^{\beta}}{\mathrm{m}\tau^{\beta}}\right) \mathbf{R}^{\beta},$$

where the parameter θ ranges from 0 to 1, $\mathrm{M}_{\alpha\beta}$ is the inverse of $\mathrm{N}_{\alpha\beta}$

$$\mathrm{N}_{\alpha\beta} = \delta_{\alpha\beta} + \left(\frac{\theta \Delta t \dot{\gamma}^{\alpha}}{m}\right) \times \left[\frac{\mathbf{R}^{\alpha}:\mathbf{P}^{\beta}}{\tau^{\alpha}} + \mathrm{sgn}(\tau^{\beta}) \frac{h_{\alpha\beta}}{g^{\alpha}}\right].$$

and $\mathrm{h}_{\alpha\beta}$ are functions of γ defined in Eq. (3.8b). Substituting Eq. (3.10) into Eq. (3.9) results in

$$\overset{\nabla}{\tau} = \mathbf{C}:\mathbf{D} - \sum_{\alpha=1}^{N} [\dot{f}^{\alpha} + \mathbf{F}^{\alpha}:\mathbf{D}]\mathbf{R}^{\alpha} = (\mathbf{C} - \sum_{\alpha=1}^{N} \mathbf{R}^{\alpha}\mathbf{F}^{\alpha}):\mathbf{D} - \sum_{\alpha}^{N} \mathbf{R}^{\alpha} \dot{f}^{\alpha}, \tag{3.11}$$

where $\mathbf{C} - \sum_{\alpha=1}^{N} \mathbf{R}^{\alpha}\mathbf{F}^{\alpha}$ and the right hand side vector represents the Jacobian and the right hand side contribution for the integration point.

The forward gradient method reduces the Jacobian, by permitting larger strain increments while producing moderate stress increments. This increases the numerical stability of the algorithm.

The strain rate $\dot{\gamma}^{\alpha}$ is calculated from Eq. (3.10) and used to update the hardening g^{α} by applying Eq. (3.8)

$$g_{n+1}^{\alpha} = g_{n}^{\alpha} + \Delta t \sum_{\beta} h_{\alpha\beta} \left|\dot{\gamma}^{\beta}\right|, \tag{3.12}$$

Values of g^{α}, α=1,...,12 for $\gamma = 0$ must be specified and taken to satisfy the relation $g^{\alpha}(0) = \tau_{\circ}$, where $\tau_{\circ}$ is the initial yield limit.

Hardening of a slip system and a stress state for each grain is incremented by using the rotation algorithm [1], [44]. This can be done after evaluation of a slip increment and the accumulated slip rate. The stress corrected by adding the rotation to the to RHS of Eq. (3.11)

$$\tau_{n+1} = \mathbf{Q}\cdot\tau_n\cdot\mathbf{Q}^T + \Delta t[\mathbf{C} - \sum_{\alpha=1}^{N}\mathbf{R}^\alpha\mathbf{F}^\alpha]:\mathbf{D} - \Delta t\sum_{\alpha=1}^{N}\mathbf{R}^\alpha\overset{\bullet}{\mathbf{f}}^\alpha, \qquad (3.13)$$

where $\mathbf{Q}$ is the material rotation increment .

Once slips and stresses are updated, the new deformation gradient $\mathbf{F}$ follows immediately from the displacement.

The plastic part $\mathbf{P}$ of the total deformation gradient $\mathbf{F}$ is updated by

$$\mathbf{P}_{n+1} = [1 + \Delta t\sum_{\alpha}\dot{\gamma}^\alpha Z^\alpha]\mathbf{P}_n, \qquad (3.14)$$

where $Z^\alpha = \mathbf{m}^\alpha \otimes \mathbf{n}^\alpha$.

The new $\mathbf{E}$ is calculated from $\mathbf{E} = \mathbf{F}\cdot\mathbf{P}^{-1}$. Knowing $\mathbf{E}$, $\mathbf{P}^\alpha, \beta^\alpha, \mathbf{R}^\alpha, \overset{*}{\mathbf{m}}^\alpha, \mathbf{W}^\alpha$ and $\overset{*}{\mathbf{n}}^\alpha$, the resolved shear stress τ^α is evaluated, and the new current state of the internal variables can be defined. A summary of the implementation of the rate dependent model into ABAQUS is given in Table 3.1.

Table 3.1 Algorithm of the user subroutine UMAT in ABAQUS for the rate dependent model.

1. ***Begin***
2. ***input initial values***: slip vectors ($\mathbf{m}_\alpha$, $\mathbf{n}_\alpha$), elastic constants, an initial crystal orientation placed in the array PROPS, initial values of **E.**

assume $\mathbf{R} = \mathbf{E}$ for t = 0 where $\mathbf{E} = \mathbf{F}\bullet\mathbf{P}^{-1}$

3. ***calculate slip rate increments*** $\Delta\gamma^\alpha = (\overset{\bullet}{\mathbf{f}}^\alpha + \mathbf{F}^\alpha:\mathbf{D})\Delta t$ for given array DSTRAIN with estimation of the strain increment,
4. ***evaluate accumulated slip*** $\gamma = \int_0^t|\dot{\gamma}^\alpha|dt$ and place it in array STATEV,
5. ***update*** $g^\alpha_{n+1} = g^\alpha_n + \sum_\beta h_{\alpha\beta}\left|\Delta\gamma^\beta\right|$, using an accumulated slip in the step 3 and place it in array STATEV
6. ***evaluate an increment of stress state***

   $\tau_{t+\Delta t} = \mathbf{Q}\cdot\tau_t\cdot\mathbf{Q}^T + \Delta t(\mathbf{C} - \sum_{\alpha=1}^{N}\mathbf{R}^\alpha\mathbf{F}^\alpha):\mathbf{D} - \Delta t\sum_{\alpha}^{N}\mathbf{R}^\alpha\dot{\mathbf{f}}^\alpha$ using Hughes-Winget rotation algorithm with the modulus $(\mathbf{C} - \sum_{\alpha=1}^{N}\mathbf{R}^\alpha\mathbf{F}^\alpha)$ placed in array DDSDDE, and updated stress placed in the array STATEV
7. ***calculate plastic*** part $\mathbf{P}_{n+1} = [1 + \Delta t\sum_\alpha\dot{\gamma}^\alpha Z^\alpha]\mathbf{P}_n$, $Z^\alpha = \mathbf{m}^\alpha\otimes\mathbf{n}^\alpha$ of total deformation gradient **F**
8. ***calculate elastic*** part $\mathbf{E} = \mathbf{F}\cdot\mathbf{P}^{-1}$ and place it in the array STATEV.
9. ***update*** $\beta^\alpha, \mathbf{R}^\alpha, \mathbf{W}^\alpha$ and $\mathbf{P}^\alpha$ knowing **E**
10. ***calculate the resolved shear stress*** $\tau^\alpha = \mathbf{P}^\alpha:\sigma$
11. ***end.***

3.4 METHOD OF SOLUTION TO THE FINITE ELEMENT EQUATION

The nonlinear finite element system of equations is solved in ABAQUS iteratively by the Newton-Raphson scheme. The system can be written in the form

$$[K][U]=[F] \tag{3.15}$$

where K is the stiffness matrix, and F is the right hand side vector contribution for the integration point (see Eq. 3.11).

The L.H.S can be defined as the linear function of $[U]$.

The Newton-Raphson method provides the approximation $[U]^{i+1}$ of the root $[U]^*$ of the equation

$$g[U] = 0, \tag{3.16}$$

computed from the approximation of $[U]^i$ using the equation

$$\frac{\partial g}{\partial U}\{[U]^{i+1} - [U]^i\} = -g[U]^i. \tag{3.17}$$

Replacing $[K][U]$ by $[F]$ and substituting $\frac{\partial g}{\partial U} = [K]$ in Eq. (3.17) shows that

$$[U]^{i+1} = [U]^i - [K]^{-1}[F]^i . \tag{3.18}$$

Rearranging of the last relation leads to the form

$$[K]\{[U]^{i+1} - [U]^i\} = [F]^i \tag{3.19}$$

from where the convergency of the method can be evaluated. The matrix $[U]^i$ converges to the solution $[U]^*$ when $[U]^{i+1} - [U]^i$ converges to zero, which happens when the right hand vector contribution for the integration point is zero: $[F]^i = 0$.

CHAPTER FOUR

THE EXTREMAL SURFACE PHENOMENOLOGICAL MODEL

4.1 INTRODUCTION

This chapter is concerned with studying shear localization and the contribution of micro-shear bands in a large plastic deformation process. Rate independent deformations in polycrystalline metallic materials are considered together with the concept of extremal surface accounting for effects of micro-shear bands and crystallographic slip over slip systems. An appropriate algorithm is implemented as a user material subroutine UMAT in FE program ABAQUS to evaluate large deformations, when crystallographic multiple slip or twinning are progressively replaced by shear localization.

Section 4.2 contains the basic notations and symbols used in this chapter.

Section 4.3 contains the main constitutive equations used in modelling of large plastic deformations accounting for micro-shear bands by means of double-shearing system, and an additional double shearing system. These notions are considered to approximate the effect of micro-shear bands.

Section 4.4 contains a Finite Element formulation of the model with extremal surface. An algorithm for evaluation of equivalent plastic strains and a procedure for computing of the tangent moduli are described there. Constitutive equations are implemented via a user material subroutine UMAT in the FE program ABAQUS.

4.2 Basic Notations

The following notations are employed: **s** represents the deviatoric stress, and **e** is the deviatoric strain. These tensors are defined by

$$\mathbf{s} = \sigma - \frac{1}{3}(tr\sigma)\mathbf{1}, \tag{4.1}$$

$$\mathbf{e} = \varepsilon - \frac{1}{3}(tr\varepsilon)\mathbf{1}, \tag{4.2}$$

where **1** is the second order unit tensor and $tr\sigma$, $tr\varepsilon$ are traces of stress and strain tensors.

The natural inner product of the linear vector spaces of deviatoric stress and deviatoric strain is defined as

$$\mathbf{s} : \bar{\mathbf{s}} = tr[\mathbf{s} \cdot \bar{\mathbf{s}}^t] \equiv s_{ij}\,\bar{s}_{ij}, \tag{4.3}$$

$$\mathbf{e} : \bar{\mathbf{e}} = tr[\mathbf{e} \cdot \bar{\mathbf{e}}^t] \equiv e_{ij}\bar{e}_{ij}, \tag{4.4}$$

where $(.)^t$ is the transposed operator. The norms associated with these inner products are defined as follows

$$\|\mathbf{s}\| = [\mathbf{s} : \mathbf{s}]^{1/2} = \sqrt{2\,J_2(\mathbf{s})} \tag{4.5}$$

$$\|\mathbf{e}\| = [\mathbf{e} : \mathbf{e}]^{1/2} = \sqrt{2\,J_2(\mathbf{e})} \tag{4.6}$$

where $J_2(\mathbf{s})$ and $J_2(\mathbf{e})$ are the second invariants of the stress and strain tensors.

4.3 Basic Constitutive Equations

The extremal surface is approximated by the Huber-Mises yield criterion [63], which is used in the model of small distortional elastic strains and finite plastic deformations. The extremal surface is defined by the equation

$$f(\mathbf{S},k) = \|\mathbf{S}\| - \sqrt{2}\,\kappa(\gamma_{eq}) = 0 \tag{4.7}$$

$$\gamma_{eq} = \int_0^t \dot{\gamma}_{eq}\, dt$$

$$\dot{\gamma}_{eq} = (2\mathbf{D}^P : \mathbf{D}^P)^{1/2} = \sqrt{2}\|\mathbf{D}^P\| \tag{4.8}$$

where **S** is the deviator of the Kirchhoff stress, γ_{eq} and $\dot{\gamma}_{eq}$ are the shear strain and the shear strain rate respectively.

The J_2 flow theory is assumed for the case when the sole mechanism of crystallographic multiple slip is responsible for plastic deformation. The contribution of mechanisms of crystallographic multiple slip is approximated by the following flow rule

$$\mathbf{D}_S^P = \frac{\sqrt{2}}{2}\dot{\gamma}_{eq}\,\hat{\mathbf{N}}, \tag{4.9}$$

$$\dot{\gamma}_{eq} = \sqrt{2}\,[\eta], \tag{4.10}$$

where $\hat{\mathbf{N}} = \frac{\mathbf{s}}{\|\mathbf{s}\|}$, $\mathbf{D}_S^P$ is the plastic deformation rate, $\dot{\gamma}_{eq}$ is the shear rate when crystallographic multiple slip is the sole mechanism for plastic deformation, $\hat{\mathbf{N}}$ is the unit vector normal to the surface defined by Eq. (4.7). Let **D** represents the total deformation rate expressed by

$$\mathbf{D} = \mathbf{D}^e + \mathbf{D}_S^P, \tag{4.11}$$

$$\mathbf{D} = (\mathbf{L}^{-1} + \frac{\alpha}{2h}\hat{\mathbf{N}}\otimes\hat{\mathbf{N}}):\overset{\circ}{\tau}, \qquad (4.12)$$

where $h = \frac{\partial \kappa}{\partial \gamma_{eq}}$ is the plastic hardening modulus, $\mathbf{L}$ is the elastic modulus, $\eta = \frac{\tau^{\circ}\cdot\hat{\mathbf{N}}}{2h}$

$[\eta] = \eta; \alpha = 1 \quad if \quad \eta > 0 \quad and \quad f = 0,$

$[\eta] = \eta; \alpha = 0 \quad if \quad \eta \le 0 \quad or \quad f < 0.$

The objective rate of any symmetric second order tensor t is given by

$$\overset{\circ}{t} = \overset{\bullet}{t} - \Omega^{e}t + t\Omega^{e}$$

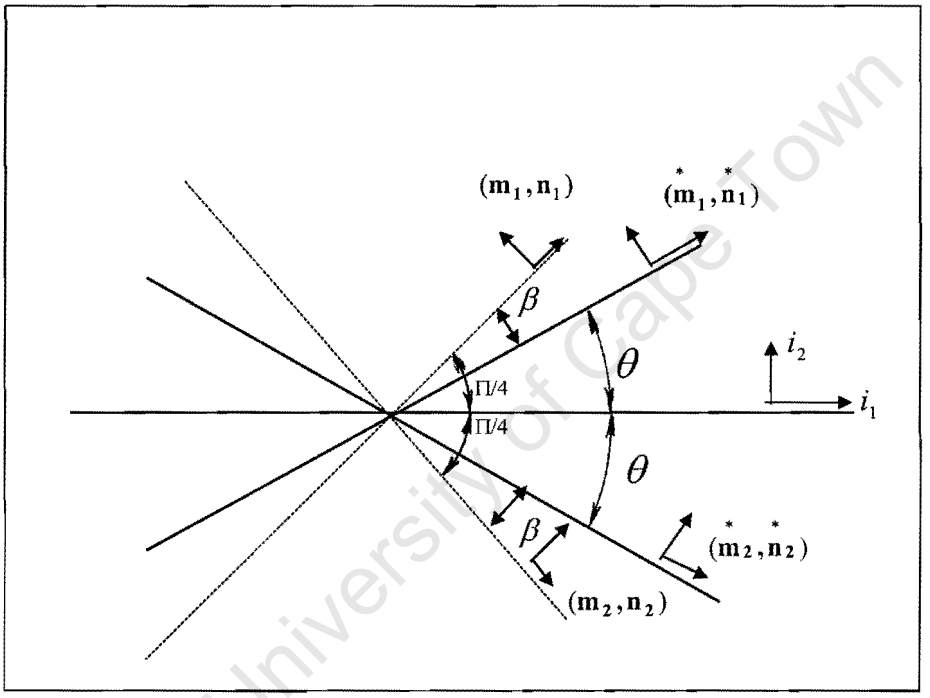

Figure 4.1 Geometry shows the double shear system in the extremal surface model

Following Pecherski [72], a double-shearing system normal to a flow plane is used to represent a contribution of active micro-shear bands. Directions $(\overset{*}{\mathbf{m}}_i, \overset{*}{\mathbf{n}}_i)$, i =1,2, of the double-shearing system represent the shear direction $\overset{*}{\mathbf{m}}_i$ while $\overset{*}{\mathbf{n}}_i$ is normal to a shear direction. The angle θ in Fig.(4.1) approximates the mean orientation of micro-shear bands and it is a crystalline parameter for a single crystal, which is statistically averaged for a polycrystalline aggregate. The compression direction is i_1.

The unit vectors $(\overset{*}{\mathbf{m}}_i, \overset{*}{\mathbf{n}}_i)$, i =1,2, are obtained directly from geometrical relations in Fig.(4.1) and can be written in terms of angle β and unit vectors $(\mathbf{m}_i, \mathbf{n}_i)$, i = 1,2, where β is the angle of rotation of planes of active micro-shear bands relative to planes of maximum shear stress. From Fig.(4.1) $\beta = \frac{\pi}{4} - \theta, \ \theta \in (0, \frac{\pi}{2})$ where θ is regarded as a crystal parameter which approximates the mean orientation of micro-shear bands.

The rate of plastic deformations and plastic spin produced by active micro-shear bands is given by

$$\mathbf{D}^{p}_{mb} = \sum_{i=1}^{2} \overset{\bullet}{\gamma}{}^{i}_{mb} (\overset{*}{\mathbf{m}}_i \otimes \overset{*}{\mathbf{n}}_i), \tag{4.13}$$

$$\mathbf{W}^{p}_{mb} = \sum_{i=1}^{2} \overset{\bullet}{\gamma}{}^{i}_{mb} (\overset{*}{\mathbf{m}}_i \otimes \overset{*}{\mathbf{n}}_i), \tag{4.14}$$

where $\overset{\bullet}{\gamma}{}^{i}_{mb}$ is the rate of plastic shearing along the i-th direction of shear. Using the geometrical relations Eq. (5.3) in [72], Eqs. (4.13) and (4.14) can be rewritten as:

$$\mathbf{D}^{p}_{mb} = \frac{\sqrt{2}}{2} \overset{\bullet}{\gamma}_{mb} (\mathbf{m}_1 + \mathbf{n}_1) + \frac{1}{2} \sin 2\beta \ (\sum_{i=1}^{2} \overset{\bullet}{\gamma}{}^{i}_{mb})(\mathbf{m}_1 \otimes \mathbf{m}_1 - \mathbf{n}_1 \otimes \mathbf{n}_1),$$

$$\mathbf{W}^{p}_{mb} = (\sum_{i=1}^{2} \overset{\bullet}{\gamma}{}^{i}_{mb})(\mathbf{m}_1 + \mathbf{n}_1), \ \overset{\bullet}{\gamma}_{mb} = \cos 2\beta \ (\sum_{i=1}^{2} \overset{\bullet}{\gamma}{}^{i}_{mb}).$$

The rate of plastic deformation can be expressed as an additive decomposition of two rates: one caused by mechanisms of crystallographic slip $\mathbf{D}^{p}_{S}$, and the second occurring due to the existence of micro-shear bands $\mathbf{D}^{p}_{mb}$,

$$\mathbf{D}^{p} = \mathbf{D}^{p}_{S} + \mathbf{D}^{p}_{mb}, \tag{4.15}$$

$$\overset{*\bullet}{\gamma} = \overset{\bullet}{\gamma}_{eq} + \overset{\bullet}{\gamma}_{mb}, \tag{4.16}$$

where $\overset{*\bullet}{\gamma}$ is the total plastic shearing rate, $\overset{\bullet}{\gamma}_{eq}$ is the shear rate from the crystallographic slip mechanism, and $\overset{\bullet}{\gamma}_{mb}$ is the rate of plastic shearing produced by micro-shear bands.

The unit normal vector to the yield surface $\hat{\mathbf{N}}$ and the unit orthogonal vector to it $\hat{\mathbf{T}}$ can be written in terms of double shearing directions [72]

$$\hat{\mathbf{N}} = \sqrt{2} \ (\mathbf{m}_1 \otimes \mathbf{n}_1), \tag{4.17}$$

$$\hat{\mathbf{T}} = \frac{\sqrt{2}}{2} (\mathbf{m}_1 \otimes \mathbf{m}_1 - \mathbf{n}_1 \otimes \mathbf{n}_1). \tag{4.18}$$

From the consistency condition $\overset{\bullet}{f}_{(\mathbf{S},k)} = 0$, the total shearing rate can be written as

$$\overset{\bullet}{\gamma}{}^{*} = \frac{\sqrt{2}}{2h} (\tau^{\circ} : \hat{\mathbf{N}}). \tag{4.19}$$

The orthogonal component $\hat{\mathbf{T}}$ can be written in terms of the normalizing factor Λ

$$\hat{\mathbf{T}} = \Lambda [\tau^{\circ\bullet} - (\tau^{\circ} : \hat{\mathbf{N}}) \hat{\mathbf{N}}]. \tag{4.20}$$

Following [72], the rate of plastic deformation $\mathbf{D}^{p}$ can be written in terms of active micro-shear fractions $f^{(1)}_{ms}$ and $f^{(2)}_{ms}$

$$\mathbf{D}^{p} = \frac{1}{2h} (\tau^{\circ} : \hat{\mathbf{N}}) \hat{\mathbf{N}} + \frac{\Lambda}{2h} (\tau^{\circ} : \hat{\mathbf{N}}) (f^{(1)}_{ms} - f^{(2)}_{ms}) \tan 2\beta \ [\tau^{\circ\bullet} - (\tau^{\circ} : \hat{\mathbf{N}}) \hat{\mathbf{N}}], \tag{4.21}$$

by substitution of Eqs. (4.19) and (4.20) into Eq.(4.21), $\mathbf{D}^P$ can be written in terms of $\hat{\mathbf{T}}$ and $\hat{\mathbf{N}}$ as

$$\mathbf{D}^P = \frac{\dot{\gamma}^*}{\sqrt{2}}[\,\hat{\mathbf{N}} + \hat{\mathbf{T}}(f_{ms}^{(1)} - f_{ms}^{(2)})\tan 2\beta\,]. \tag{4.22}$$

4.4 FINITE ELEMENT FORMULATION

The aim of this section is to develop an algorithm for evaluation of equivalent plastic strains accounting for micro-shear bands by means of double shearing system.

4.4.1 Algorithm of Evaluation of the Equivalent Plastic Strain

The deformation process is treated as a strain controlled process. The stress history is considered as a function of strain history. The elastic pivot stress $\mathbf{s}_{n+1}^T$ is computed from a converged solution at time $t = t_n$. If the resulting state defined by $\mathbf{s}_{n+1}^T$ lies outside of the elastic region enclosed by the yield surface $f(\mathbf{s},\alpha,\kappa) = 0$, the final state is defined as the closest-point projection of $\mathbf{s}_{n+1}^T$ onto the yield surface shown in Figs.(4.2(a)) and (4.2(b)). This can be summarized in the following two formulas

$$\mathbf{s}_{n+1}^T = \mathbf{s}_n + 2G\Delta\mathbf{e}_{n+1}, \tag{4.23}$$

$$\mathbf{s}_n = P(\mathbf{s}_{n+1}^T), \tag{4.24}$$

where $P: R^5 \to \partial C$ denotes the orthogonal projection onto elastic region C, with a compact set C and the yield surface $f(\mathbf{s},\alpha,\kappa) = 0$ as a boundary. The shear modulus G is related to the elastic modulus E and Poisson's ratio υ by

$$G = \frac{E}{2(1+\upsilon)}. \tag{4.25}$$

This procedure amounts to enforcing the consistency condition at the end of each time step and was first proposed by Wilkins [100], and developed by Simo [84], [85].

For an arbitrary convex yield function, the standard minimization problem with an associative flow rule and isotropic hardening aims at finding the minimum distance of a point representing the stress state to the Von-Mises yield surface.

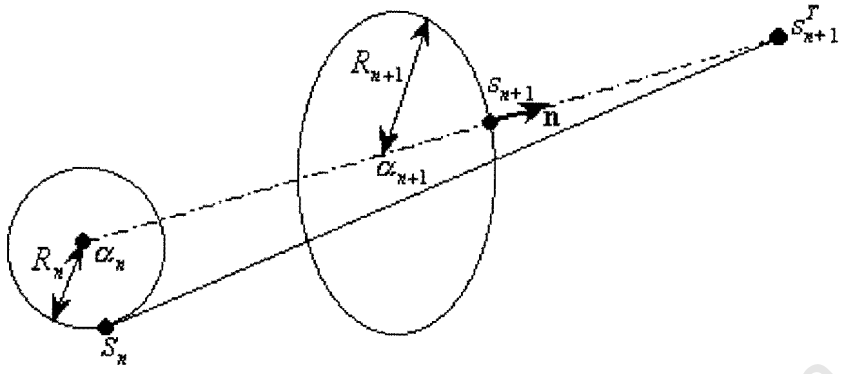

Figure 4.2(a) The closest-point projection of the pivot stress onto a yield surface in the case of nonlinear kinematic hardening

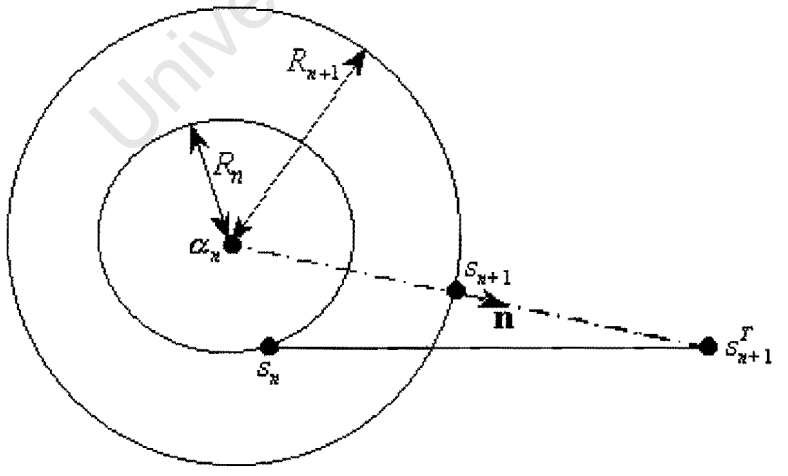

Figure 4.2 (b) The closest-point projection of the pivot stress onto the yield surface in the case of nonlinear isotropic hardening

Let $\hat{\mathbf{N}}$ denote the unit vector normal to a yield surface at the end of a typical time step $[t_n, t_{n+1}]$, then the normalization of the stress results in

$$\hat{\mathbf{N}} = \frac{\mathbf{s}^T_{n+1}}{\left\| \mathbf{s}^T_{n+1} \right\|} \tag{4.26}$$

The equivalent plastic shear rate at the end of time step $[t_n, t_{n+1}]$ can be computed using Eq.(4.8) and Eq.(4.22)

$$\overset{*}{\gamma}_{n+1} = \overset{*}{\gamma}_n + \int_{t_n}^{t_{n+1}} \sqrt{2}\ (\mathbf{D}^P : \mathbf{D}^P)^{\frac{1}{2}}\, dt, \tag{4.27}$$

$$\overset{*}{\gamma}_{n+1} = \overset{*}{\gamma}_n + \overset{*\bullet}{\gamma}\ (\hat{\mathbf{H}} : \hat{\mathbf{H}})^{\frac{1}{2}} \Delta t,$$

where $\hat{\mathbf{H}} = [\hat{\mathbf{N}} + \hat{\mathbf{T}}(f^{(1)}_{ms} - f^{(2)}_{ms}) \tan 2\beta\ ]$, $\hat{\mathbf{T}}$ and $\hat{\mathbf{N}}$ are orthogonal unit vectos $\hat{\mathbf{N}} : \hat{\mathbf{T}} = 0$, $\hat{\mathbf{N}} : \hat{\mathbf{N}} = 1$. Using this in Eq.(4.27) results in

$$\overset{*}{\gamma}_{n+1} = \overset{*}{\gamma}_n + \overset{*\bullet}{\gamma}\ \Delta t\ [1 + (f^{(1)}_{ms} - f^{(2)}_{ms})^2 \tan^2 2\beta\ ]^{\frac{1}{2}}. \tag{4.28}$$

Computation of residual functions $g(\overset{*\bullet}{\gamma}\ \Delta t)$ ***and*** $Dg(\overset{*\bullet}{\gamma}\ \Delta t)$

The stress $\mathbf{s}_{n+1}$ at the end of a step is computed from the pivot elastic stress $\mathbf{s}^T_{n+1}$ according to the equation

$$\mathbf{s}_{n+1} = \mathbf{s}^T_{n+1} - 2\overset{*\bullet}{\gamma}\ \Delta t G \hat{\mathbf{N}}, \tag{4.29}$$

where $\hat{\mathbf{N}}$ is the unit vector normal to the extremal surface. Substituting $\mathbf{s}^T_{n+1} = \hat{\mathbf{N}} \left\| \mathbf{s}^T_{n+1} \right\|$ and for $\mathbf{s}_{n+1} = \hat{\mathbf{N}} \left\| \mathbf{s}_{n+1} \right\|$ in Eq.(4.29) results in

$$\hat{\mathbf{N}} \left\| \mathbf{s}_{n+1} \right\| = \hat{\mathbf{N}} \left\| \mathbf{s}^T_{n+1} \right\| - 2\overset{*\bullet}{\gamma}\ \Delta t G \hat{\mathbf{N}} \tag{4.30}$$

Applying the consistency condition $\left\| \mathbf{s}_{n+1} \right\| = \sqrt{2}\kappa$ in Eq. (4.30) results in

$$\sqrt{2}\,\hat{\mathbf{N}}\,\kappa\ (\overset{*}{\gamma}) = \hat{\mathbf{N}} \left\| \mathbf{s}^T_{n+1} \right\| - 2\overset{*\bullet}{\gamma}\ \Delta t G \hat{\mathbf{N}}. \tag{4.31}$$

Multiplying both sides of Eq.(4.31) by $\hat{\mathbf{N}}$, and assuming $\hat{\mathbf{N}} : \hat{\mathbf{N}} = 1$, equations with scalars can be obtained

$$g(\overset{*\bullet}{\gamma}\ \Delta t) = -\sqrt{2}\ \kappa\ (\overset{*}{\gamma}) + \left\| \mathbf{s}^T_{n+1} \right\| - 2\overset{*\bullet}{\gamma}\ \Delta t G = 0, \tag{4.32}$$

$$Dg(\overset{*\bullet}{\gamma}\ \Delta t) = -\sqrt{2}\ \kappa^{\bullet}(\overset{*}{\gamma})\,\mathbf{X} - 2G, \tag{4.33}$$

with $\mathbf{X} = [1 + (f^{(1)}_{ms} - f^{(2)}_{ms})^2 \tan^2 2\beta\ ]^{\frac{1}{2}}$.

Table 4.1 Algorithm of evaluation of the equivalent plastic strain for the concept of kinematics of crystal deformation.

1. Begin
2. Form the deviatoric strain increment

$$\Delta \mathbf{e}_{n+1} = \Delta\varepsilon - \frac{1}{3}\mathrm{tr}\Delta\varepsilon$$

3. Calculate elastic predictor

$$\mathbf{s}^{T}_{n+1} = \mathbf{s}_{n} + 2G\Delta \mathbf{e}_{n+1},$$

4. Compute the unit normal $\hat{\mathbf{N}}$

$$\hat{\mathbf{N}} = \frac{\mathbf{s}^{T}_{n+1}}{\left\| \mathbf{s}^{T}_{n+1} \right\|}$$

5. Form the residual function

$$g(\overset{*\bullet}{\gamma}\ \Delta t) = -\sqrt{2}\ \kappa\ (\overset{*}{\gamma}\ ) \quad + \left\| \mathbf{s}^{T}_{n+1} \right\| - 2\overset{*\bullet}{\gamma}\ \Delta tG$$

6. Solve the residual equation in step 5 for $(\overset{*\bullet}{\gamma}\ \Delta t)$ using the Newton iteration method (Table 4.2),
7. Compute the equivalent plastic strain at t_{n+1}

$$\overset{*}{\gamma}_{n+1} = \overset{*}{\gamma}_{n} + \overset{*\bullet}{\gamma}\ \Delta t\ [\,1 + (f^{(1)}_{ms} - f^{(2)}_{ms})^{2} \tan^{2} 2\beta\ ]^{\frac{1}{2}}$$

8. Update the deviatoric stress tensor **s** at t_{n+1}

$$\mathbf{s}_{n+1} = \sqrt{2}\ \ \kappa(\overset{*}{\gamma}_{n+1})\hat{\mathbf{N}}$$

9. Add the elastic volume change

$$\sigma_{n+1} = \mathbf{s}_{n+1} + k\,\mathrm{tr}\,\Delta\varepsilon\,\mathbf{1}$$

10. Update $\mathbf{T}_{n+1} = \dfrac{\partial\tilde{\sigma}(\sigma_{n}, \varepsilon_{n}, \overset{*}{\gamma}_{n}, \varepsilon - \varepsilon_{n})}{\partial\,\varepsilon}\Big|_{\varepsilon = \varepsilon_{n+1}}$ for the contribution to the global stiffness matrix.
11. End

Table 4.2 Evaluation of $(\overset{*}{\gamma}\overset{\bullet}{}\ \Delta t)$ for the extremal surface concept of crystal deformation

Newton's iteration method is used to calculate $(\overset{*}{\gamma}\overset{\bullet}{}\ \Delta t)$.

1. $\overset{*k}{\gamma}_{n+1} = \overset{*k+1}{\gamma}_{n} + (\overset{*}{\gamma}\overset{\bullet}{}\ \Delta t)^k \ [\,1 + (f_{ms}^{(1)} - f_{ms}^{(2)})^2 \tan^2 2\beta\,]^{\frac{1}{2}}$

2. Calculate $g(\overset{*}{\gamma}\overset{\bullet}{}\ \Delta t)$

$$g(\overset{*}{\gamma}\overset{\bullet}{}\ \Delta t) = -\sqrt{2}\ \kappa\ (\overset{*}{\gamma}) + \left\| \mathbf{s}_{n+1}^{T} \right\| - 2\overset{*}{\gamma}\overset{\bullet}{}\ \Delta t G$$

3. Calculate $Dg(\overset{*}{\gamma}\overset{\bullet}{}\ \Delta t)$

$$Dg(\overset{*}{\gamma}\overset{\bullet}{}\ \Delta t) = -\sqrt{2}\ \kappa\ \overset{\bullet}{}(\overset{*}{\gamma})\ \mathbf{X} - 2G$$

$$\mathbf{X} = [\,1 + (f_{ms}^{(1)} - f_{ms}^{(2)})^2 \tan^2 2\beta\,]^{\frac{1}{2}}$$

4. $$(\overset{*}{\gamma}\overset{\bullet}{}\ \Delta t)^{k+1} = (\overset{*}{\gamma}\overset{\bullet}{}\ \Delta t)^k - \frac{g(\overset{*}{\gamma}\overset{\bullet}{}\ \Delta t)^k}{Dg(\overset{*}{\gamma}\overset{\bullet}{}\ \Delta t)^k}$$

5. If $\left| g(\overset{*}{\gamma}\overset{\bullet}{}\ \Delta t)^k \right| >$ tolerance value

Put $k+1 = k$ and go to 1

4.4.2 Evaluation of Tangent Moduli

This section contains a procedure for computation of tangent moduli. The method is consistent with the algorithm described in Tables 4.1 and 4.2. We assume that the increments of σ_n , $\overset{*}{\gamma}_n$, ε_n are known.

The expression for evaluation of $\tilde{\sigma}(\sigma_n, \varepsilon_n, \overset{*}{\gamma}_n, \varepsilon - \varepsilon_n)$ on step 9 in Table 4.1 takes the form

$$\tilde{\sigma}(\sigma_n, \varepsilon_n, \overset{*}{\gamma}_n, \varepsilon - \varepsilon_n) = K(tr\Delta\varepsilon_{n+1})\mathbf{1} + \mathbf{s}_{n+1}. \tag{4.34}$$

By substitution of $\mathbf{s}_{n+1}$ from step 8 in Table 4.1, $\tilde{\sigma}(\sigma_n, \varepsilon_n, \overset{*}{\gamma}_n, \varepsilon - \varepsilon_n)$ can be written as

$$\tilde{\sigma} = K(tr\Delta\varepsilon_{n+1})\mathbf{1} + \sqrt{2}\kappa(\overset{*}{\gamma}_{n+1})\,\hat{\mathbf{N}} = K(tr\Delta\varepsilon_{n+1})\mathbf{1} + R_{n+1}\hat{\mathbf{N}} \tag{4.35}$$

where $R_{n+1} = \sqrt{2}\,\kappa(\overset{*}{\gamma}_{n+1})$ is the radius of the yield surface. The tangent modulus $\mathbf{T}_{n+1}$ is defined as

$$\mathbf{T}_{n+1} = \frac{\partial\tilde{\sigma}(\sigma_n, \varepsilon_n, \overset{*}{\gamma}_n, \varepsilon - \varepsilon_n)}{\partial\varepsilon}\Big|_{\varepsilon = \varepsilon_{n+1}} . \tag{4.36}$$

The derivative of the normal unit vector $\hat{\mathbf{N}}$ relative to $\mathbf{s}$, according to Lemma (4.1) in [46], has the form

$$\frac{\partial \hat{\mathbf{N}}}{\partial \mathbf{s}} = \frac{1}{\|\mathbf{s}\|}[\mathbf{I} - \hat{\mathbf{N}} \otimes \hat{\mathbf{N}}]. \tag{4.37}$$

The direct use of the chain rule gives the following result

$$\frac{\partial [\operatorname{tr} \varepsilon_{n+1}]}{\partial \varepsilon_{n+1}} = 1, \tag{4.38}$$

$$\frac{\partial \mathbf{e}_{n+1}}{\partial \varepsilon_{n+1}} = \mathbf{I} - \frac{1}{3} \mathbf{1} \otimes \mathbf{1}. \tag{4.39}$$

Using Eq.(4.37) in addition to Eq.(4.38) and Eq.(4.39) results in

$$\mathbf{T}_{n+1} = K \mathbf{1} \otimes \mathbf{1} + 2G \frac{R_{n+1}}{\|\mathbf{s}^T_{n+1}\|}[\mathbf{I} - \frac{1}{3} \mathbf{1} \otimes \mathbf{1}] - 2G \frac{R_{n+1}}{\|\mathbf{s}^T_{n+1}\|} \hat{\mathbf{N}} \otimes \hat{\mathbf{N}} + \hat{\mathbf{N}} \otimes \frac{\partial R_{n+1}}{\partial \varepsilon_{n+1}}. \tag{4.40}$$

Computation of $\dfrac{dR_{n+1}}{d\varepsilon_{n+1}}$

Let $(f^{(1)}_{ms} - f^{(2)}_{ms}) = f^{ms}_{net}$ and differentiate the scalar equation in Eq.(4.32) using thechain rule with respect to ε_{n+1} gives

$$-\sqrt{2}\,\kappa^{\bullet}(\overset{*}{\gamma})\,\Delta t \left\{ \frac{\partial \overset{*\bullet}{\gamma}}{\partial \varepsilon_{n+1}} [1 + f^{ms^2}_{net} \tan^2 2\beta]^{\frac{1}{2}} + \overset{*\bullet}{\gamma} \frac{f^{ms}_{net} \tan^2 2\beta}{[1 + f^{ms^2}_{net} \tan^2 2\beta]^{\frac{1}{2}}} \frac{\partial f^{ms}_{net}}{\partial \varepsilon_{n+1}} \right\} \tag{4.41}$$

$$+ \frac{\partial \|\mathbf{s}^T_{n+1}\|}{\partial \varepsilon_{n+1}} - 2G\Delta t \frac{\partial \overset{*\bullet}{\gamma}}{\partial \varepsilon_{n+1}} = 0$$

Using the chain rule in Eq.(4.26) results in

$$\frac{\partial \|\mathbf{s}^T_{n+1}\|}{\partial \varepsilon_{n+1}} = \frac{\partial \|\mathbf{s}^T_{n+1}\|}{\partial \mathbf{s}_{n+1}} \frac{\partial \mathbf{s}_{n+1}}{\partial \varepsilon_{n+1}} = 2G \hat{\mathbf{N}}.$$

Substituting for $\dfrac{\partial \|\mathbf{s}^T_{n+1}\|}{\partial \varepsilon_{n+1}}$ in Eq.(4.41) and solving for $\Delta t \dfrac{\partial \overset{*\bullet}{\gamma}}{\partial \varepsilon_{n+1}}$ results in

$$-2G\hat{\mathbf{N}} = \Delta t \frac{\partial \overset{*\bullet}{\gamma}}{\partial \varepsilon_{n+1}} [-\sqrt{2}\kappa^{\bullet}(\overset{*}{\gamma}_{n+1})[1 + f^{ms^2}_{net} \tan^2 2\beta]^{\frac{1}{2}} - 2G]$$

$$-\sqrt{2}\kappa^{\bullet} \overset{*\bullet}{\gamma}\, \Delta t \left[\frac{f^{ms}_{net} \tan^2 2\beta}{[1 + f^{ms^2}_{net} \tan^2 2\beta]^{\frac{1}{2}}} \right] \frac{\partial f^{ms}_{net}}{\partial \varepsilon_{n+1}},$$

$$\Delta t \frac{\partial \overset{*\bullet}{\gamma}}{\partial \varepsilon_{n+1}} = \frac{2G\hat{\mathbf{N}} - \sqrt{2}\kappa^{\bullet}\overset{*\bullet}{\gamma}\Delta t\left[\dfrac{f_{net}^{ms}\tan^2 2\beta}{[\,1 + f_{net}^{ms2}\tan^2 2\beta\,]^{\frac{1}{2}}}\right]\dfrac{\partial f_{net}^{ms}}{\partial \varepsilon_{n+1}}}{[\sqrt{2}\,\kappa^{\bullet}(\overset{*}{\gamma}_{n+1})[\,1 + f_{net}^{ms2}\tan^2 2\beta\,]^{\frac{1}{2}} + 2G]},$$

$$\Delta t \frac{\partial \overset{*\bullet}{\gamma}}{\partial \varepsilon_{n+1}} = \frac{\hat{\mathbf{N}} - \sqrt{2}\kappa^{\bullet}\overset{*\bullet}{\gamma}\Delta t\left[\dfrac{f_{net}^{ms}\tan^2 2\beta}{2G[\,1 + f_{net}^{ms2}\tan^2 2\beta\,]^{\frac{1}{2}}}\right]\dfrac{\partial f_{net}^{ms}}{\partial \varepsilon_{n+1}}}{1 + \dfrac{\sqrt{2}\kappa^{\bullet}(\overset{*}{\gamma}_{n+1})[\,1 + f_{net}^{ms2}\tan^2 2\beta\,]^{\frac{1}{2}}}{2G}} \qquad (4.43)$$

Using the chain rule and Eq.(4.27) in $\mathbf{R}_{n+1} = \sqrt{2}\,\kappa(\overset{*}{\gamma}_{n+1})$

$$\frac{d\mathbf{R}_{n+1}}{d\varepsilon_{n+1}} = \frac{\partial \mathbf{R}_{n+1}}{\partial \overset{*}{\gamma}}\frac{\partial \overset{*}{\gamma}}{\partial \varepsilon_{n+1}},$$

$$\frac{d\mathbf{R}_{n+1}}{d\varepsilon_{n+1}} = \sqrt{2}\kappa^{\bullet}(\overset{*}{\gamma}_{n+1})\Delta t\left\{[1 + f_{net}^{ms2}\tan^2 2\beta\,]^{\frac{1}{2}}\frac{\partial \overset{*\bullet}{\gamma}}{\partial \varepsilon_{n+1}} + \overset{*\bullet}{\gamma}\left[\frac{f_{net}^{ms}\tan^2 2\beta}{2G[1 + f_{net}^{ms2}\tan^2 2\beta\,]^{\frac{1}{2}}}\right]\frac{\partial f_{net}^{ms}}{\partial \varepsilon_{n+1}}\right\} \qquad (4.44)$$

where $\kappa^{\bullet}(\overset{*}{\gamma}_{n+1}) = \dfrac{d\kappa(\overset{*}{\gamma}_{n+1})}{d\overset{*}{\gamma}}$, and $\Delta t \dfrac{\partial \overset{*\bullet}{\gamma}}{\partial \varepsilon_{n+1}}$ is defined in Eq.(4.43).

Substituting for $\dfrac{d\mathbf{R}_{n+1}}{d\varepsilon_{n+1}}$ from Eq.(4.44) into Eq.(4.40) the consistent form of the tangent moduli can be evaluated.

The operator in Eq.(4.40) is the consistent tangent modulus which is given to ABAQUS as 4×4 matrix in conventional 2-D strain compression analysis.

CHAPTER FIVE

RESULTS OF FE SIMULATIONS

5.1 INTRODUCTION

This chapter is devoted for numerical examples on shear bands and texture evolution. Modeling of shear bands formation in a single crystal under plain strain compression demonstrates an application of the rate dependent and extremal surface models. The internal variables models, and crystal constitutive models, used in the calculations are described in chapters three and four, where the internal variables are both scalars and tensors.

Section 5.2 contains simulations of Al-Cu (fcc), and (bcc) single crystals subjected to plain strain compression for the rate dependent model. A behavior of Al-Cu crystal is also simulated under a plain strain compression for the extremal surface model.

Section 5.3 contains an example of a copper single crystal, compressed in a channel die. A behavior of a single crystal is simulated both for the rate dependent and extremal surface models.

5.2 Plane strain compression of Al-Cu (fcc) and (bcc) single crystals.

Shear bands in a benchmark problem, considered in this thesis, is modeled for Al-Cu (fcc) and (bcc) crystal idealized by two slip systems, under plain strain compression. The model consists of a crystal undergoing double conjugate slip. The normal to a crystal interface lies in the compression direction. The initial orientation of a lattice is shown in Fig.(5.1).

The crystal is represented by five hundred sixty square, two-dimensional, plane-strain, four-nodded elements. The ratio of the initial width to the initial height $(\frac{W_o}{L_o})$ of the specimen is 0.51, with 28 elements in the height and 20 in the width direction. Fig.(5.3(a)) shows the initial mesh geometry of a crystallite body. Boundary conditions are applied to the model as follows: on the material face y=0, both the normal displacement and the shear traction vanish. Material faces x=0 and x=W_o are

traction-less. Finally, the top nodes subject to a uniform displacement boundary conditions, which results in shear free compression rate of 0.001/s (see Fig.(5.2)).

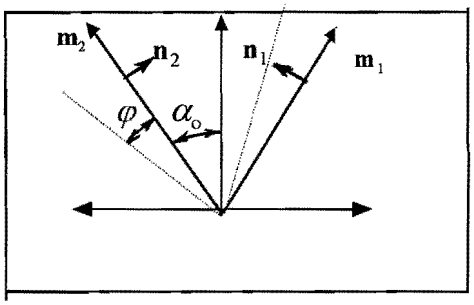

Figure 5.1 The initial lattice orientation of an Al-Cu fcc single crystal

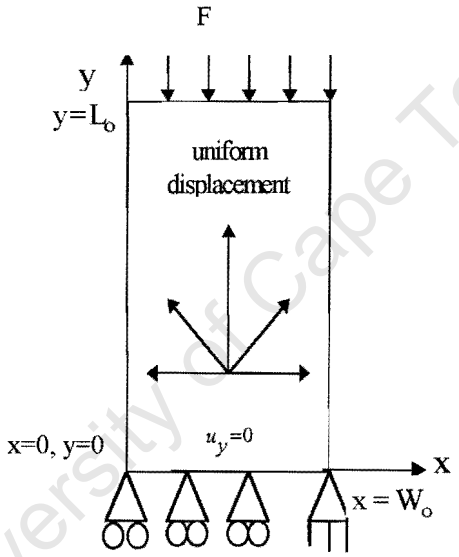

Figure 5.2 The boundary conditions applied to the Al-Cu single crystal model

Table 5.1 Elastic constants used for (fcc) and (bcc) simulations in terms of material yield limit τ_o.

C_{11}=1346 τ_o MPa	C_{12}=576.92 τ_o MPa	C_{44}=384.6 τ_o MPa

Results for the Al-Cu (fcc) crystal simulation for the rate dependent material model

The reference configuration of the two-dimensional single crystal model is depicted in Fig.(5.1), with α_o= 30° and the angle of rotation $\varphi = 1°$. This geometry serves as a model for fcc crystal in [79]. For a fcc crystal this is the angle that the primary and conjugate slip directions would make with the stable <112> tensile direction. The initial slip direction, **m,** and slip plane normals, **n**, are shown in Fig.(5.1).

In the simulation of the Al-Cu (fcc) crystal the following hardening rule is used:

$$\dot{\gamma}^{\alpha} = \dot{a}^{\alpha}\left[\frac{\tau^{\alpha}}{g^{\alpha}}\right]\left[\left|\frac{\tau^{\alpha}}{g^{\alpha}}\right|\right]^{(1/m)-1}, \qquad g^{\alpha}(\gamma) = \tau_o + \frac{h_o}{11.125}\tanh(11.125\gamma), \quad (5.1)$$

$$h(\gamma) = h_o \sec h^2(11.125\gamma). \quad (5.2)$$

where γ is the accumulated plastic strain, h_o represents the initial hardening rate, and τ_o is the yield stress. The above hardening equation has been used previously by Harren *et al.* [36] in their Taylor model calculations of large strain shearing of (fcc) crystals. This form fits adequately the hardening data of Chang and Asaro [23], which was obtained for Al-Cu single crystals subjected to tension along the <211> direction.

Elastic constants used in FE simulations are shown in Table 5.1. These constants were used by Peirce *et al.* in [75] for the fcc and bcc crystals calculations. The material parameters used in this simulation are tabulated in Table 5.2. These constants fit the hardening data for Al-Cu single crystals [36].

Table 5.2 Material parameters for an Al-Cu (fcc) crystal simulation.

$\dot{a}_o$=0.001/s	m=0.005	$h_o = 8.9\ \tau_o$

Figs.(5.4(c)), (5.5(c)), and (5.6(c)) show a lattice rotation, the values given corresponding to the rotation (in degrees) of the lattice away from the initial orientation shown in Fig.(5.1); positive values show clockwise rotation.

Deformed finite element meshes are shown in Fig.(5.3(b))-(5.3(d)), for various values of the compressive logarithmic strain $\varepsilon_{22} = -\ln(\frac{L}{L_o})$ with the current L and the initial length L_o of the finite element mesh along *y*-direction. Fig.(5.3(a)) shows the initial finite element mesh for $\varepsilon_{22} = 0.0$. Fig.(5.4(b)) shows the initial forming of the shear band across the crystal which grows more in Fig.(5.5(b)) and is completely formed in Fig.(5.6(b)).

The accumulated shear strain and the equivalent strain contour plots presented in Fig.(5.4(a)), (5.5(a)), and (5.6(a)), and (5.4(b)), (5.5(b)), and (5.6(b)), respectively, show the corresponding strain levels depicted in Figs.(5.3(b)), (c), and (d). The equivalent strain is defined by $\varepsilon = \sqrt{\varepsilon_1^2 + \varepsilon_2^2 + \varepsilon_3^2}/\sqrt{2}$, where $\varepsilon_1, \varepsilon_2$, and ε_3 are the principal logarithmic strains. Now, by the time when the strain level depicted by Fig.(5.3(b)) is reached, the deformation gets noticeably non-uniform, and the beginning of localized deformation is already evident. As seen in Fig.(5.4(a)) and (5.4(b)) the strains and the accumulated shear strains, in the area from the north-west to south-east, are noticeably high and range from 0.102 to 0.127 and from 0.217 to 0.27, respectively. When the strain depicted in Fig.(5.3(c)) is reached, the localized deformation in Fig.(5.5(a)) and (5.5(b)) gets more nonuniform and in the shear band

strip, the equivalent strain and the accumulated shear strain range from 0.167 to 0.211 and from 0.334 to 0.466, respectively. In Fig.(5.6(a)) and (5.6(b)), which correspond to Fig.(5.3(d)), the shear band is already formed across the specimen. The strain level and the accumulated shear strains in the localized strip are increasing and range from 0.215 to 0.385 and from 0.76 to 0.977, respectively. It is noticeable from Table 5.3 that the equivalent strain inside the localized zone is higher than the applied strain.

As can be seen from Fig.(5.4(c)), the beginning of the localized deformation is already evident, and it is seen that there is significant amount of non-uniform lattice reorientation. For instance, across the specimen from the north-west to south-east the lattice is rotated from 2° to 4°, and from Fig.(5.5(c)) the rotation increased from 4° to 10°, while in Fig.(5.6(c)) it exceeds 16°. The contour plots of the lattice rotation in Figs.(5.4(c)), (5.5(c)), and (5.6(c)), show that while the shear bands do not develop along crystallographic directions, the slip systems within the shear band tend to rotate in the positive direction to align with the band.

Table 5.3 The accumulated shear strain, the equivalent strain and the lattice rotation in the localized zone for various logarithmic strains of the Al-Cu fcc crystal for the rate dependent model.

Applied strain	Accumulated shear strain from - to	Equivalent strain from - to	Lattice rotation in degrees from - to
0.083	0.217-0.270	0.102-0.127	2.02-40.0
0.108	0.334-0.466	0.167-0.211	4.00-10.0
0.156	0.760-0.977	0.215-0.385	16.60-37.0

A comparison of the rate dependent calculations of Peirce *et al.* [75] with the present results of rate dependent calculations for a (fcc) crystal indicates some important conclusions, at least for a relatively low hardening crystal such as the one modeled here by hardening rule 5.2. The crystals develop shear bands exhibiting characteristic inclination of approximately 40° with respect to the tensile axis. This also agrees with experimental results conducted by Chang and Asaro [23] on Al-Cu crystals.

While not discernible in Fig.(5.4), a shear band pattern is evident in Fig.(5.5), which shows contour plots at equivalent strain 0.108. In Figs.(5.5(a)) and (5.5(b)), note how little additional straining has occurred in the upper right and lower left regions of the specimen in comparison with Fig.(5.4). Nearer to the specimen center, however, strain has begun to concentrate in a well–defined band. The lattice continues to rotate inside the band zone and rotations are greater than 10°. This behavior is quite similar to the results obtained by Peirce *et al.* [75] and Bronkhorst *et al.* [17] for the fcc crystal simulation. The phenomenology just described is in very close agreement with available experimental work of Chang and Asaro [23] on symmetrically oriented crystals of an aluminum alloy.

Contours of lattice rotations illustrate that, while the shear bands do not develop along crystallographic directions, the slip systems within the shear band tend to rotate to align with the band. Lattice rotations compare favorably with the solution of Lemonds *et al.* [55] and Peirce *et al.* [75].

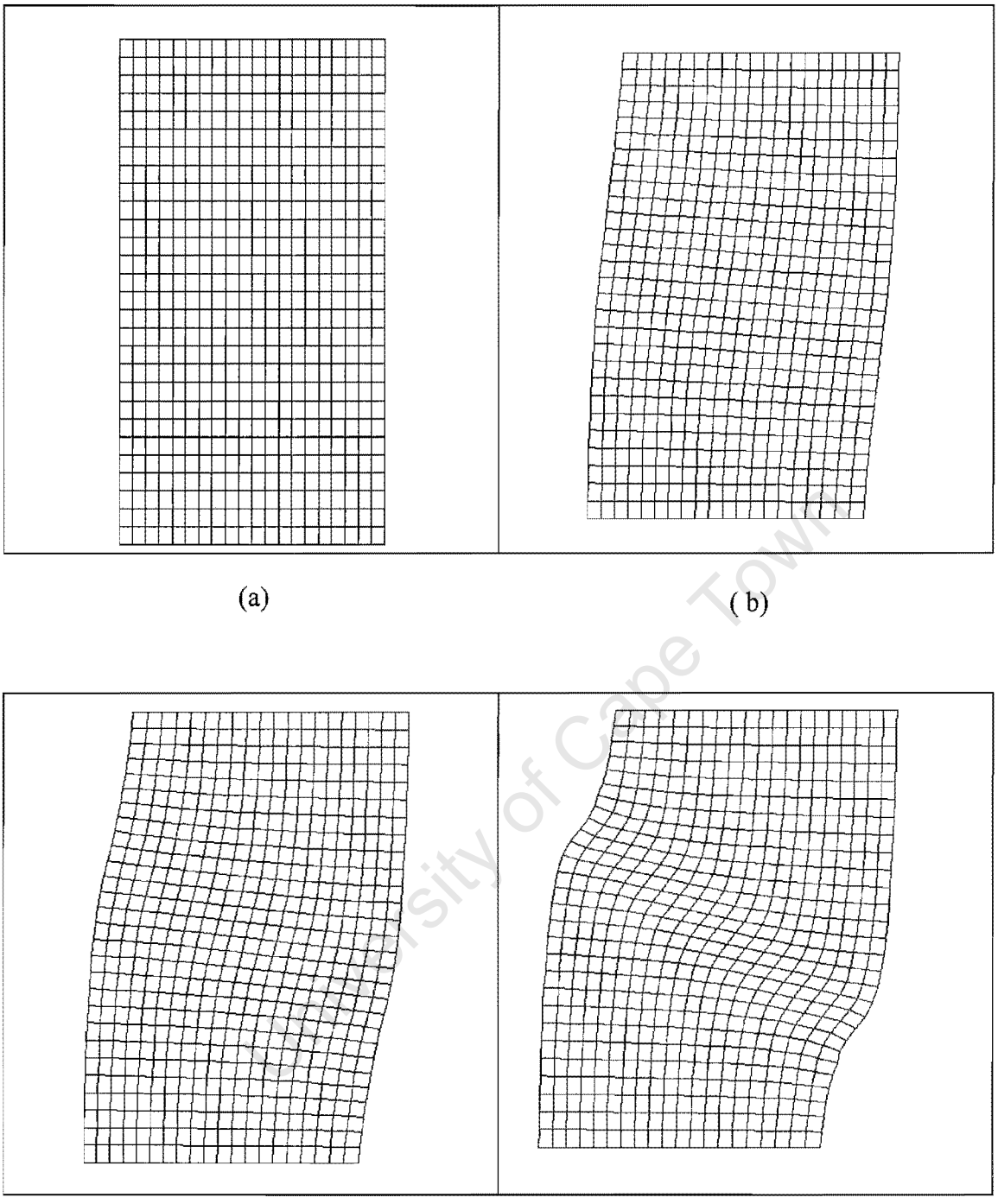

Figure 5.3 Deformed meshes from the finite element calculation of the (fcc) crystal for the rate dependent model. (a) ε_{22}=0.0, (b) ε_{22}=0.083, (c) ε_{22}=0.108, (d) ε_{22}=0.156.

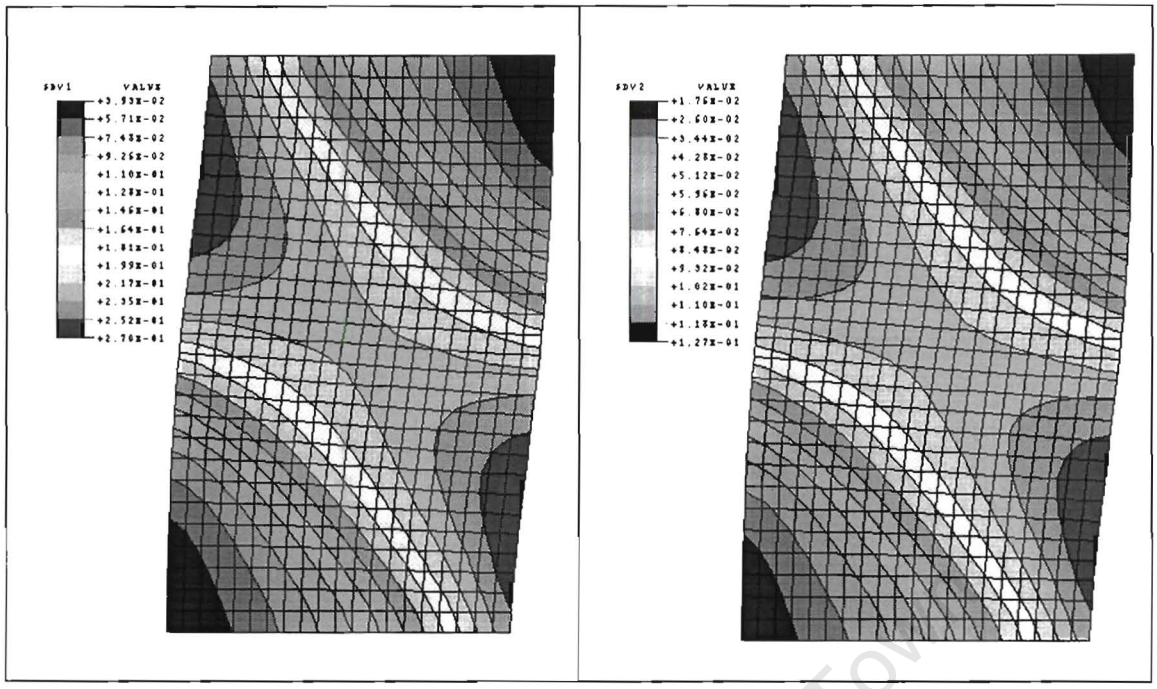

(a) (b)

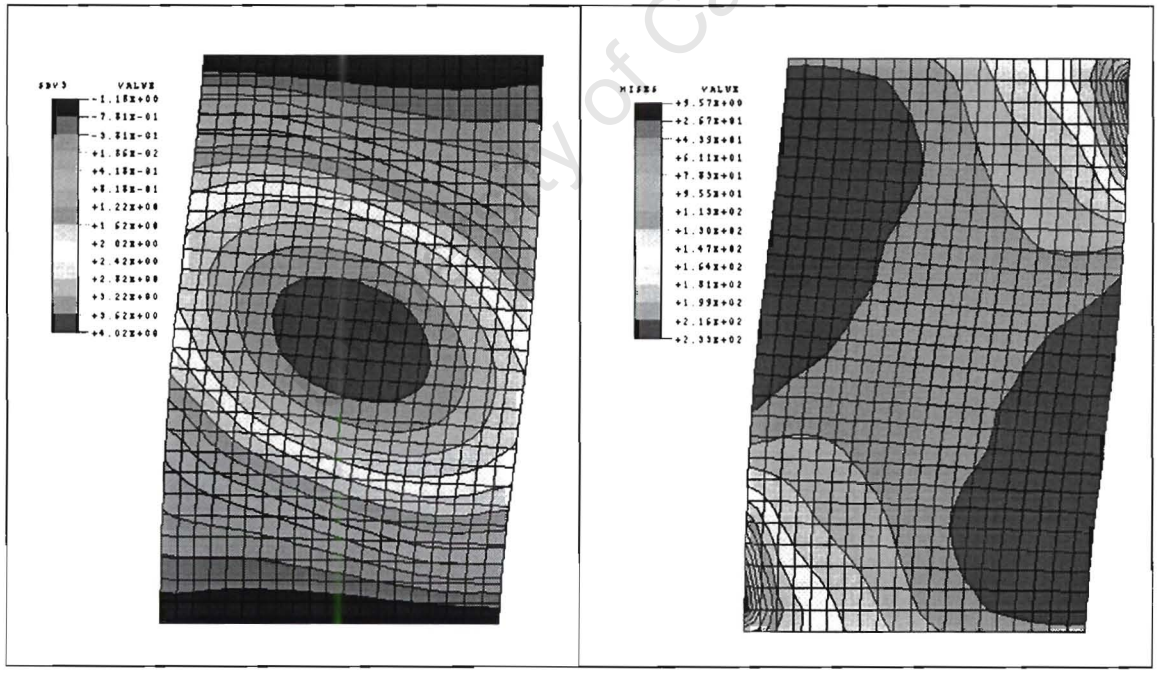

(c) (d)

Figure 5.4 (a) Contours of accumulated slip; (b) contours of equivalent strain; (c) contours of lattice rotations; (d) contours of the von Mises stress, for the strain value ε_{22} =0.083 for an Al-Cu (fcc) deformed crystal shown in Fig.(5.3(b)) for the rate dependent model.

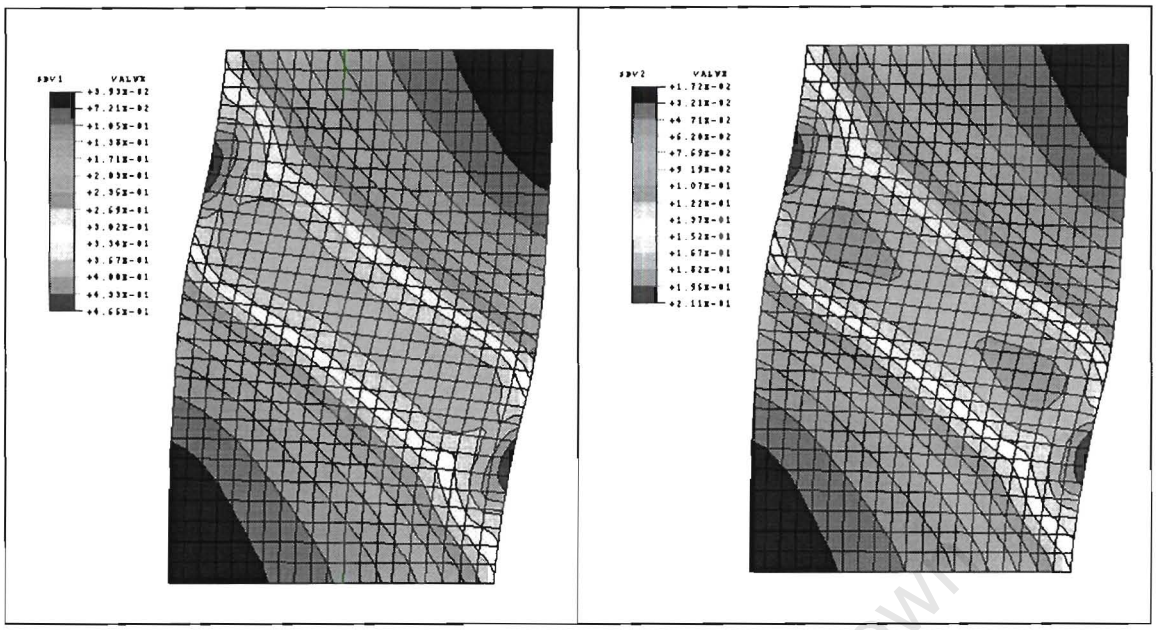

(a) (b)

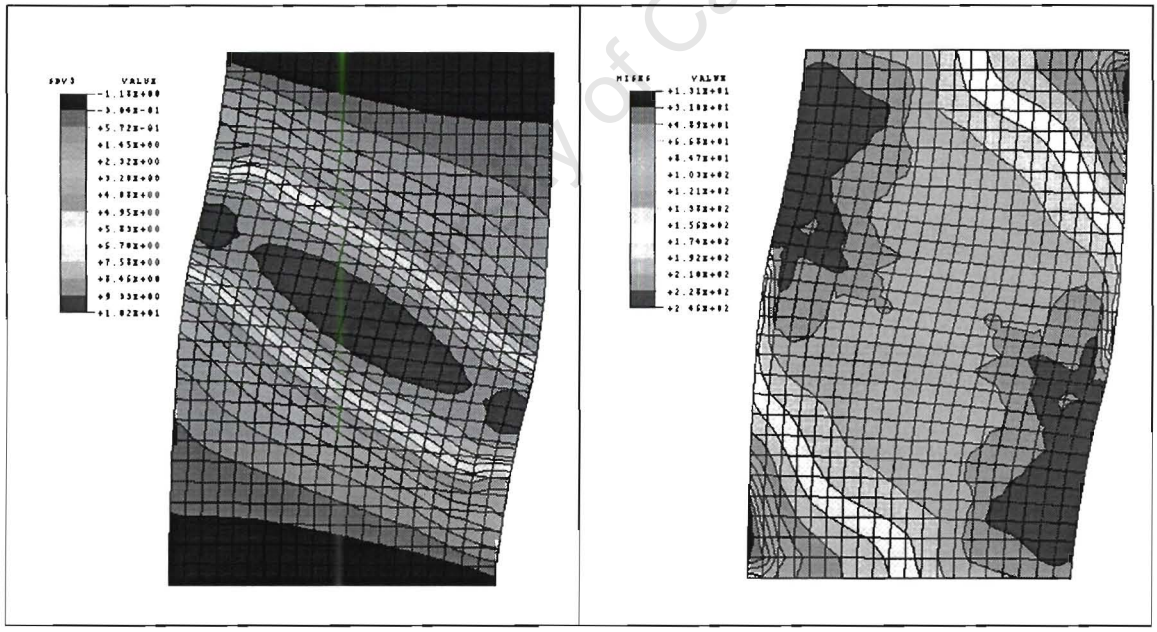

(c) (d)

Figure 5.5 (a) Contours of accumulated slip; (b) contours of equivalent strain; (c) contours of lattice rotations; (d) contours of the von Mises stress, for the strain value ε_{22} =0.108 for an Al-Cu (fcc) deformed crystal shown in Fig.(5.3(c)) for the rate dependent model.

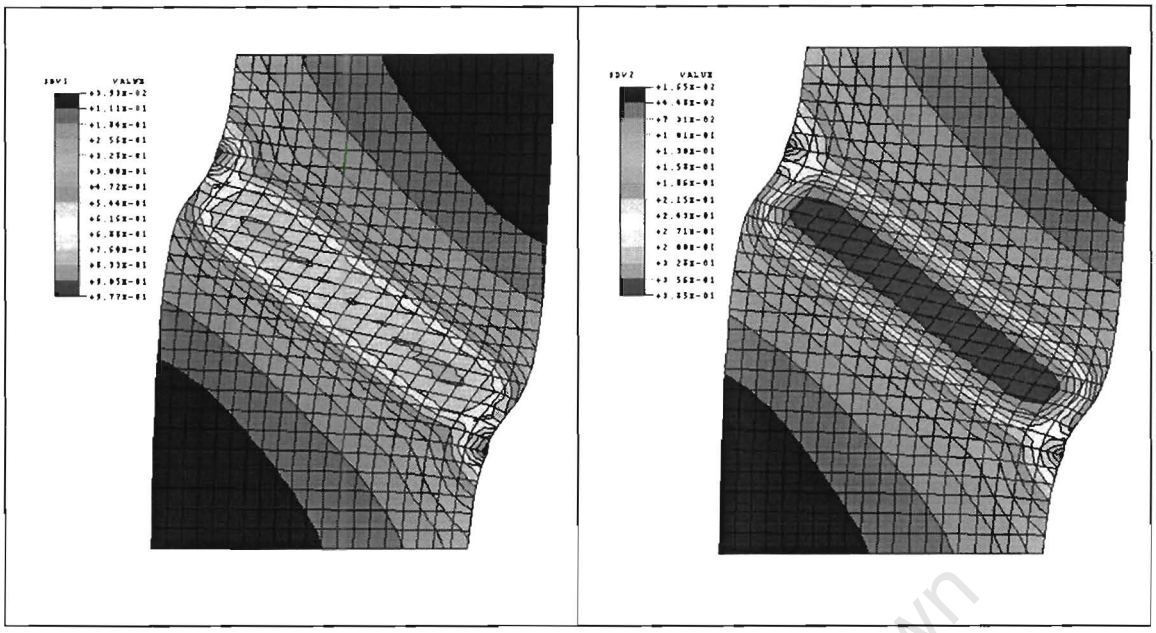

(a) (b)

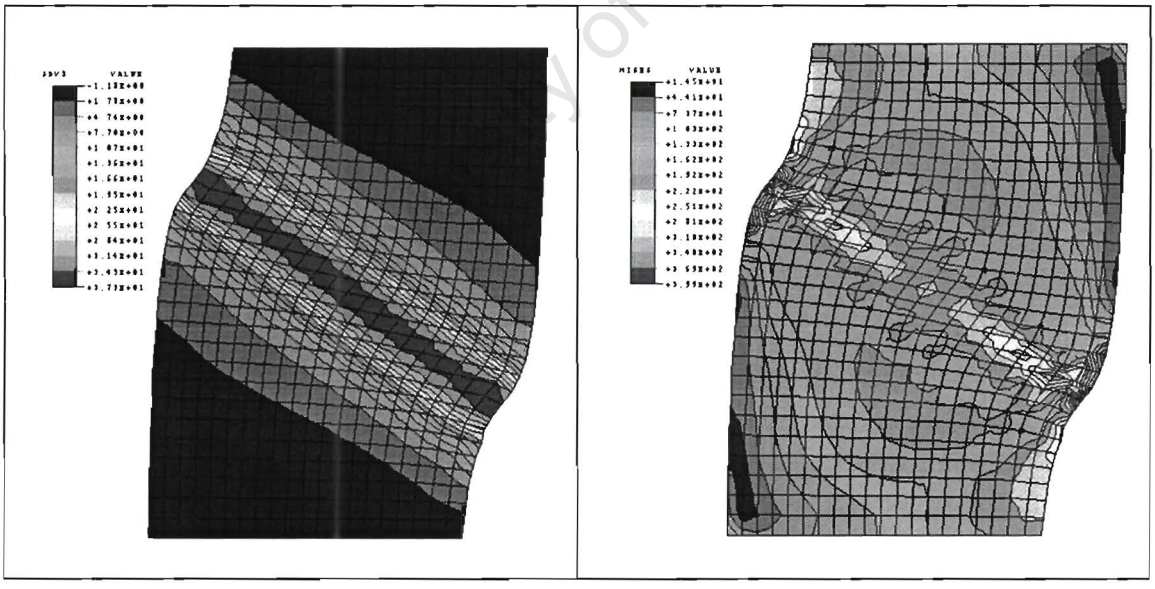

(c) (d)

Figure 5.6 (a) Contours of accumulated slip; (b) contours of equivalent strain; (c) contours of lattice rotations; (d) contours of the von Mises stress, for the strain value ε_{22} =0.156 for an Al-Cu (fcc) deformed crystal shown in Fig.(5.3(d)) for the rate dependent model.

Results for the (bcc) crystal simulations for the rate dependent material model:

The reference configuration of the two-dimensional single crystal model is shown in Fig.(5.1), with $\alpha_\circ = 60^\circ$ and angle of rotation $\varphi = 1^\circ$. This orientation can be used to model (bcc) crystals as tested by Reid *et al.* [79].

The hardening rule used in the simulation of bcc crystal is:

$$\dot{\gamma}^{\alpha} = \dot{a}^{\alpha}\left[\frac{\tau^{\alpha}}{g^{\alpha}}\right]\left[\left|\frac{\tau^{\alpha}}{g^{\alpha}}\right|\right]^{(1/m)-1},$$

$$g^{\alpha}(\gamma) = \tau_\circ + \frac{h_\circ}{200.}\tanh(200.\gamma), \text{ and } \quad h(\gamma) = h_\circ \operatorname{sech}^2(200.0\gamma).$$

The elastic constants used are the same as in Table 5.1. The material parameters tabulated in Table 5.4, used in this simulation, are identical to the bcc crystal simulation in Peirce *et al.* [75]. The material properties were chosen to give a resolved shear-stress/shear-strain curve with high initial hardening that rapidly saturated. As our numerical results will show, the development of localized plastic flow and shear bands orientations in this calculation is quite different from that in the (fcc) model crystal.

Table 5.4 Material parameters for the (bcc) single crystal simulation.

$\dot{a}_\circ$ =0.001/s	m=0.005	$h_\circ = 40\ \tau_\circ$

The undeformed finite element mesh is the same as used for the (fcc) crystal simulation Fig.(5.3(a)). The deformed meshes for the plane strain compression are shown in Figs.(5.7(a)), (5.7(b)), (5.7(c)), and (5.7(d)) for various strains ε_{22}. Figs.(5.8), (5.9), (5.10), and (5.11) show contours of the accumulated shear strain, the equivalent strain, lattice rotations, and the von Mises stress corresponding to the deformed mesh.

Fig.(5.7(a)) shows the beginning of the non-uniform deformation in the expected shear band zone. Figs.(5.7(b)), (5.7(c)), and (5.7(d)) show the initiation of shear bands. In Fig.(5.7(c)) a shear band is more evident, but not as sharp as in the fcc model Fig.(5.3(d)). The shear band is getting sharper for higher displacement in Fig.(5.7(d)).

The accumulated shear strain and the equivalent strain contours presented in Figs.(5.8(a)), (5.8(b)), (5.9(a)), (5.9(b)), (5.10(a)), (5.10(b)), (5.11(a)), and (5.11(b)) show that there is a noticeable rate of strain localization in the shear band zone, and deformation is nonuniform. Table 5.5 shows that concentration of localization increases in the shear band zone as the displacement increases (see Figs.(5.8(a)), (5.8(b)) - (5.11(a)), (5.11(b))), and that strains inside the localized zone are significantly higher than applied strains. It is noticeable that the localized strip is wider than one in the case of the (fcc) crystal model in Figs.(5.6(a)) and (5.6(b)). Localization of accumulated shear-strains and equivalent strains is also less pronounced than in the (fcc) crystal simulation.

Table 5.5 The accumulated shear-strain, the equivalent strain and a lattice rotation in a shear band zone for various logarithmic strains of the (bcc) crystal simulation for the rate dependent model.

Applied strain	Accumulated shear strain from - to	Equivalent strain from - to	Lattice rotation (in degrees) from - to
0.083	0.207-0.379	0.0735-0.163	(-4.42) - (-13.4)
0.108	0.246-0.526	0.1060-0.290	(-5.06) - (-18.5)
0.156	0.342-0.733	0.1430-0.320	(-7.72) - (-22.2)
0.260	0.707-1.170	0.2450-0.449	(-8.83) - (-24.6)

In the simulation with the (bcc) crystal, Fig.(5.7(d)) shows that localized shearing becomes evident at larger end displacements. However, a well-defined sharp localized shear band was not developed in this case. This is in contrast with the behavior exhibited for the (fcc) geometry's.

The beginning of the non-uniform localization of deformation is as in the (fcc) model accompanied by a significant non-uniform lattice re-orientation. The rotation is significantly larger in the shear strip than in other areas of the specimen. Contours of a lattice rotation in Figs.(5.8(c))-(5.12(c)), and Table 5.5 show that slip systems within the shear band tend to rotate in the negative direction to align with the band. The lattice rotations compare favorably with solutions by Lemond *et al.* [55], Peirce *et al.* [75] and Harren *et al.* [36].

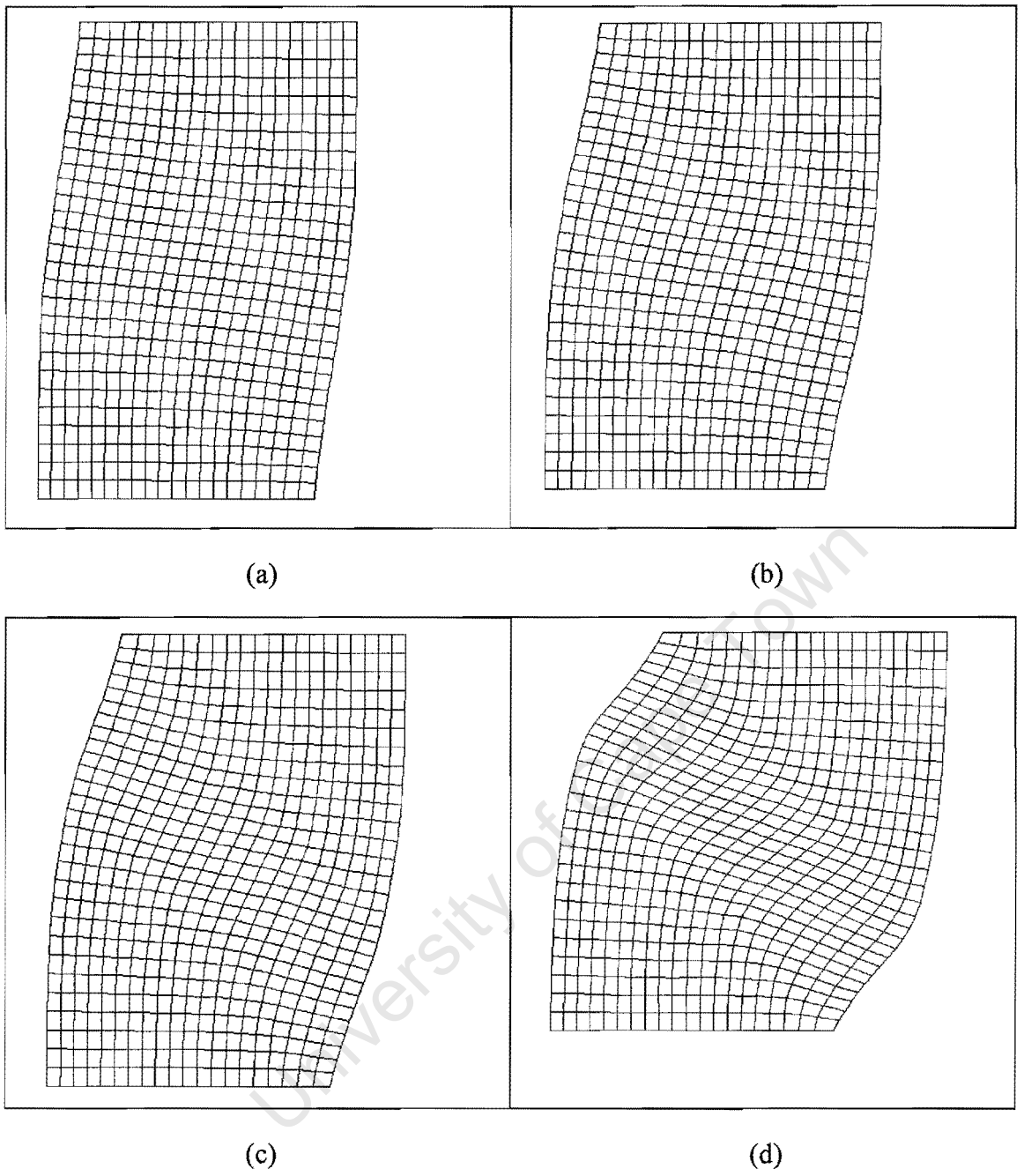

Figure 5.7 Deformed finite element meshes for the (bcc) crystal for the rate dependent model. (a) ε_{22}=0.083, (b) ε_{22}=0.108, (c) ε_{22}=0.156, (d) ε_{22}=0.26.

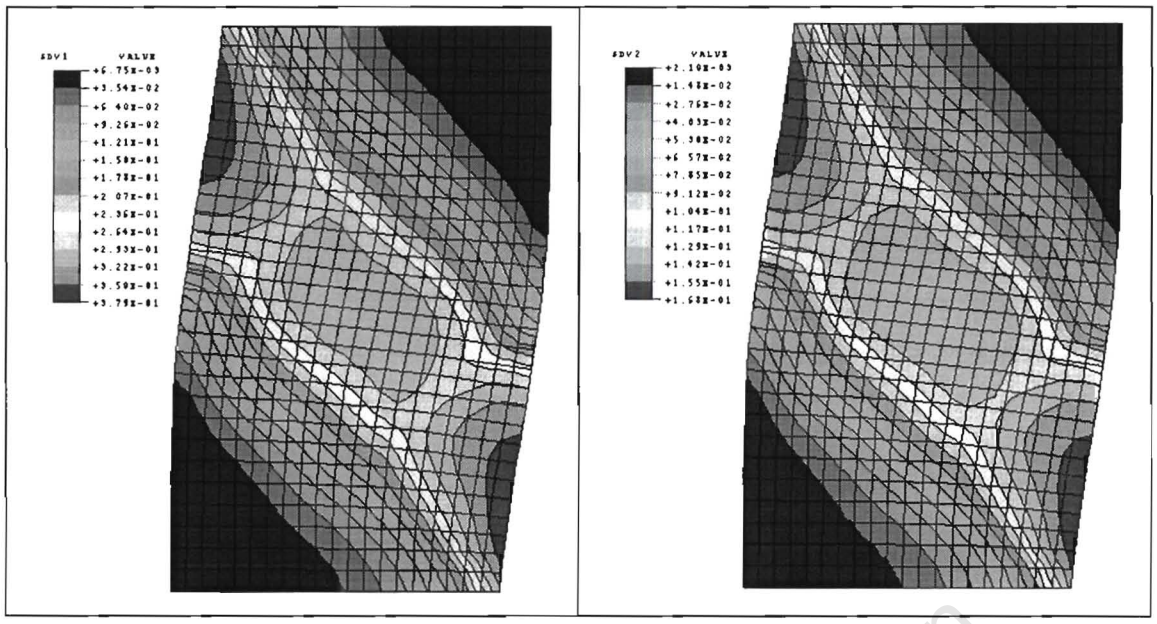

(a)

(b)

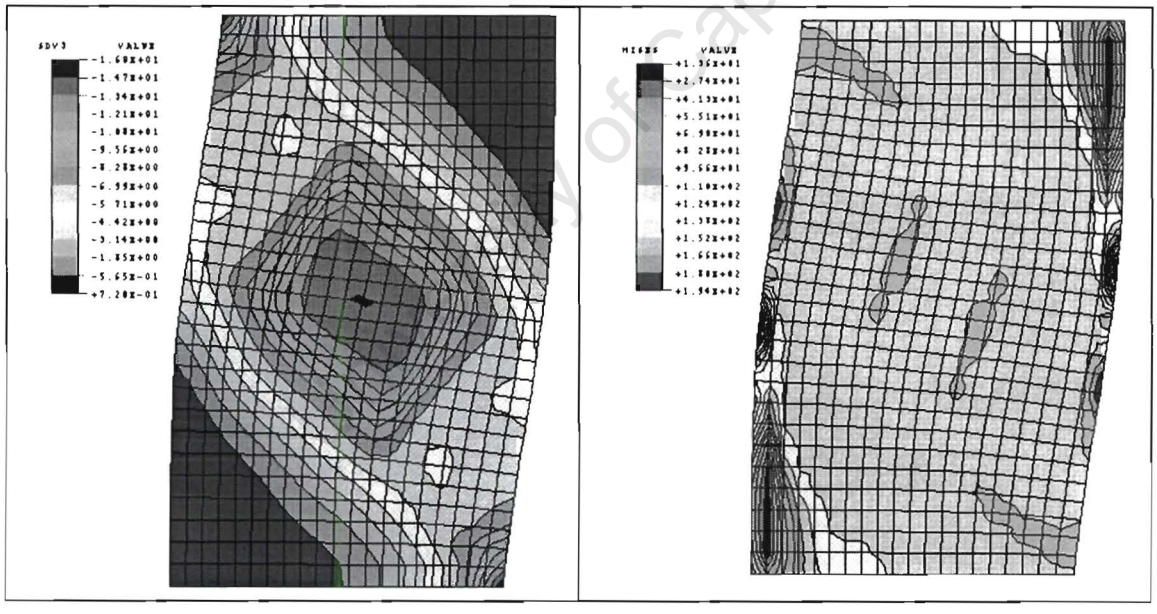

(c)

(d)

Figure 5.8 (a) Contours of accumulated slip; (b) contours of equivalent strain; (c) contours of lattice rotations; (d) contours of the von Mises stress, for the strain value ε_{22}=0.083 for the (bcc) deformed crystal shown in Fig.(5.7(a)) for the rate dependent model.

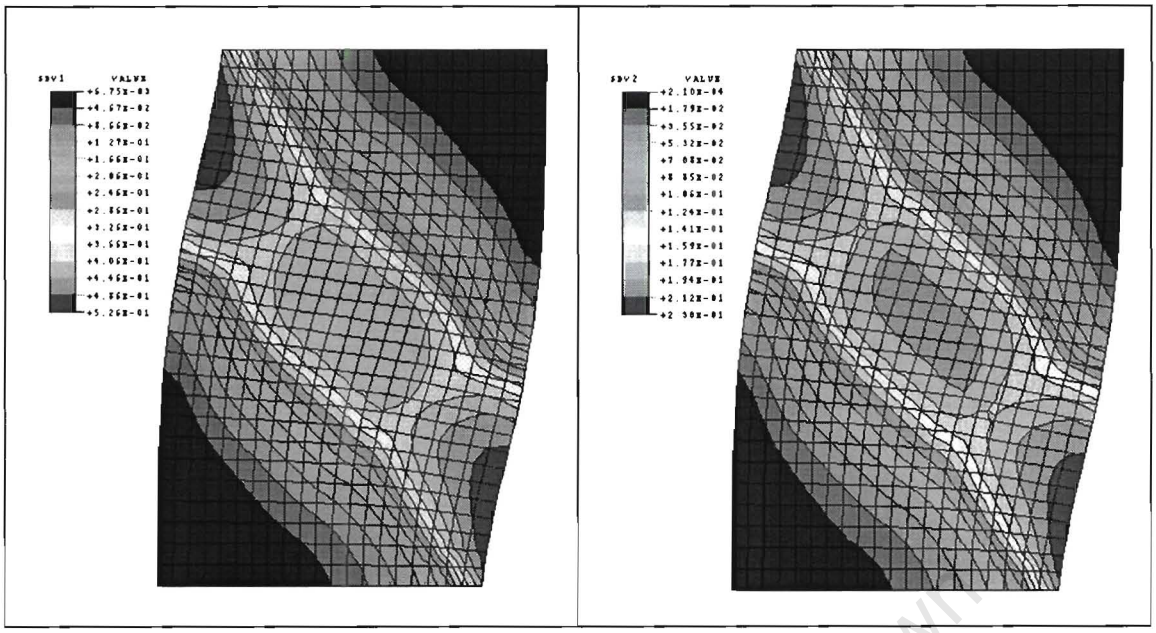

(a) (b)

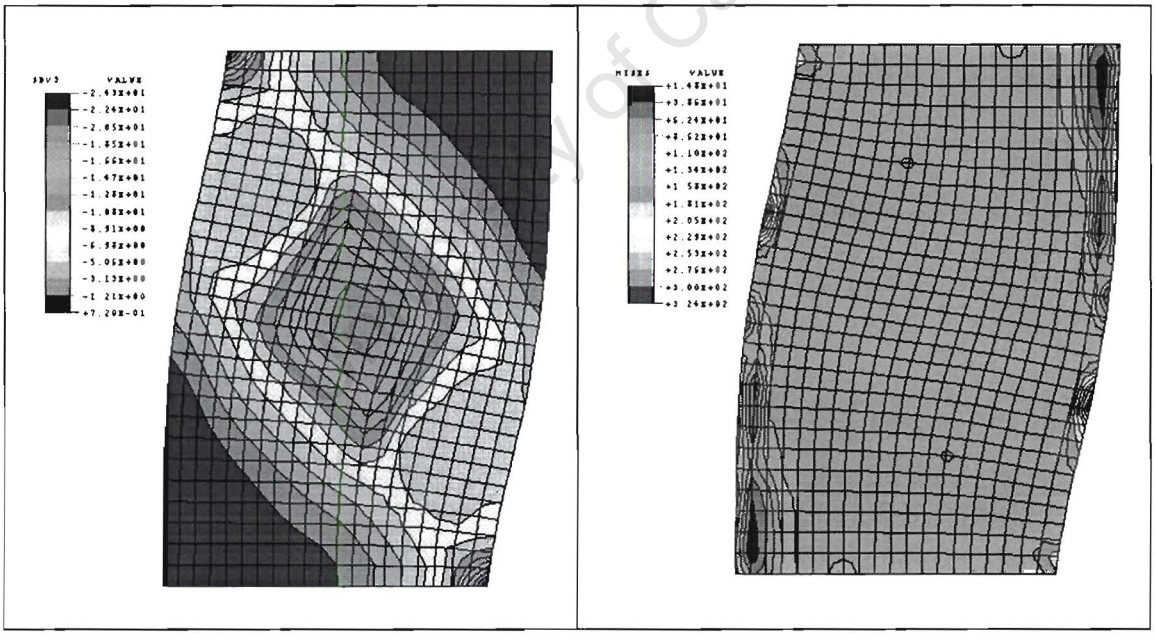

(c) (d)

Figure 5.9 (a) Contours of accumulated slip; (b) contours of equivalent strain; (c) contours of lattice rotations; (d) contours of the von Mises stress for the strain ε_{22} =0.108 of the (bcc) deformed crystal shown in Fig.(5.7(b)) for the rate dependent model.

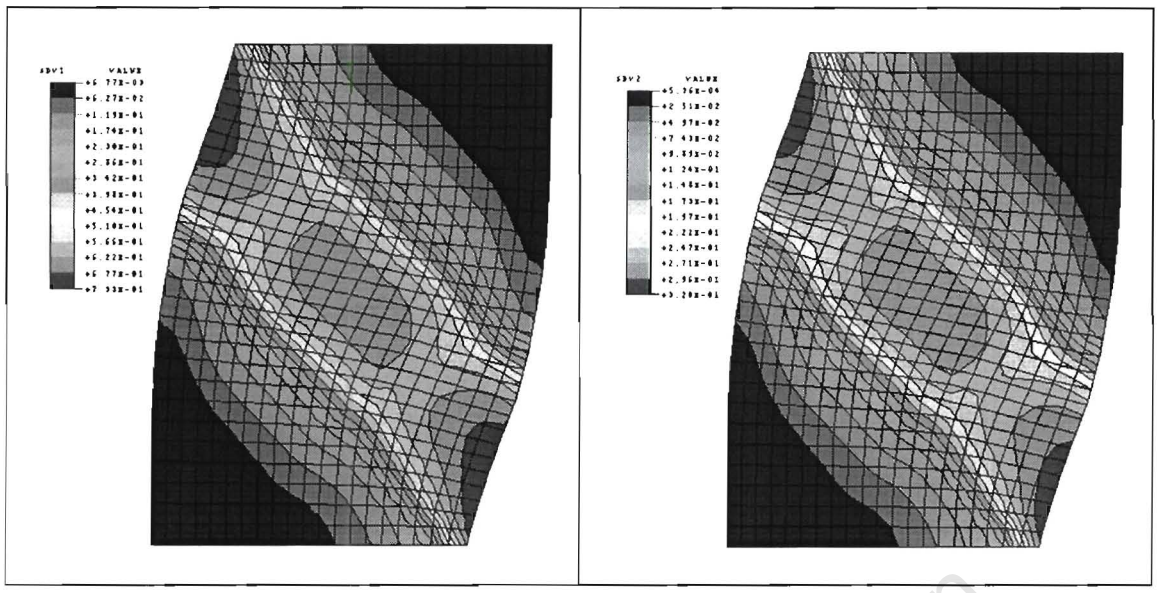

(a) (b)

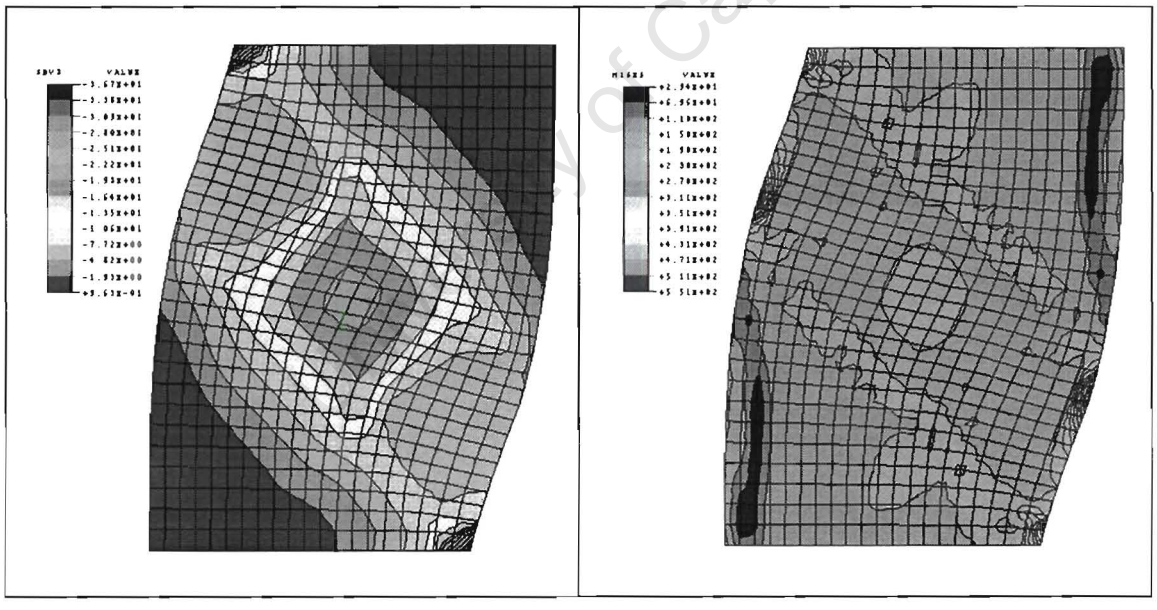

(c) (d)

Figure 5.10 (a) Contours of accumulated slip; (b) contours of equivalent strain; (c) contours of lattice rotations; (d) contours of the von Mises stress for the strain ε_{22} =0.156 of the (bcc) deformed crystal shown in Fig.(5.7(c)) for the rate dependent model.

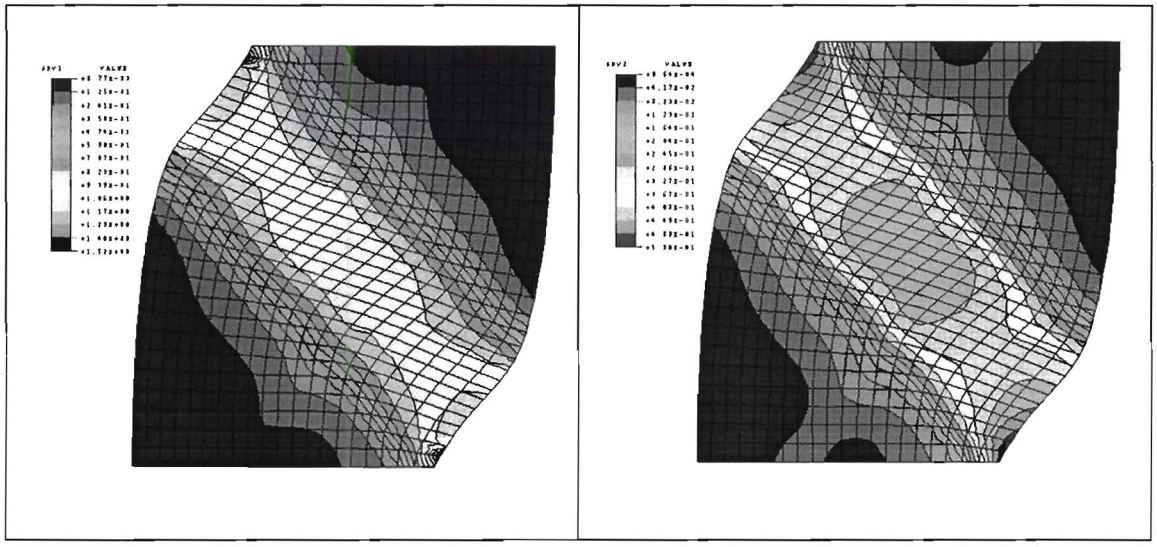

(a) (b)

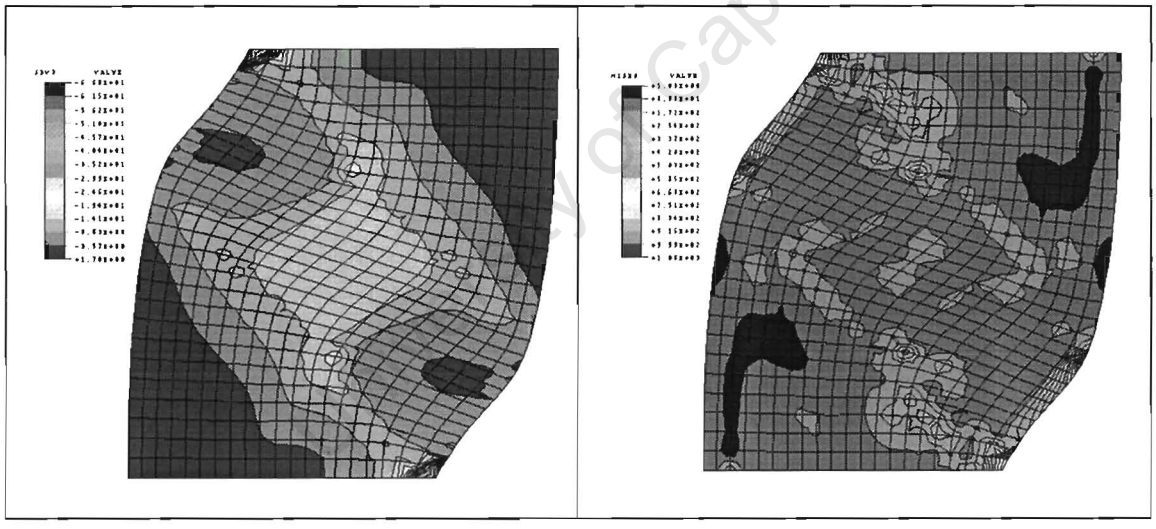

(c) (d)

Figure 5.11 (a) Contours of accumulated slip; (b) contours of equivalent strain; (c) contours of lattice rotations; (d) contours of the von Mises stress for the strain ε_{22} =0.26 of the (bcc) deformed crystal shown in Fig.(5.7(d)) for the rate dependent model.

Results of the simulation for the Al-Cu single crystal deformation: Rate Independent (External surface) Model.

The reference configuration of a crystal subject to two-dimensional compression considered here is the same as for the simulation of Al-Cu crystal deformation for the rate dependent constitutive relations. In this model slip directions and a rotation angle are no longer needed. The crystalline variable $\beta = \frac{\pi}{4} - \theta$, with a crystalline parameter $\theta \in (0, \frac{\pi}{2})$ which approximates the mean orientation of micro-shear bands is applied. The angle θ is equal to $44.5°$. The nett fraction is given by

$F_{ms}^{net} = \frac{A}{(1+e^{B-c|\varepsilon|})}$, where A=0.9, B=6.5, and C=11.8

The hardening law for the Al-Cu single crystal compression is:

$$\kappa = \tau_o + \frac{8.9\tau_o}{11.125}\tanh(11.125\gamma).$$

Elastic constants are the same as given in Table 5.1, that correspond to Young's modulus E=1000 τ_o, and Poisson's ratio υ=0.3.

In this rate independent constitutive model a rate of plastic shearing is determined by applying the consistency condition (see Table 4.1), so the evolution equation of a rate of plastic shearing is no longer applied.

Deformed finite element meshes for the plain strain compression are shown in Figs.(5.12(a)), (5.12(b)), (5.12(c)), and (5.12(d)) for various ε_{22}. In Fig.(5.12(c)) a shear band formation is clear, but it is not sharp as well as for the (fcc) rate dependent formulation shown in Fig.(5.3(d)), and it is more close to the (bcc) simulation in Fig.(5.7(c)). The shear band becomes sharper as a strain increases as can be seen in Fig. 5.12(d).

Figs.(5.13-5.15) show contours of the accumulated plastic strain, the equivalent strains, the nett fraction internal variable, and the von Misses stress that correspond to a deformed mesh shown in Fig.(5.12).

The localized strip in this simulation (see Figs.(5.13(a),(b))-(15(a),(b))) is significantly wider than one in the case obtained for the simulation with the rate dependent crystal model.

Table 5.6 The accumulated plastic strain, the equivalent strain and a nett fraction in a shear band zone for various logarithmic strains of a single crystal simulation for the concept with the extremal surface.

Applied strain	Accumulated plastic strain from - to	Equivalent strain from - to	Nett fraction from - to
0.083	0.173-0.254	0.0829-0.122	0.0102-0.0149
0.108	0.263-0.373	0.0997-0.198	0.0156-0.0332
0.156	0.309-0.670	0.1470-0.295	0.4100-0.1000
0.260	0.515-1.570	0.2370-0.490	0.1570-0.4990

The accumulated plastic strain and the equivalent strain contours presented in Figs.(5.13(a),(b))-(15(a),(b)) show that there is a noticeable rate of strain localization in the shear-band zone compared to other parts of a specimen, and deformation there is non-uniform. Table 5.6 and Figs.(5.12(a))-(5.12(d)) show that concentration of localization increases significantly in a shear band zone as displacement increases. It is noticeable that a localized strip is wider than in the case of the fcc crystal model and similar to one in the case of the bcc model. A rate of localization of accumulated shear strains and equivalent strains is less than the ones in the fcc and bcc crystals simulations. It is noticeable that shear band develops more rapidly in a thinner zone for the rate dependent simulation of the Al-Cu crystal than in the extremal surface model simulation. The phenomenology just described shows that the rate dependent simulation is in a closer agreement with computational results of Peirce *et al.* [75], and experimental results conducted by Chang and Asaro [23] and Embury *et al.* [32] on Al-Cu crystals.

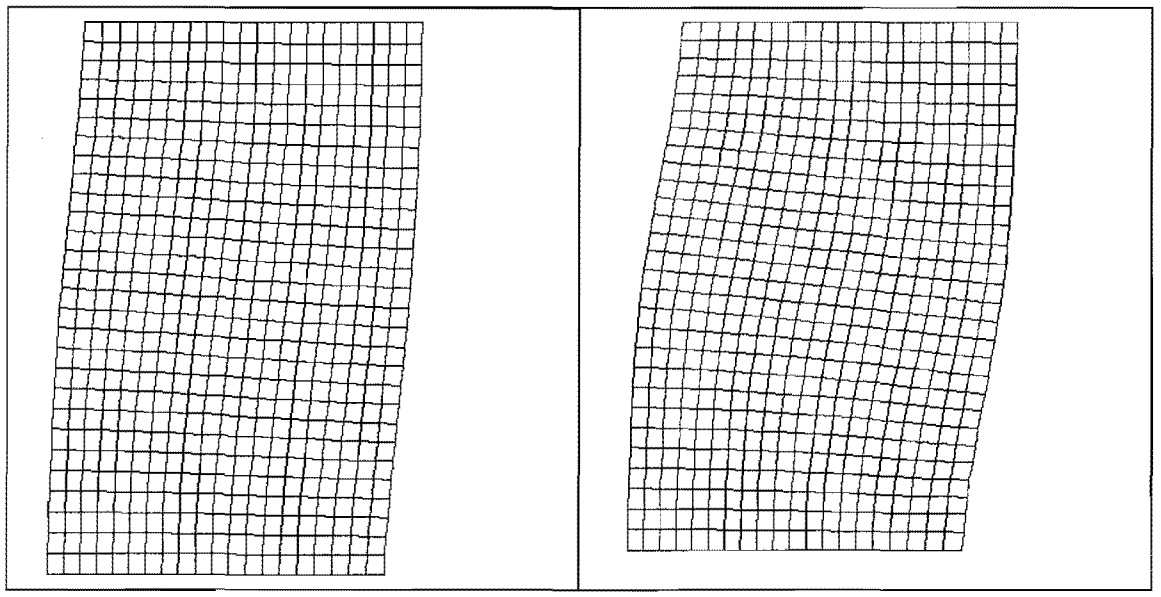

(a) (b)

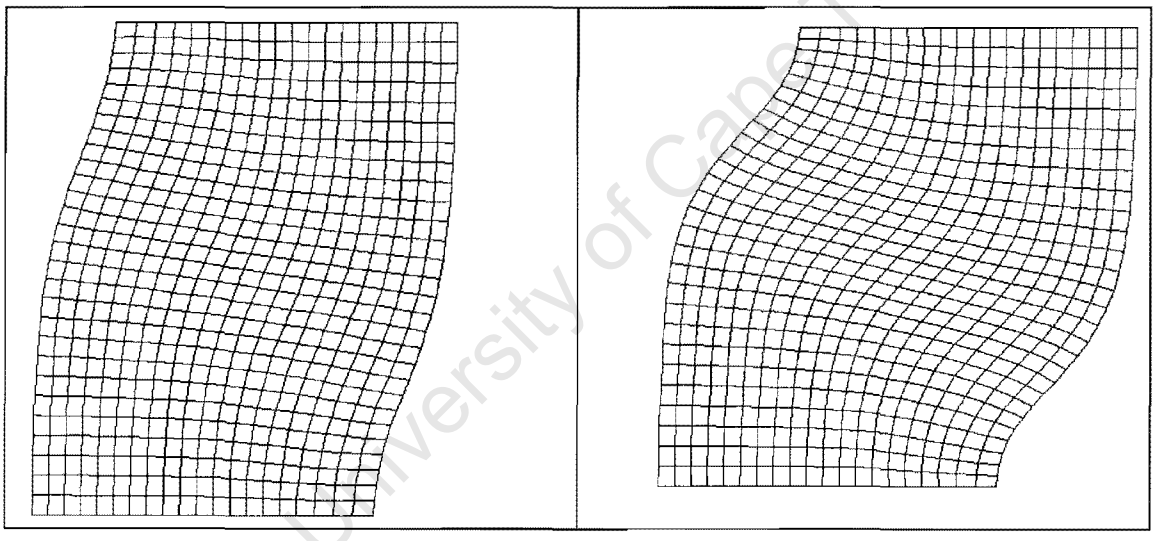

(c) (d)

Figure 5.12 Deformed finite element meshes of Al-Cu crystal for the extremal surface model. (a) ε_{22}=0.083, (b) ε_{22}=0.108, (c) ε_{22}=0.156, (d) ε_{22}=0.26.

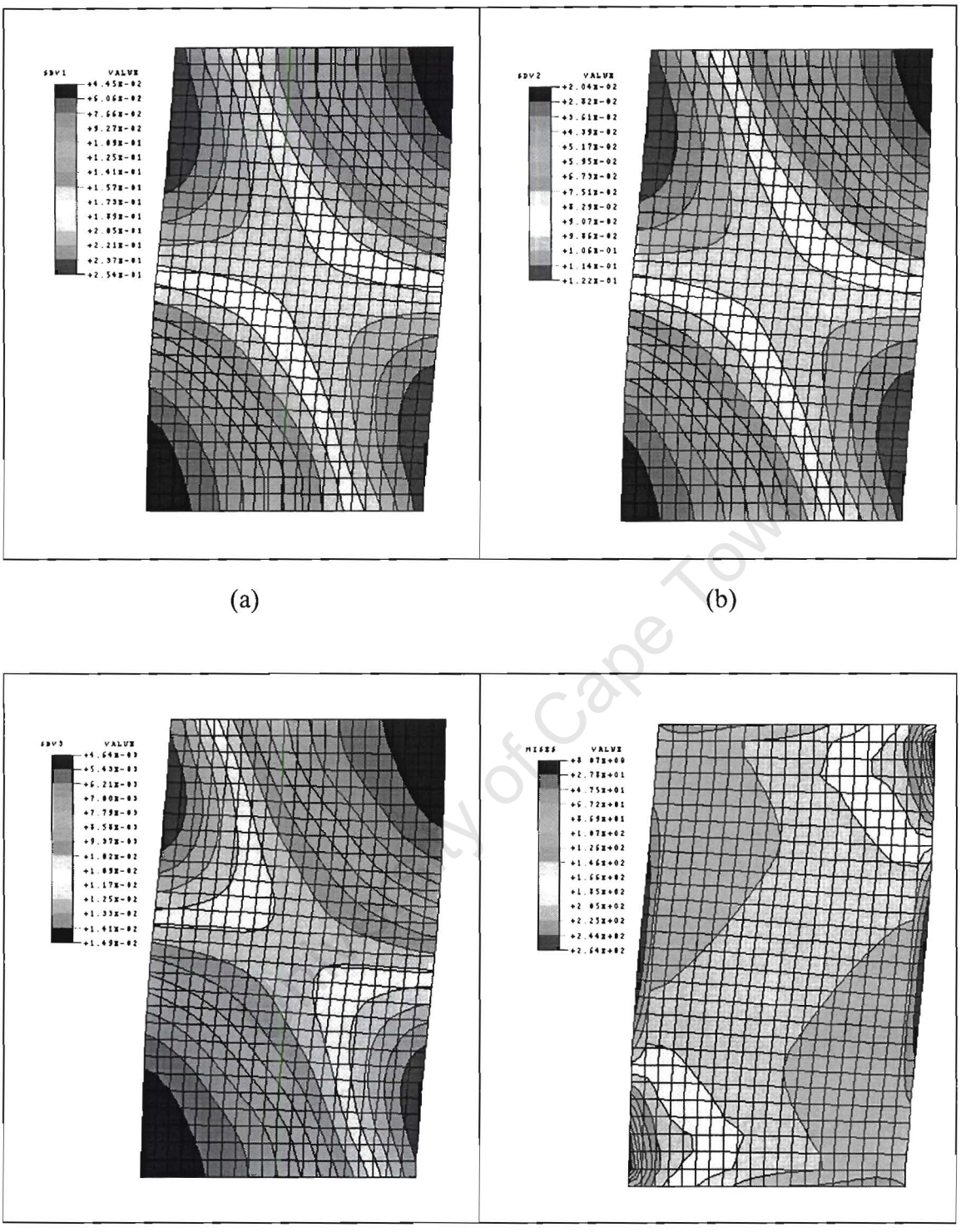

Figure 5.13 (a) Contours of accumulated slip; (b) contours of equivalent strain; (c) contours of nett fraction; (d) contours of the von Mises stress of the strain =0.083 of an Al-Cu (fcc) deformed crystal shown in Fig.(5.12(a)) for the extremal surface model.

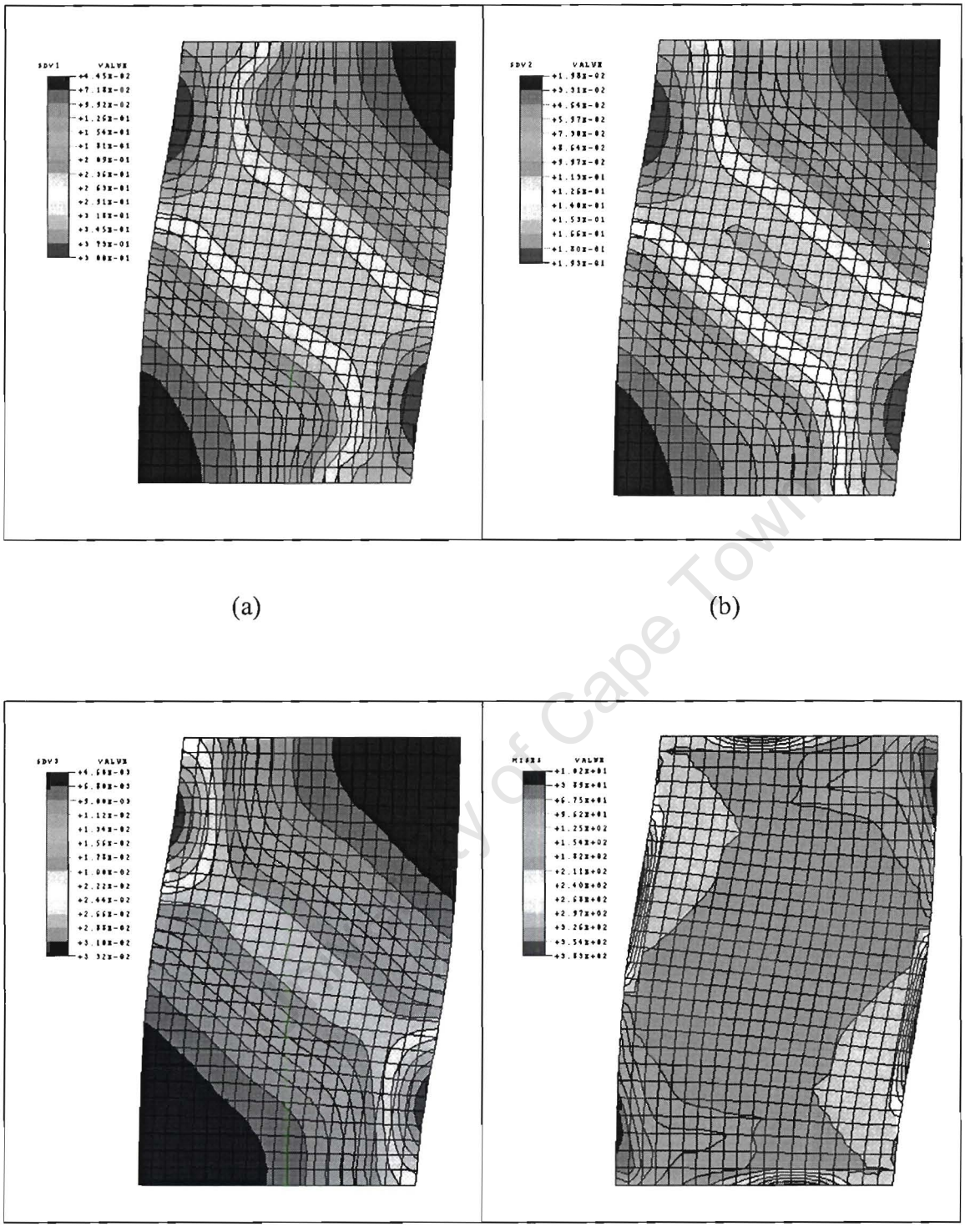

Figure 5.14 (a) contours of accumulated slip; (b) contours of equivalent strain; (c) contours of nett fraction; (d) contours of the von Mises stress for the strain ε_{22} =0.108 of an Al-Cu (fcc) deformed crystal shown in Fig.(5.12(b)) for the extremal surface model.

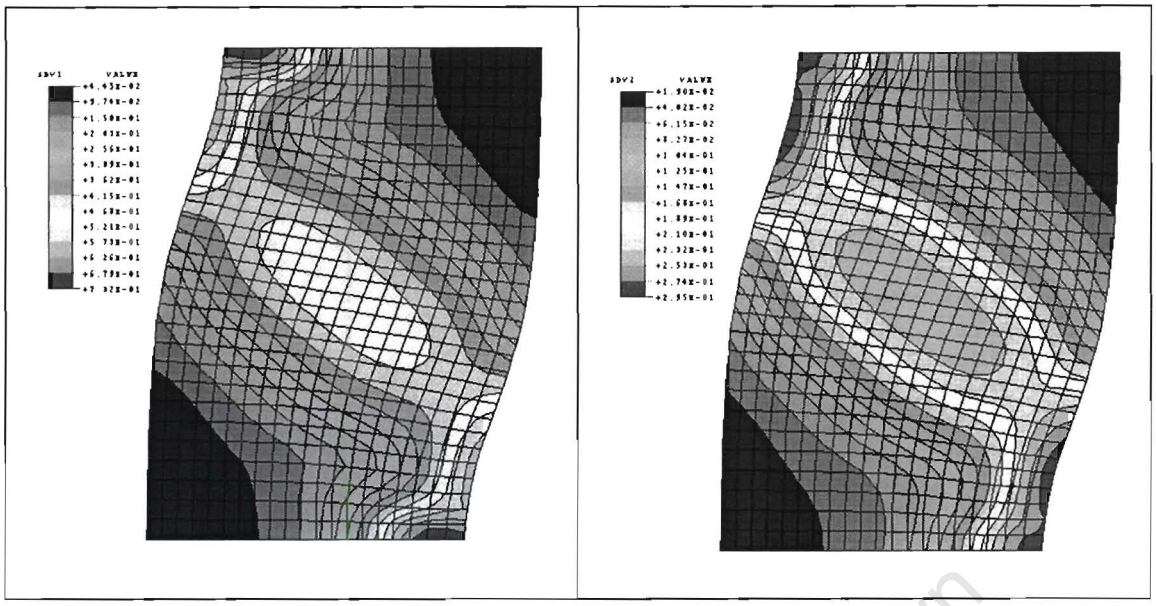

(a) (b)

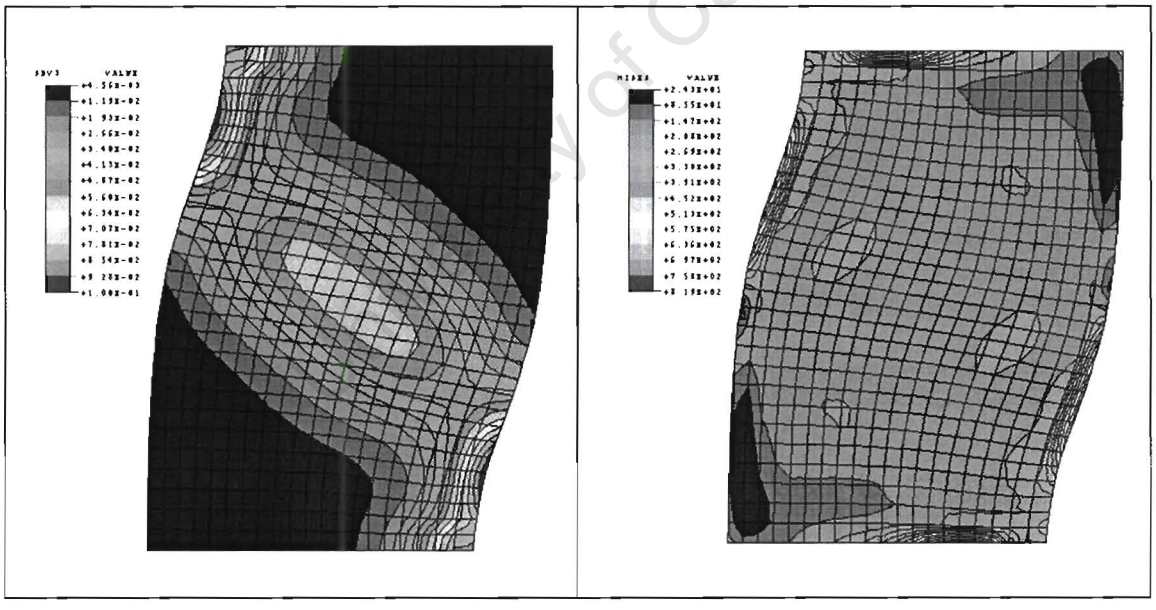

(c) (d)

Figure 5.15 (a) contours of accumulated slip; (b) contours of equivalent strain; (c) contours of nett fraction; (d) contours of the von Mises stress for the strain value ε_{22} =0.156 for the Al-Cu (fcc) deformed crystal shown in Fig.(5.12(c)) for the extremal surface model.

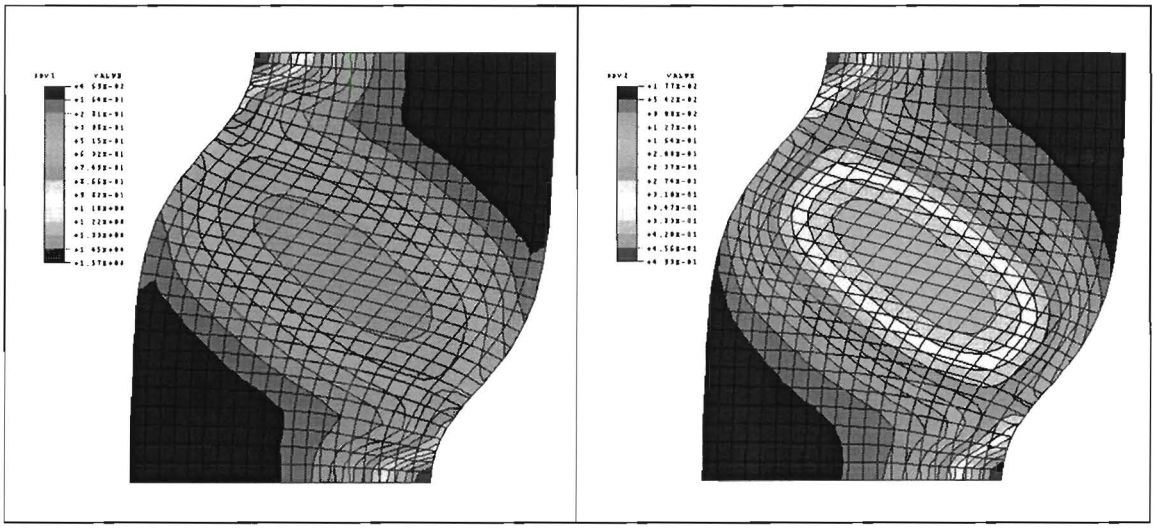

(a) (b)

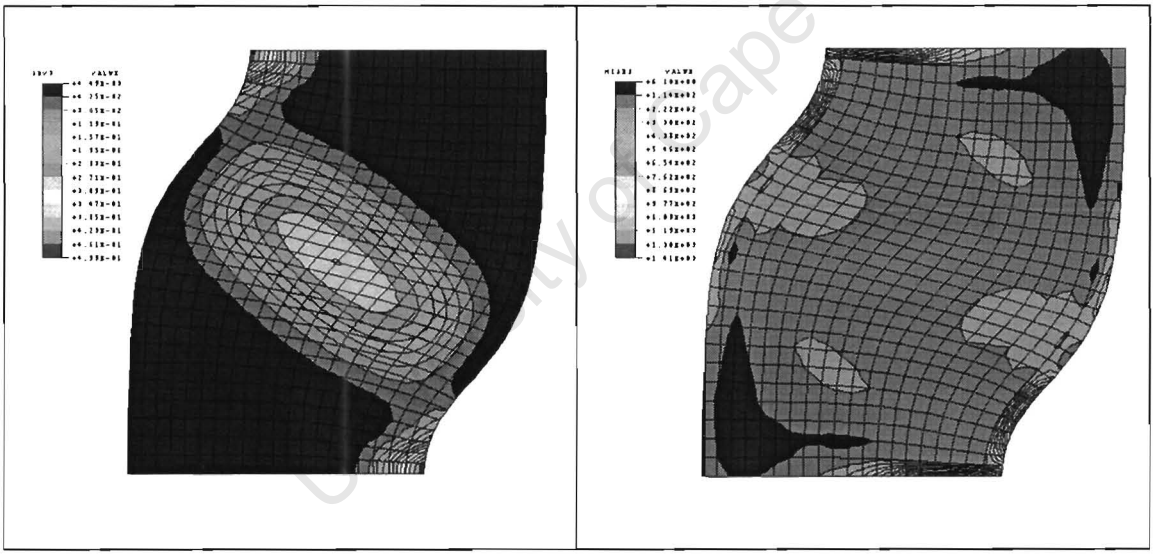

(c) (d)

Figure 5.16 (a) contours of accumulated slip; (b) contours of equivalent strain; (c) contours of net fraction; (d) contours of the von Mises stress for the strain value $\varepsilon_{22} = 0.26$ of an Al-Cu (fcc) deformed crystal shown in Fig.(5.12(d)) for the extremal surface model.

5.3 Channel die compression of a copper single crystal.

A copper single-crystal deformation in a plane-strain compression test is simulated both for rate dependent and rate independent constitutive models of a solid. A crystal is compressed between a channel die and a rectangular punch that is schematically depicted in Fig.(5.18).

CHANNEL DIE BENCHMARK:

The numerical analysis is conducted by using the finite element program ABAQUS with constitutive relations incorporated into a user subroutine. The deformation is modelled by considering a small part of a crystal as a representative unit volume. Actual dimensions of a region are irrelevant to this model, since constitutive relations do not include a size scale. The initial height and width of a model region are $L_o = 1.5\ W_o$ and $S_o = W_o$, S_o is the out-of plane dimension.

Compression is along the y direction. The material extends in the x direction and z is the out of plane direction.

The crystal is represented by five hundred and seventy square, two-dimensional, plane-strain, four-nodded elements. The finite element mesh consists of 30 quadrilaterals in the y-direction and 19 in the x-direction. Fig.(5.20(a)) shows the initial mesh geometry of the crystallite body. The boundary conditions are the following:

$U_y = 0$ along $y = 0$

$U_y = -.001 L_o$ along $y = L_o$

$U_x = 0$ along $x = 0$

$U_x =$ constant along $x = W_o$

All surfaces are constrained to remain planar. The boundary conditions are shown in Fig.(5.18). The elastic constants in Table 5.7 are taken to fit the elastic anisotropy of a copper single crystal [10], and determine a moderately rate-sensitive crystal with m = 0.002.

Table 5.7 Elastic constants used for the simulation with a copper single crystal.

C_{11}=842.0 τ_o, MPa	C_{12}= 607.0 τ_o, MPa	C_{44}=377.0 τ_o, MPa

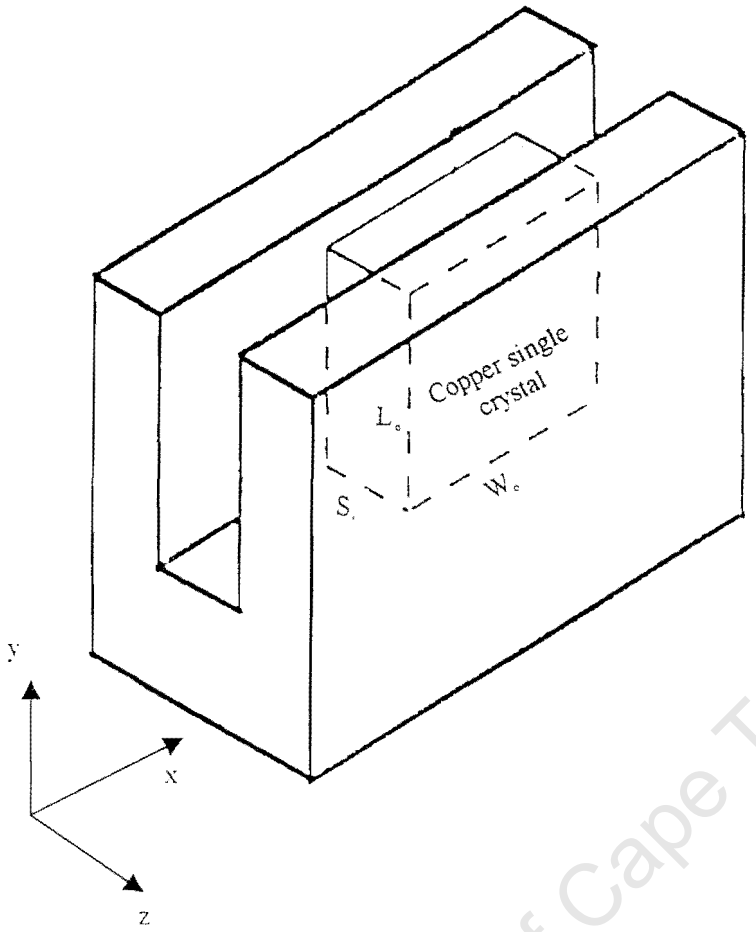

Figure 5.17 A copper single crystal in a channel die

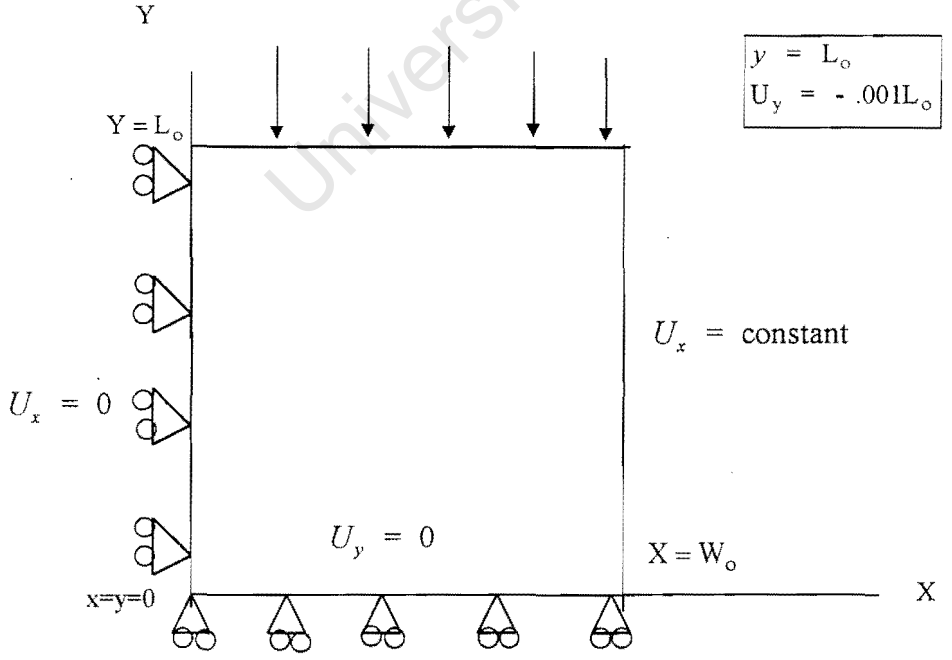

Figure 5.18 Boundary conditions applied to the copper crystal deformed in a channel die.

Results for simulations with a copper single crystal for the rate dependent material

Twelve slip directions, $\mathbf{m}^{\alpha}$, and twelve normals to slip planes, $\mathbf{n}^{\alpha}$, are idealized by two slip systems shown in Fig.(5.19). Finite element computations were carried out using the single crystal model depicted in Fig.(5.17), with the boundary conditions shown in Fig.(5.18). A value of the reference strain rate $\dot{a}^{\alpha}$ in Eq.(3.7) is given by $\dot{a}^{\alpha} = \dot{a}_o$, that is a constant for all slip systems α. The prescribed displacement rate is $\dot{U} = \dot{a}_o L_o$.

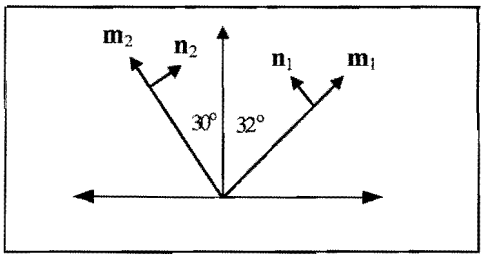

Figure 5.19 The initial lattice orientation for copper single crystal

The hardening law for the compression test of a copper single crystal is defined by

$$\dot{\gamma}^{\alpha} = \dot{a}\ \mathrm{sign}(\tau^{\alpha}) \left| \frac{\tau^{\alpha}}{q(\gamma)} \right|^{\frac{1}{m}},$$

$$g^{\alpha}(\gamma) = \tau_o + \frac{h_o}{11.125}\tanh(11.125\gamma), \quad h(\gamma) = h_o \mathrm{sech}^2(11.125\gamma).$$

The material parameters for the copper single crystal simulation are tabulated in Table 5.8. The value of strain-rate sensitivity exponent used in the analysis, m=0.002, was selected to provide a slightly rate dependent behaviour, and is taken to be within the range of material-rate sensitivities determined experimentally.

Table 5.8 Material parameters for the copper single crystal simulation for the rate dependent constitutive material model.

$\dot{a}_o$=0.001/s	m=0.002	$h_o = 8.9\ \tau_o$

Fig.(5.20) shows a deformed finite element mesh for various values of strains. The compressive logarithmic strain is $\varepsilon_{22} = -\ln(\frac{L}{L_o})$, where L and L_o are the current and the initial height of the finite element mesh along the y-direction, respectively. The deformation appears to be fairly uniform for ε_{22} =0.164. The deformation has become noticeably more non-uniform for ε_{22} =0.255. For ε_{22} larger than 0.255, it is

evident that new shearing modes have already formed a shear band from the north-west to south-east side of the specimen. This shear band is inclined at an angle approximately equal to 40° to the horizontal direction. The new shear band continuously intensifies for $\varepsilon_{22} = 0.58$.

Contours of the accumulated shear slip in Figs.(5.21(a)), (5.22(a)), and (5.23(a)) show the corresponding strain levels depicted in Figs.(5.20(b)), .(5.20(c)), and .(5.20(d)). Figs.(5.21(b)), (5.22(b)), and (5.23(b)) show equivalent strains. Figs.(5.22(a)) and .(5.22(b)) show that the deformation is quite non-uniform for the highest amount of slip activity occurred along the localized zone from the north-east to south-west, but strains do not exceed the applied uniform strain of 0.164. Figs.(5.23(a)) and (5.23(b)) show the formation of a new shear band which appears from the north-east to south-west zone of the specimen. Figs.(5.23(a)) and (5.23(b)) illustrate the shear band after intensification when the accumulated slip rate reaches a maximum value inside the shear band and the equivalent shear strain reaches a value of 1.26. This value is significantly greater than the applied uniform strain.

Figs.(5.21(c)), (5.22(c)), and (5.23(c)) show the rotation of the lattice accompanying the deformation. In Fig.(5.23(c)) it can be seen that a lattice inside the shear band rotates in the positive direction to align with the shear band direction.

It is important to note that results illustrated in Figs.(5.20)-(5.23) are for a moderately rate sensitive crystal with m = 0.002. Similar calculations, discussed in Section 5.2, show that the shear localization becomes more pronounced when m=0.005. However, the rate sensitivity is still high enough to split the crystal into active and passive regions.

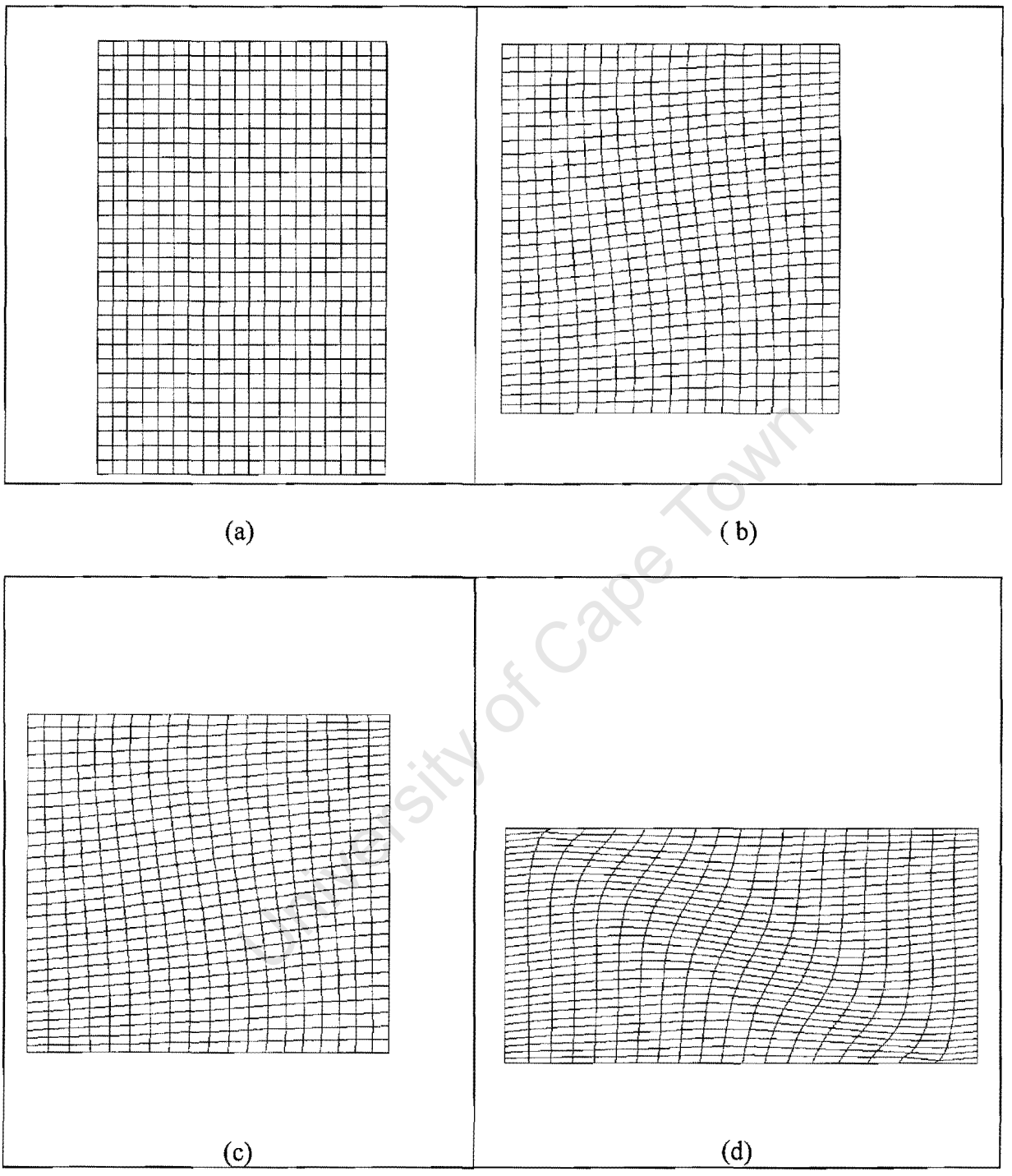

Figure 5.20 Deformed finite element meshes for a copper single crystal for the rate dependent model. (a) ε_{22}=0.0, (b) ε_{22}=0.164, (c) ε_{22}=0.255, (d) ε_{22}=0.58.

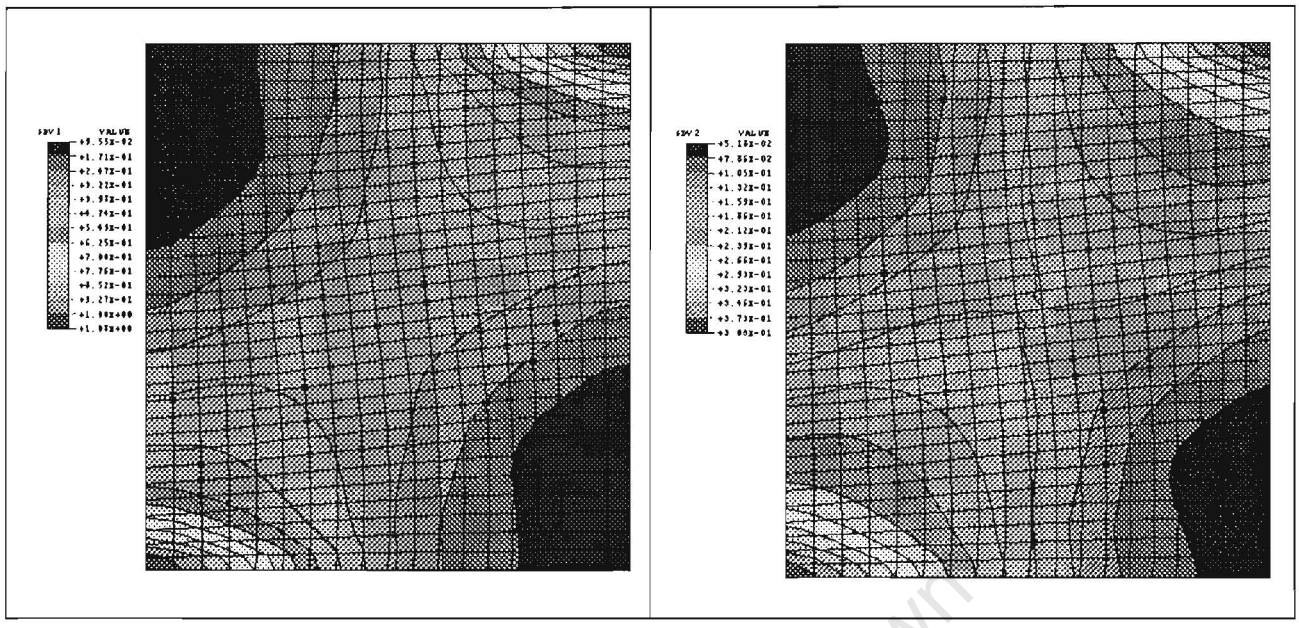

(a) (b)

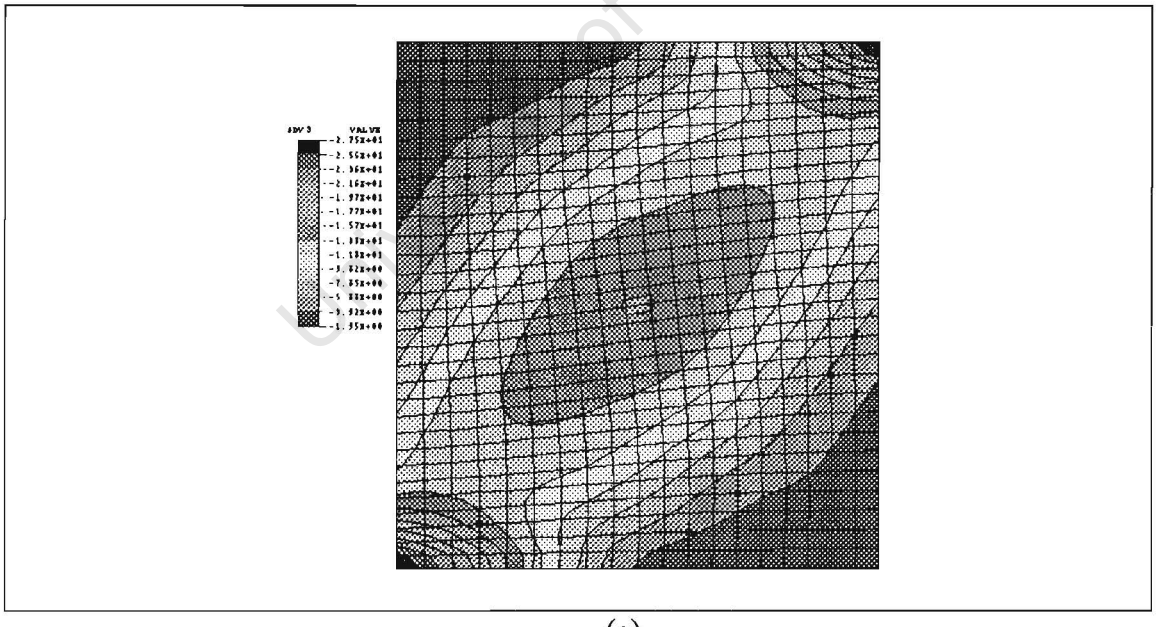

(c)

Figure 5.21 (a) Contours of accumulated slip; (b) contours of equivalent strain; (c) contours of lattice rotations for the strain $\varepsilon_{22} = 0.164$ for a deformed copper crystal shown in Fig.(5.20(b)) for the rate dependent model.

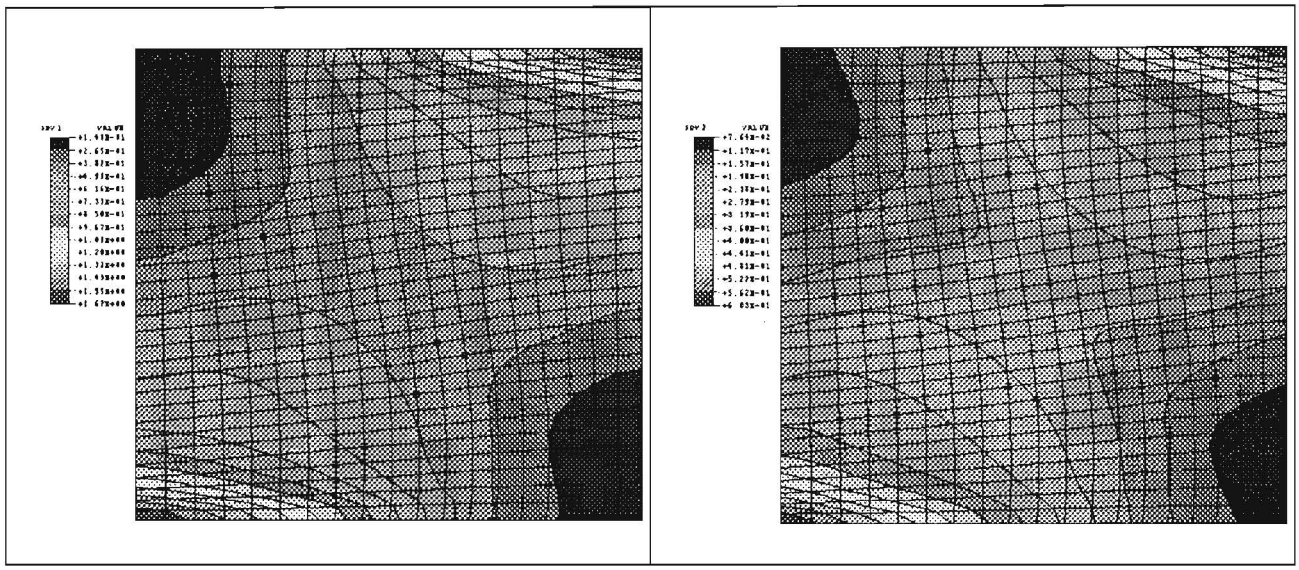

(a) (b)

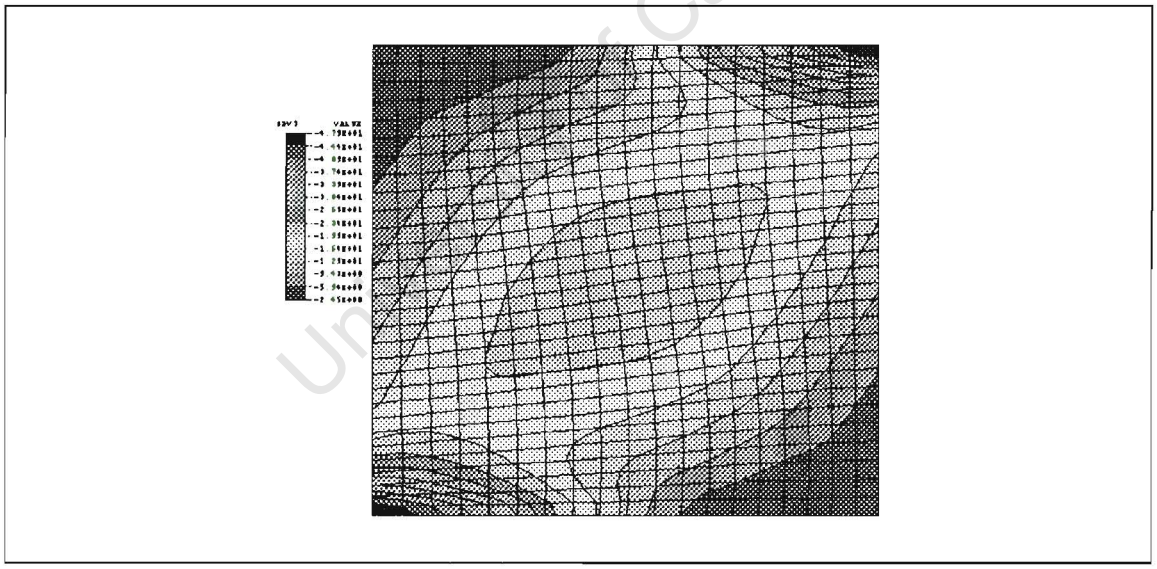

(c)

Figure 5.22 (a) Contours of accumulated slip; (b) contours of equivalent strain; (c) contours of lattice rotations for the strain $\varepsilon_{22} = 0.255$ for a deformed copper crystal shown in Fig.(5.20(c)) for the rate dependent model.

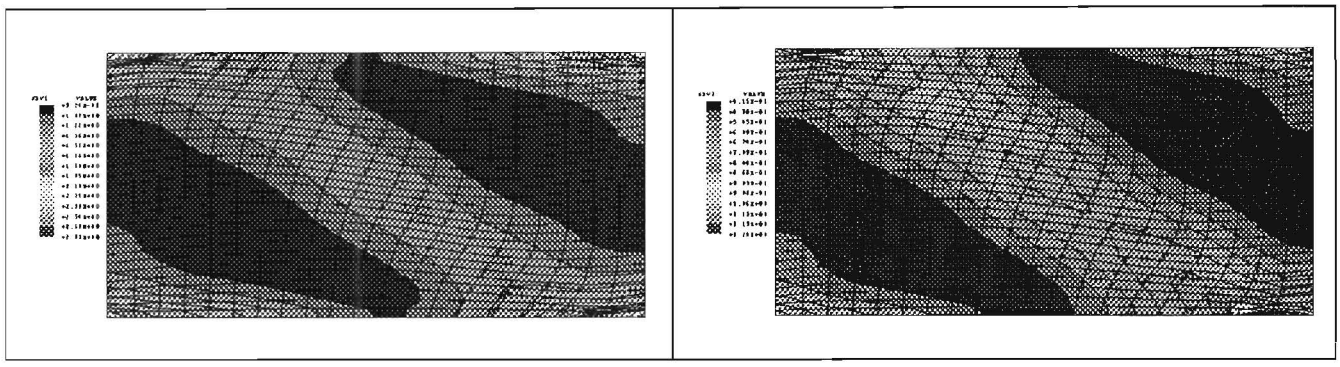

(a) (b)

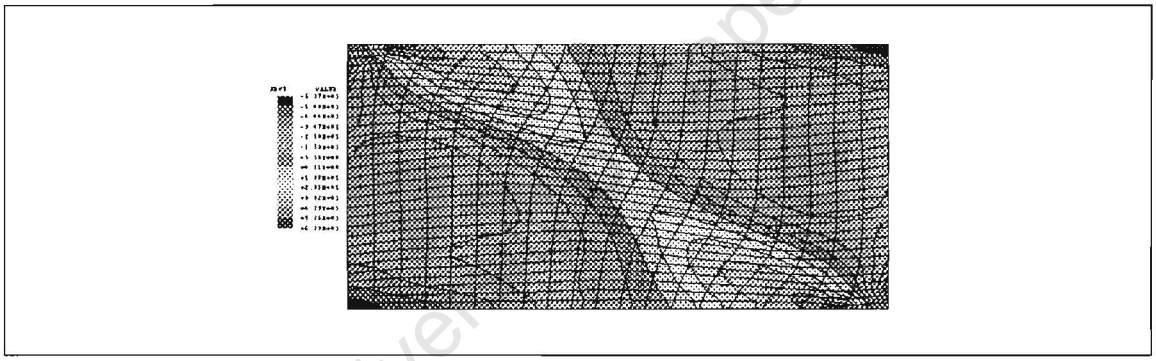

(c)

Figure 5.23 (a) Contours of accumulated slip; (b) contours of equivalent strain; (c) contours of lattice rotations for strain $\varepsilon_{22} = 0.58$ for a deformed copper crystal shown in Fig.(5.20(d)) for the rate dependent model.

Results of simulation for a copper single crystal for the extremal surface concept.

The reference configuration of the two dimensional strain compression crystal considered here is the same as in the copper crystal simulation for the rate dependent material. The net fraction formula is the same as the one used in the previous example of Section 5.2, with A=0.9, B=6.5, C=11, and $\beta = 0.5°$.

The single crystal compression simulation for the extremal surface concept is based on the hardening law used in Section 5.2 for the Al-Cu crystal simulation. The elastic constants are tabulated in Table 5.7.

Deformed finite element meshes for the plain strain compression simulation are shown in Figs.(5.25(a))-(5.25(c)) for various values of strain.

Figs.(5.25(a)), (5.25(b)), (5.26(a)), (5.26(b)), (5.27(a)), and (5.27(b)) show the corresponding strain levels depicted in Fig.(5.24). Unlike the rate dependent simulation of this problem, Fig.(5.25(a)) and (5.25(b)) show that the deformation is becoming non-uniform. When ε_{22} = 0.164 the shear localized in a zone from north-east to the south-west, with the highest slip rate in localized zone. Fig.(5.26) corresponding to strain level depicted in Fig.(5.24(b)) shows the start of localization in the zone from the north-west to the south-east. Fig.(5.27), that corresponds to strain level depicted in Fig.(5.24(c)) shows the propagation of shear mode in a form of a shear band across the north-west to the south-east of the specimen inclined at an angle approximately equal to 36° to the horizontal direction. This angle is significantly smaller than the inclination of the shear band in the rate dependent simulation. Strain inside the shear band reached a value of 1.17, which is significantly higher than the applied strain. The net fraction internal variable is greater than zero and less than one, and reaches a maximum value of 0.902 inside the shear band at the strain level of 0.58. Shear band in Fig.(5.24(c)) is not as sharp as in Fig.(5.20(d)) for the rate dependent simulation.

Results of simulation for a copper single crystal for the extremal surface concept.

The reference configuration of the two dimensional strain compression crystal considered here is the same as in the copper crystal simulation for the rate dependent material. The net fraction formula is the same as the one used in the previous example of Section 5.2, with A=0.9, B=6.5, C=11, and $\beta = 0.5°$.

The single crystal compression simulation for the extremal surface concept is based on the hardening law used in Section 5.2 for the Al-Cu crystal simulation. The elastic constants are tabulated in Table 5.7.

Deformed finite element meshes for the plain strain compression simulation are shown in Figs.(5.25(a))-(5.25(c)) for various values of strain.

Figs.(5.25(a)), (5.25(b)), (5.26(a)), (5.26(b)), (5.27(a)), and (5.27(b)) show the corresponding strain levels depicted in Fig.(5.24). Unlike the rate dependent simulation of this problem, Fig.(5.25(a)) and (5.25(b)) show that the deformation is becoming non-uniform. When ε_{22} = 0.164 the shear localized in a zone from north-east to the south-west, with the highest slip rate in localized zone. Fig.(5.26) corresponding to strain level depicted in Fig.(5.24(b)) shows the start of localization in the zone from the north-west to the south-east. Fig.(5.27), that corresponds to strain level depicted in Fig.(5.24(c)) shows the propagation of shear mode in a form of a shear band across the north-west to the south-east of the specimen inclined at an angle approximately equal to 36° to the horizontal direction. This angle is significantly smaller than the inclination of the shear band in the rate dependent simulation. Strain inside the shear band reached a value of 1.17, which is significantly higher than the applied strain. The net fraction internal variable is greater than zero and less than one, and reaches a maximum value of 0.902 inside the shear band at the strain level of 0.58. Shear band in Fig.(5.24(c)) is not as sharp as in Fig.(5.20(d)) for the rate dependent simulation.

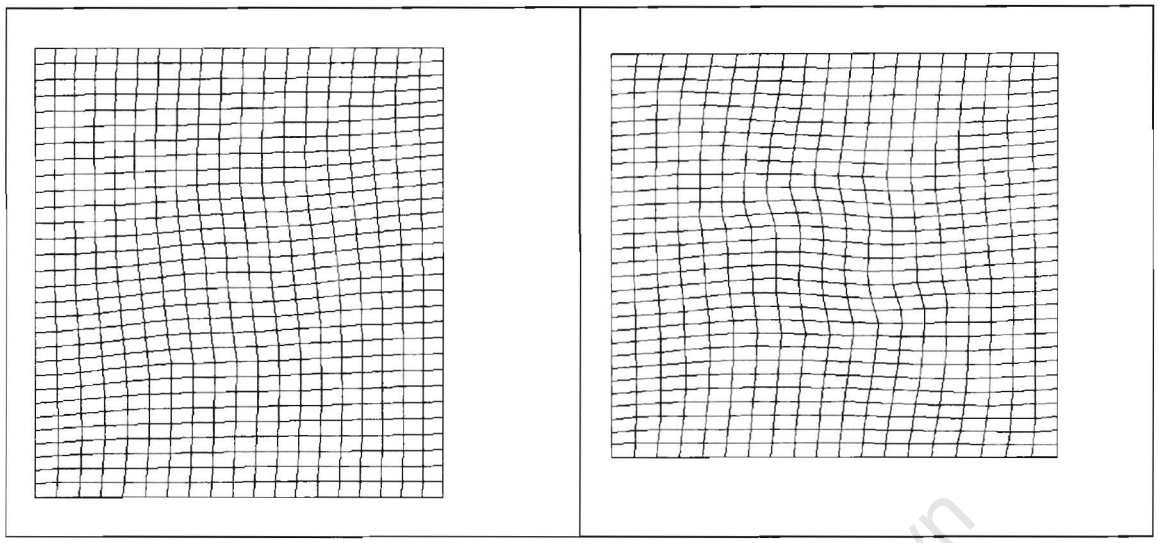

(a) (b)

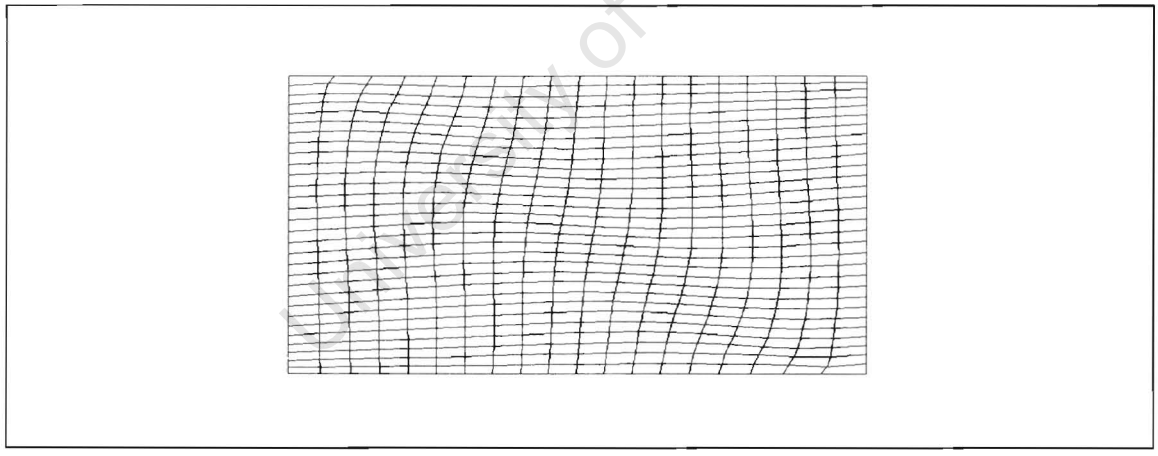

(c)

Figure 5.24 Deformed finite element meshes for a copper single crystal for the extremal surface model, for various values of strain (a) ε_{22}=0.164, (b) ε_{22}=0.255, (c) ε_{22}=0.58.

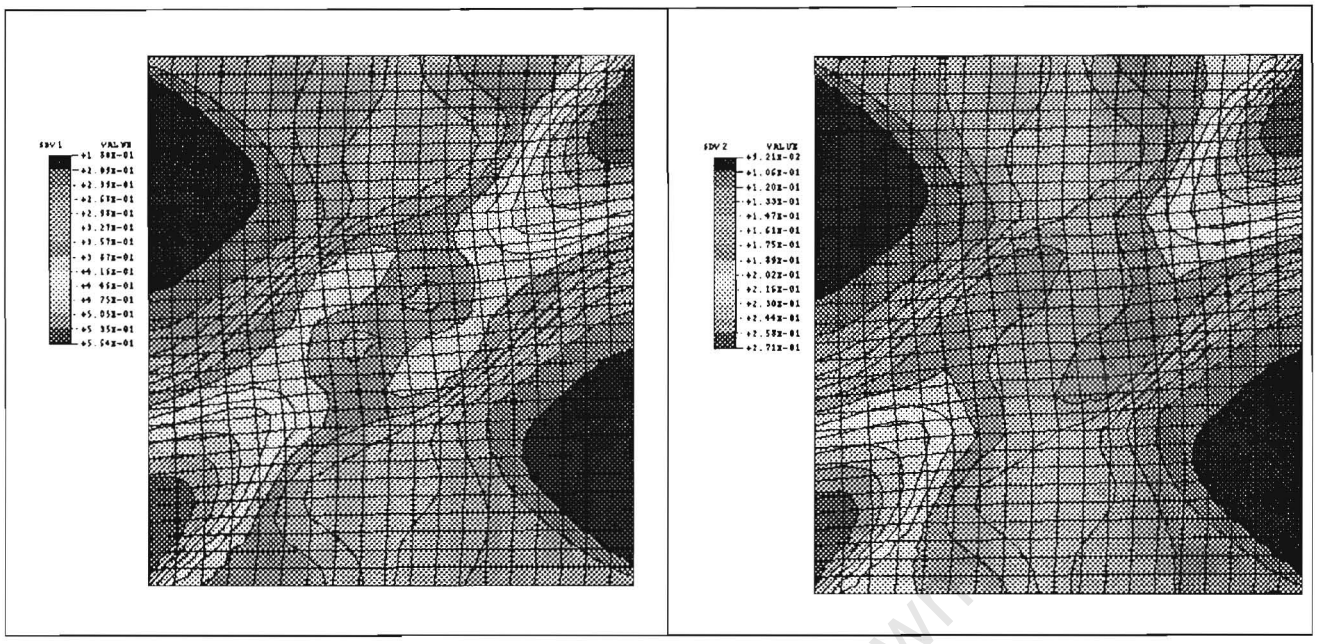

(a) (b)

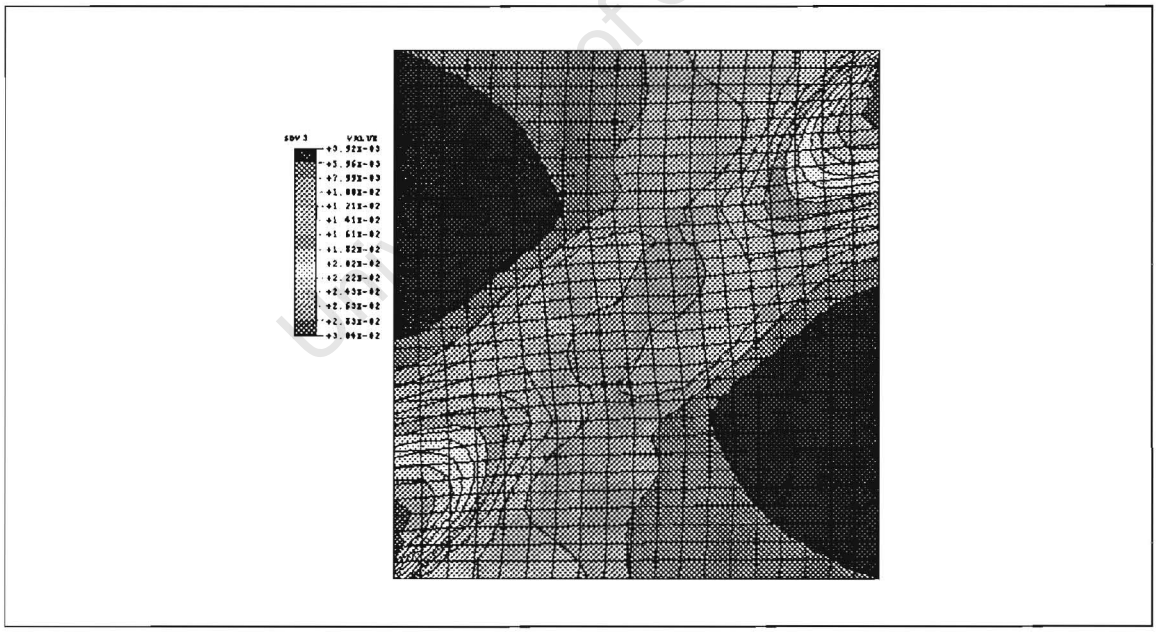

(c)

Figure 5.25 (a) contours of accumulated slip; (b) contours of equivalent strain; (c) contours of nett fraction for the strain ε_{22}=0.164 for a deformed copper crystal shown in Fig.(5.24(a)) for the rate independent model.

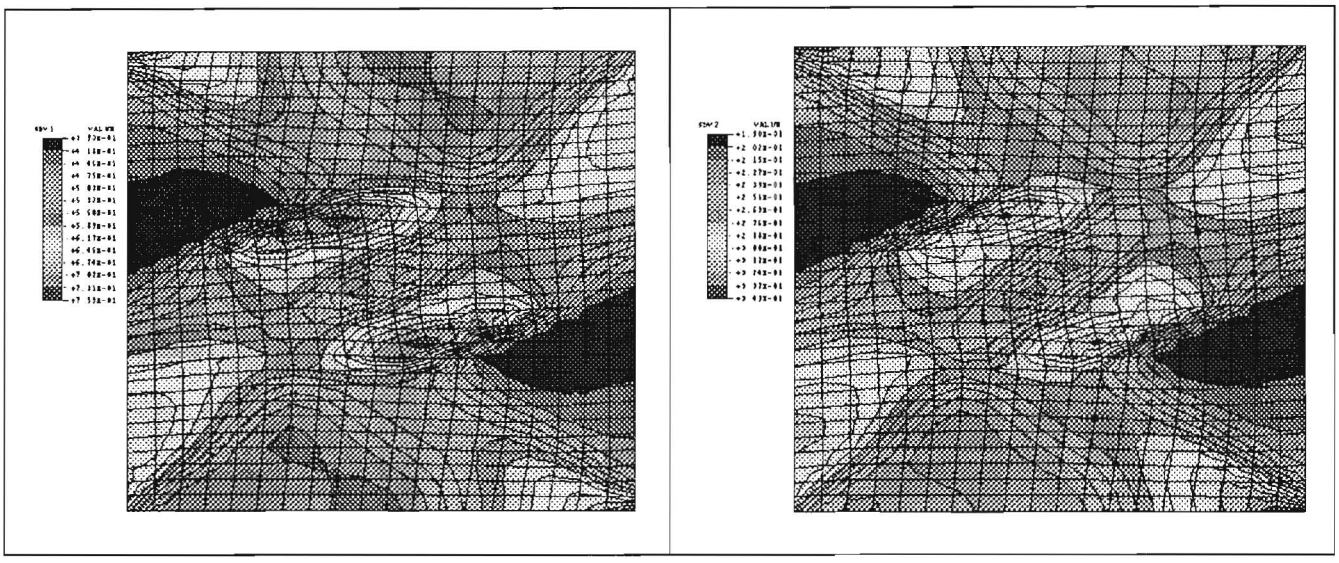

(a) (b)

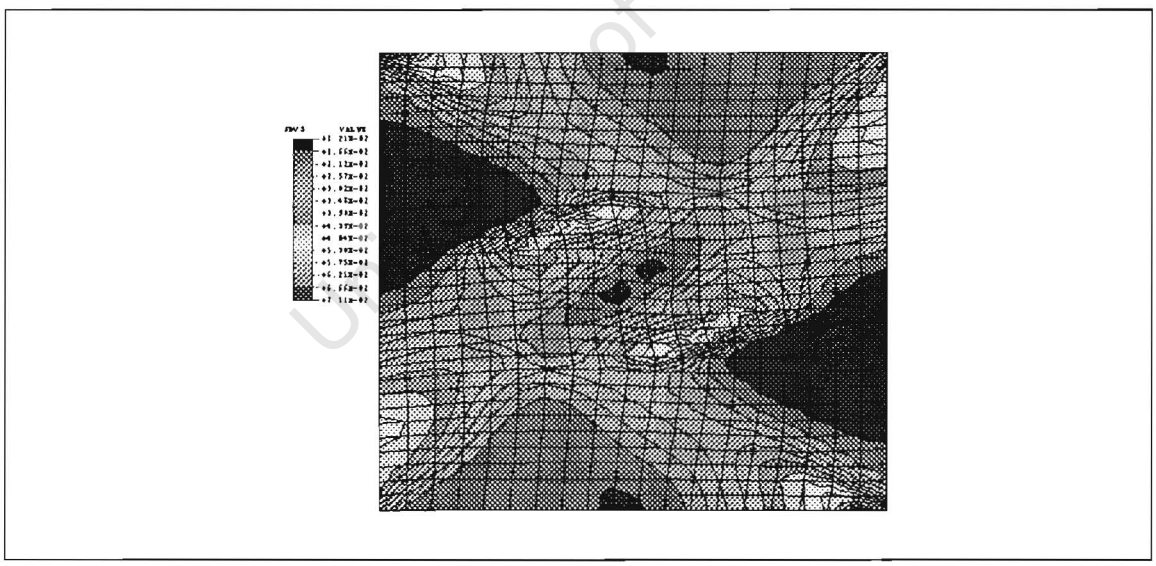

(c)

Figure 5.26 (a) contours of accumulated slip; (b) contours of equivalent strain; (c) contours of net fraction the strain ε_{22}=0.255 for a deformed copper crystal shown in Fig.(5.24(b)) for the rate independent model.

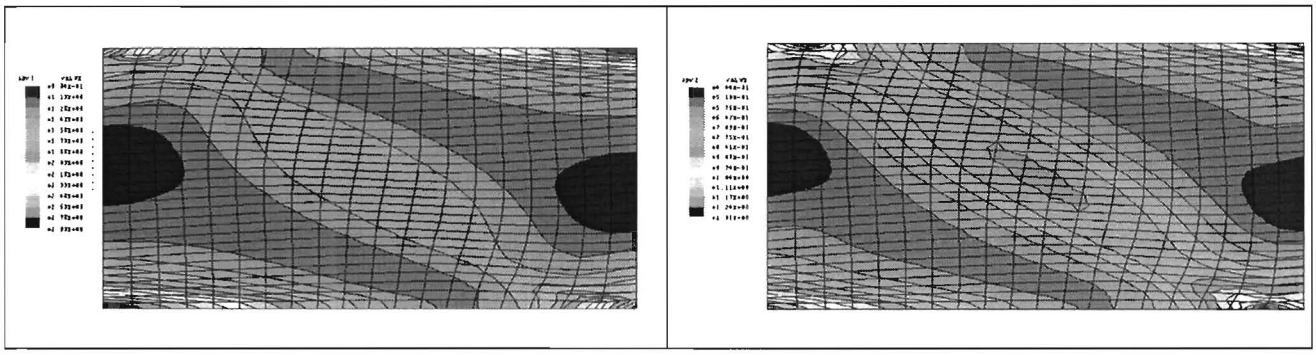

(a) (b)

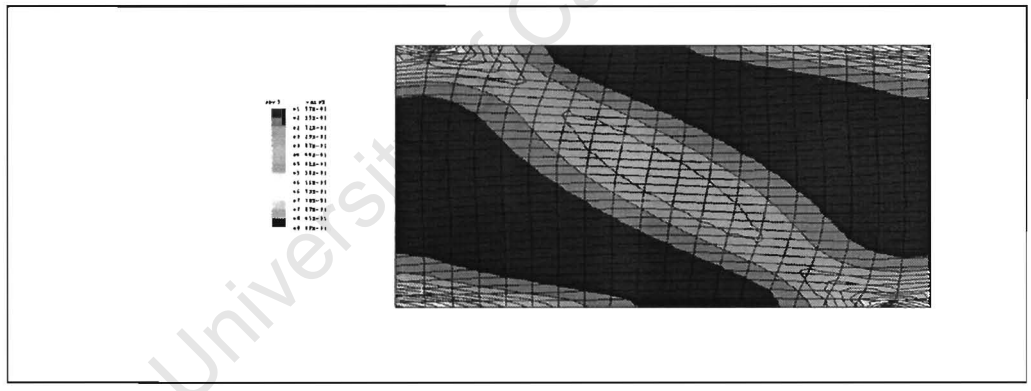

(c)

Figure 5.27 (a) Contours of accumulated slip; (b) contours of equivalent strain; (c) contours of nett fraction the strain $\varepsilon_{22} = 0.58$ for a deformed copper crystal shown in Fig.(5.24(c)) for the rate independent model.

CHAPTER SIX

CONCLUSIONS

The development of rate dependent constitutive relations for analyzing crystalline plasticity and texture evolution at large strains as presented in [5], [54], [74], [75], [76], makes possible the study of other phenomena, like shear localization in a form of shear bands. These studies together with results obtained in chapter five showed the importance of shear bands at large plastic deformation of metals. They also showed the importance of developing constitutive equations that consider the role of shear bands in a large plastic deformation process of crystallite materials, and help to develop a clear and accurate understanding of plasticity.

Procedures applicable for modeling of shear localization in single crystals are developed for various materials such as the rate dependent material model proposed by Peirce *et al.* [75], and a model of material with the concept of extremal surface recently developed by Pecherski [72]. Results are obtained for various crystalline geometries using the finite element software ABAQUS incorporating internal variable algorithms for the integration of the constitutive relations through the user material subroutine "UMAT". Results obtained for these two material models for a benchmark with a plain strain compression for (fcc) and (bcc) single crystals are compared and analyzed.

Localization of plastic flow into macroscopic shear bands has long been observed under general states of stress and strain. Further, after the first appearance of shear bands, most materials can withstand large amounts of plane strain compression without fracture. The localization of deformation into shear bands is an inherent and natural outcome of a plastic deformation process with large deformations. Results for both models show that bands of localized plastic deformation are formed at realistic strain levels and occur at angles that are in agreement with experimental and computational results obtained by Anand, Becker, and Peirce *et al.* [5], [13], [14], [75], [76].

The finite element calculations with the forward gradient scheme developed by Peirce *et al.* [75] illustrate the importance of kinematics in the development of non-uniform and localized deformation in a single crystal. The formation of a shear band invariably occurs along planes rotated, relative to the dominant slip system, away from the compression direction. In the case of the initial slip system with angle α_o

equal to thirty degrees that is used for the rate dependent modeling of (fcc) crystals, it was found that after accumulated large strains, shear-bands are formed in a sharp way, and the localized zone is thin. The kinematics of shear-band involves a significant lattice rotation inside bands which increases the resolved shear stress on the specific slip system. It means that a rotation causes "a geometric softening" and thus promotes intensive straining locally. A lattice rotation inside a shear-band is in the positive direction, so the slip system can align with shear-band direction. The case of the initial slip system angle α_0 equal to sixty degrees represents a different geometry suitable for the rate dependent model of (bcc) crystals. In this case shear bands have difficulty in forming and their formation starts at higher strains compared to the (fcc) crystal and the lattice rotation is in the negative direction. A localized zone in this case is significantly wider than in the case of the (fcc) crystal simulation. It is noticeable that in both models, bands of the localized plastic deformation are formed at realistic strain levels. Once a shear band initiates, it appears to be the major strain bearing process and it divides a crystal into an active and a passive region. Thus, with increasing strain more localization develops in initially localized areas. The lattice rotations in both cases compares favorably with solutions by Lemond *et al.* [55], Peirce *et al.* [75] and Harren *et al.* [36].

It is important to note that in the rate dependent calculations of the (fcc) and (bcc) single crystals with strain rate sensitivity parameter m = 0.005, the shear localization is more pronounced in comparison to calculations for a moderately rate sensitive copper single crystal with m=0.002. This is in a very close agreement with results obtained by Peirce *et al.* [75].

Results obtained for the plain strain compression benchmark for Al-Cu and copper single crystals, for the rate dependent constitutive relations, indicate that the initial orientation of a crystal influences both the onset of band formation and the orientation of bands. This agrees with experimental results obtained by Embury *et al.* [32] in their study of the nature of shear bands in Al-Cu single crystals.

It seems that, in spite of the complexity, the extremal surface concept of large plastic deformation can be applicable in modeling of large plastic deformations under highly constrained conditions, that occur in technological shaping processes and ductile failure. In the cases presented in this work, calculations proved to be effective. In the rate independent simulation of the Al-Cu single crystal, the non-uniform localization at started almost the same strain as in the case of rate dependent simulation of the Al-Cu and (bcc) crystals simulation. A shear localization in copper for the rate dependent model starts significantly earlier than a shear localization of the same crystal for the rate independent model. A width of shear localization zone for the simulation with the extremal surface is significantly wider than the one obtained for the rate dependent simulation. These shear bands are also not as sharp as in the rate dependent simulation. The angles of inclination of shear bands in both rate dependent and rate independent models agree with experimental results obtained by Peirce *et al.* [75]. Harren *et al.* [36]. Embury *et al.* [32], and Bronkhorst *et al.* [17][18].

Although computational results obtained for the rate dependent model are closer to the experimental results than those obtained with the extremal surface approach, the rate independent constitutive models are significantly less time consuming than the rate dependent ones. The extremal surface concept needs more experimental and more

equal to thirty degrees that is used for the rate dependent modeling of (fcc) crystals, it was found that after accumulated large strains, shear-bands are formed in a sharp way, and the localized zone is thin. The kinematics of shear-band involves a significant lattice rotation inside bands which increases the resolved shear stress on the specific slip system. It means that a rotation causes "a geometric softening" and thus promotes intensive straining locally. A lattice rotation inside a shear-band is in the positive direction, so the slip system can align with shear-band direction. The case of the initial slip system angle α_o equal to sixty degrees represents a different geometry suitable for the rate dependent model of (bcc) crystals. In this case shear bands have difficulty in forming and their formation starts at higher strains compared to the (fcc) crystal and the lattice rotation is in the negative direction. A localized zone in this case is significantly wider than in the case of the (fcc) crystal simulation. It is noticeable that in both models, bands of the localized plastic deformation are formed at realistic strain levels. Once a shear band initiates, it appears to be the major strain bearing process and it divides a crystal into an active and a passive region. Thus, with increasing strain more localization develops in initially localized areas. The lattice rotations in both cases compares favorably with solutions by Lemond *et al.* [55], Peirce *et al.* [75] and Harren *et al.* [36].

It is important to note that in the rate dependent calculations of the (fcc) and (bcc) single crystals with strain rate sensitivity parameter m = 0.005, the shear localization is more pronounced in comparison to calculations for a moderately rate sensitive copper single crystal with m=0.002. This is in a very close agreement with results obtained by Peirce *et al.* [75].

Results obtained for the plain strain compression benchmark for Al-Cu and copper single crystals, for the rate dependent constitutive relations, indicate that the initial orientation of a crystal influences both the onset of band formation and the orientation of bands. This agrees with experimental results obtained by Embury *et al.* [32] in their study of the nature of shear bands in Al-Cu single crystals.

It seems that, in spite of the complexity, the extremal surface concept of large plastic deformation can be applicable in modeling of large plastic deformations under highly constrained conditions, that occur in technological shaping processes and ductile failure. In the cases presented in this work, calculations proved to be effective. In the rate independent simulation of the Al-Cu single crystal, the non-uniform localization at started almost the same strain as in the case of rate dependent simulation of the Al-Cu and (bcc) crystals simulation. A shear localization in copper for the rate dependent model starts significantly earlier than a shear localization of the same crystal for the rate independent model. A width of shear localization zone for the simulation with the extremal surface is significantly wider than the one obtained for the rate dependent simulation. These shear bands are also not as sharp as in the rate dependent simulation. The angles of inclination of shear bands in both rate dependent and rate independent models agree with experimental results obtained by Peirce *et al.* [75], Harren *et al.* [36], Embury *et al.* [32], and Bronkhorst *et al.* [17][18].

Although computational results obtained for the rate dependent model are closer to the experimental results than those obtained with the extremal surface approach, the rate independent constitutive models are significantly less time consuming than the rate dependent ones. The extremal surface concept needs more experimental and more

cost efficient and theoretical studies to identify relevant internal variables. In the nett fraction evolution equation, the identification of parameters for specific materials plays an important role in the solution of industrial problems. In spite of not using the exact nett fraction evolution equations, results for the extremal surface concept show similarity with the rate dependent model. Comparison of these results with experimental tests still requires an evaluation of the effectiveness of the extremal surface concept.

Rate dependent and rate independent constitutive models facilitate a study of more complex problems. In particular, it is possible to include more complex single crystals and polycrystals, such as those based on the actual three-dimensional geometry of metals. It is also possible to include kinematic hardening in the extremal surface concept along with the isotropic hardening.

APPENDIX A

CRYSTALLITE SLIP SYSTEMS

This appendix contains examples and symbols used to denote crystallite slip systems.

We assumed the crystal has two slip systems symmetrically disposed about the tensile y-axis, and that **m** and **n** vectors represent the slip direction and the slip plane normals, respectively. Geometry dictates that

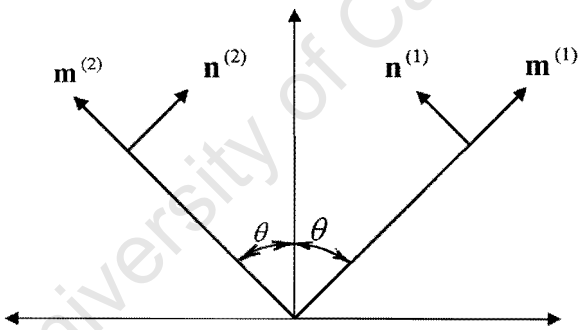

Figure A.1 Two slip directions $\mathbf{m}^i$ and slip plane normals $\mathbf{n}^i$ in the crystals idealized by two slip systems.

$m_1^{(1)} = \sin\theta$	$m_1^{(2)} = -\sin\theta$
$m_2^{(1)} = \cos\theta$	$m_2^{(2)} = \cos\theta$
$n_1^{(1)} = -\cos\theta$	$n_1^{(2)} = \cos\theta$
$n_2^{(1)} = \sin\theta$	$n_2^{(2)} = \sin\theta$

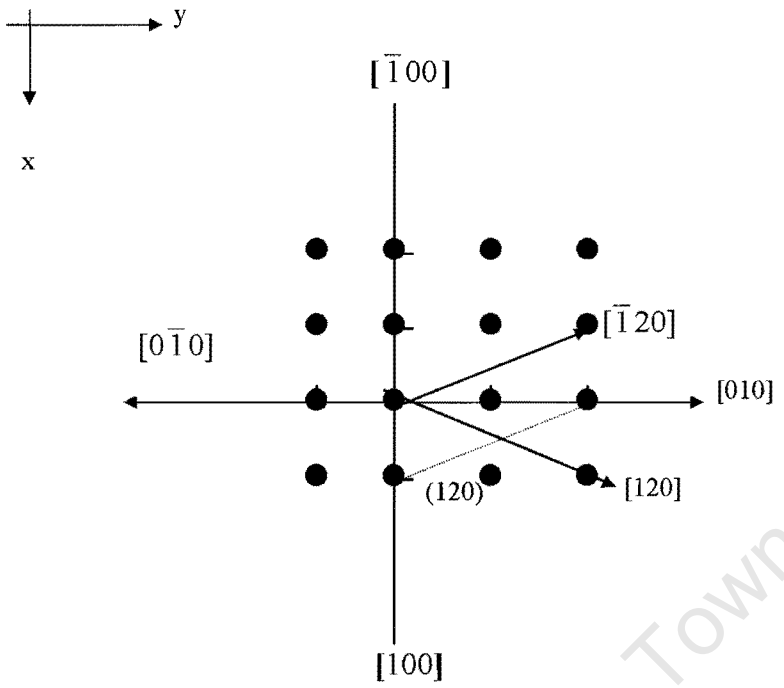

Figure A.2 Examples showing lattice directions in two-dimensional lattice.

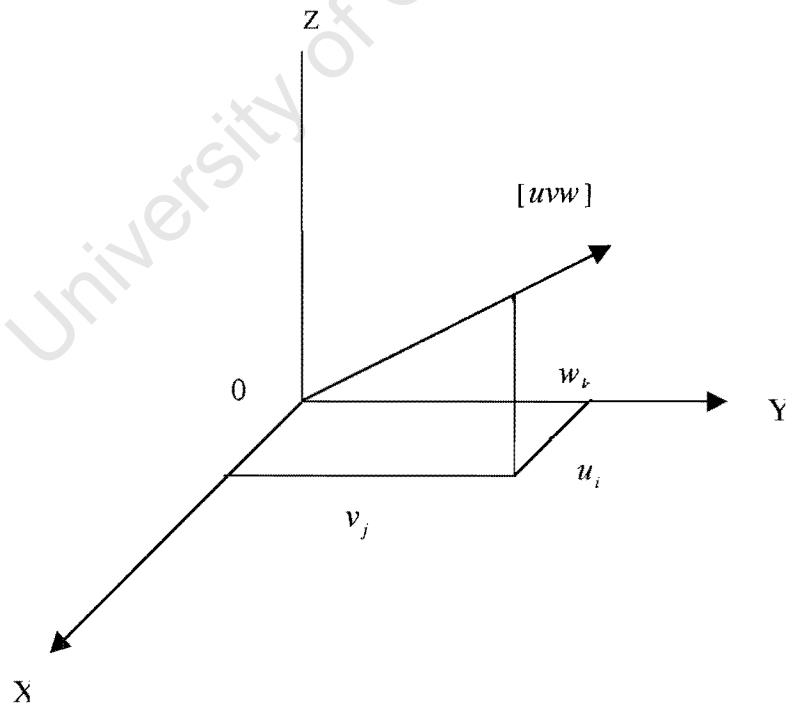

Figure A.3 The direction [*uvw*] in relation to its components along the crystallographic axis.

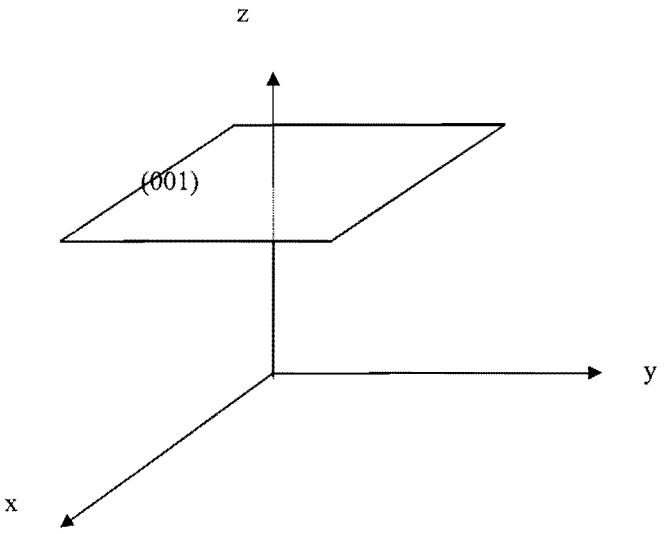

Figure A.4 Plane (001) intercepts z-axis at unity and x-and y-axes at infinity.

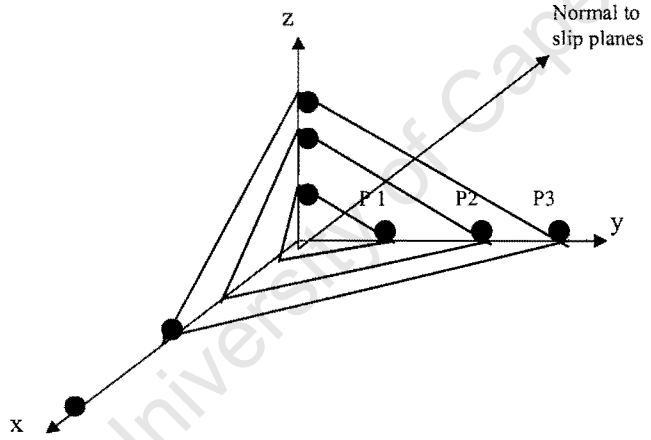

Figure A.5 Three-dimensional lattice and the (311) family of planes

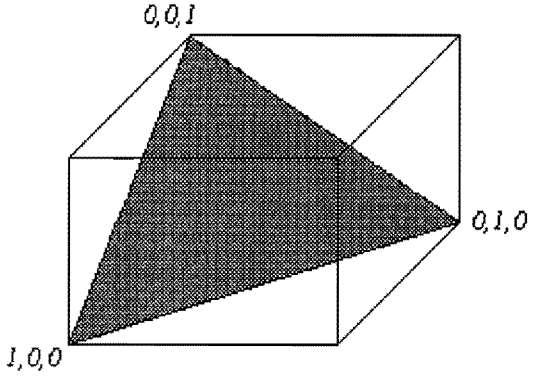

Figure A.6 Gliding of the (fcc) crystal on the crystallographic plane (111) and the <110> slip direction.

Table A.1 Example of twelve {111}<110> (fcc) slip systems in terms of the rotation angle θ.

slip system	directions
1- $n^1=(111)$ $m^1=[011]$	$(\sqrt{2}\cos\theta - \sin\theta\ ,\ \sqrt{2}\sin\theta + \cos\theta,\ 0)/\sqrt{3}$ $(\cos\theta + \sqrt{2}\sin\theta\ ,\ \sin\theta - \sqrt{2}\cos\theta\ ,-1)/2$
2- $n^2=(111)$ $m^2=[10\bar{1}]$	$(\sqrt{2}\cos\theta - \sin\theta\ ,\ \sqrt{2}\sin\theta + \cos\theta,\ 0)/\sqrt{3}$ $(\cos\theta + \sqrt{2}\sin\theta, \sin\theta - \sqrt{2}\cos\theta\ ,1)/2$
3- $n^3=(111)$ $m^3=[1\bar{1}0]$	$(\sqrt{2}\cos\theta - \sin\theta\ ,\ \sqrt{2}\sin\theta + \cos\theta,\ 0)/\sqrt{3}$ $(0,0,1)$
4- $n^4=(\bar{1}1\bar{1})$ $m^4=[110]$	$(\sin\theta, -\cos\theta\ , -\sqrt{2}\ )/\sqrt{3}$ $(\cos\theta, \sin\theta,\ 0)$
5- $n^5=(\bar{1}1\bar{1})$ $m^5=[0\bar{1}\bar{1}]$	$(\sin\theta, -\cos\theta\ , -\sqrt{2}\ )/\sqrt{3}$ $(-\cos\theta + \sqrt{2}\sin\theta, -\sin\theta - \sqrt{2}\cos\theta\ ,\ 1)/2$
6- $n^6=(\bar{1}1\bar{1})$ $m^6=[10\bar{1}]$	$(\sin\theta, -\cos\theta\ , -\sqrt{2}\ )/\sqrt{3}$ $(\cos\theta + \sqrt{2}\sin\theta, \sin\theta - \sqrt{2}\cos\theta\ ,1)/2$
7- $n^7=(\bar{1}\bar{1}1)$ $m^7=[\bar{1}0\bar{1}]$	$(-\sqrt{2}\cos\theta - \sin\theta\ ,\ -\sqrt{2}\sin\theta + \cos\theta,\ 0)/\sqrt{3}$ $(-\cos\theta + \sqrt{2}\sin\theta, -\sin\theta - \sqrt{2}\cos\theta\ ,\ -1)/2$
8- $n^8=(\bar{1}\bar{1}1)$ $m^8=[0\bar{1}\bar{1}]$	$(-\sqrt{2}\cos\theta - \sin\theta\ ,\ -\sqrt{2}\sin\theta + \cos\theta,\ 0)/\sqrt{3}$ $(-\cos\theta + \sqrt{2}\sin\theta, -\sin\theta - \sqrt{2}\cos\theta\ ,\ 1)/2$
9- $n^9=(\bar{1}\bar{1}1)$ $m^9=[1\bar{1}0]$	$(-\sqrt{2}\cos\theta - \sin\theta\ ,\ -\sqrt{2}\sin\theta + \cos\theta,\ 0)/\sqrt{3}$ $(0,\ 0,\ 1)$
10- $n^{10}=(1\bar{1}\bar{1})$ $m^{10}=[110]$	$(\sin\theta, -\cos\theta, \sqrt{2}\ )/\sqrt{3}$ $(\cos\theta, \sin\theta,\ 0)$
11- $n^{11}=(1\bar{1}\bar{1})$ $m^{11}=[\bar{1}0\bar{1}]$	$(\sin\theta, -\cos\theta, \sqrt{2}\ )/\sqrt{3}$ $(-\cos\theta + \sqrt{2}\sin\theta, -\sin\theta - \sqrt{2}\cos\theta\ ,\ -1)/2$
12- $n^{12}=(1\bar{1}\bar{1})$ $m^{12}=[011]$	$(\sin\theta, -\cos\theta, \sqrt{2}\ )/\sqrt{3}$ $(\cos\theta + \sqrt{2}\sin\theta, \sin\theta - \sqrt{2}\cos\theta\ ,-1)/2$

APPENDIX B

MATRIX AND VECTOR REPRESENTATIONS OF TENSORS

This Appendix is devoted to vectors and tensors used in the implementation of algorithms described in the third and fourth chapter as the a user material subroutines "UMAT" for FE program ABAQUS.

- The shear modulus G is related to elastic modulus E and Poisson's ratio υ by
  $G = \frac{E}{2(1+\upsilon)}$.
- The Bulk modulus k is given by:
  $k = \frac{E}{3(1-2\upsilon)}$,
  where E is the elastic modulus and υ is Poisson's ratio
- Stress and strain $[4\times 1]$ vectors **S** and **E** are represented by

$$S_{ij} = \begin{bmatrix} s_{11} \\ s_{22} \\ s_{33} \\ s_{12} \end{bmatrix},$$

$$E_{ij} = \begin{bmatrix} e_{11} \\ e_{22} \\ e_{33} \\ e_{12} \end{bmatrix},$$

where the usual assumption of symmetry reducing nine components of a tensor to four components.

- The material matrix C is given in terms of elastic modulus E and Poisson's ratio υ by

$$C = \frac{E(1-\upsilon)}{(1+\upsilon)(1-2\upsilon)} \begin{bmatrix} 1 & \frac{\upsilon}{1-\upsilon} & \frac{\upsilon}{1-\upsilon} & 0 \\ \frac{\upsilon}{1-\upsilon} & 1 & \frac{\upsilon}{1-\upsilon} & 0 \\ \frac{\upsilon}{1-\upsilon} & \frac{\upsilon}{1-\upsilon} & 1 & 0 \\ 0 & 0 & 0 & \frac{1-2\upsilon}{2(1-\upsilon)} \end{bmatrix}$$

- The following constant matrices used in the evaluation of the consistent tangent modulus are formed:
  - the 3×3 identity matrix is represented as 4×1

$$1 = \begin{bmatrix} 1 \\ 1 \\ 1 \\ 0 \end{bmatrix}$$

  - the fourth order identity matrix

$$I = \begin{bmatrix} 1 & 0 & 0 & 0 \\ 0 & 1 & 0 & 0 \\ 0 & 0 & 1 & 0 \\ 0 & 0 & 0 & 1 \end{bmatrix}$$

  - The outer product of the second identity

$$\mathbf{1} \otimes \mathbf{1} = \begin{bmatrix} 1 & 1 & 1 & 0 \\ 1 & 1 & 1 & 0 \\ 1 & 1 & 1 & 0 \\ 0 & 0 & 0 & 0 \end{bmatrix}$$

  - the deviatoric identity

$$\mathbf{I}_{dev} = \begin{bmatrix} 1 & 0 & 0 & 0 \\ 0 & 1 & 0 & 0 \\ 0 & 0 & 1 & 0 \\ 0 & 0 & 0 & 1 \end{bmatrix} - \frac{1}{3} \begin{bmatrix} 1 & 1 & 1 & 0 \\ 1 & 1 & 1 & 0 \\ 1 & 1 & 1 & 0 \\ 0 & 0 & 0 & 0 \end{bmatrix}$$

BIBLIOGRAPHY

[1] ABAQUS Theory Manual, *Version 5.2, 1990, Hibbit Karllsson and Sorensen, Inc, Providence.*

[2] ABAQUS User Manual, *Version 5.2, 1990, Hibbit Karllsson and Sorensen, Inc, Providence.*

[3] S. Ahzi, R. J. Asaro, B. J. Lee, "On the plasticity of low symmetry crystals lacking five independent slip systems", *Mechanics of Materials, vol. 20, p. 1, 1995.*

[4] E. C. Aifantis, "On the microstructural origin of certain inelastic models", *ASME, J. Eng. Mat. Tech., Vol. 106, P. 326, 1984.*

[5] L. Anand and W. A. Spitzig, "Initiation of localized shear bands in plane strain", *J. Mech. Phys. , vol. 28, p. 113, 1980.*

[6] L. Anand, "Constitutive equations for hot working of metals", *Int. J. Plasticity, vol. 1, p. 213, 1985.*

[7] J. H. Argyris, L. E. Vaz, and K. J. William, "Improved solution methods for elastic rate problems", *Computer Methods In Applied Mechanics And Engineering, vol. 16, p. 231, 1978.*

[8] R. J. Asaro and J. Rice, "Strain localization in ductile single crystals", *J . Mech. Phys. Solid, vol. 25, p. 309, Pergamon Press, 1977.*

[9] R. J. Asaro, "Crystal plasticity", *J. App. Mech., vol. 50, p. 921, 1983.*

[10] R. J. Asaro and A. Needleman, "Texture development and strain hardening in rate dependent polycrystals", *Acta Metal., vol. 33, p. 923, 1985.*

[11] R. J. Asaro, M. Doa, "Localized deformation modes and non-Schmid effect in crystalline solids. Part I", Critical Conditions of Localization, *Mechanics of Materials, vol. 23, p. 71, 1996.*

[12] R. J. Asaro, M. Doa, "Localized deformation modes and non-Schmid effect in crystalline solids. Part II", Deformation Patterns, *Mechanics of Materials, vol. 23, p. 103, 1996.*

[13] R. Becker, J. F. Butler, Jr. H. Hu, and L. A. Lalli, "Analysis of an aluminum single crystal with unstable initial orintation (001)[110] in channel die compression", *Metal. Trans., vol. 22A, p. 45, 1991.*

[14] R. Becker, "Analysis of texture evolution in channel die compression- I. Effects of grain integration", *Acta Metal., vol. 39, p. 1211, 1991.*

[15] R. Becker, "An Analysis of shear localization during bending of polycrystalline sheet", *J. Appl. Mech., vol. 59, p. 491, 1992.*

[16] C. E. Beevers, "On thermodynamics and stability of continuous media, in: W. Fiszdon, K. Wilmanski (eds); Mathematical models and methods in mechanics", *Banach Center Publ., vol. 15, PWN, Warswa, p. 49, 1985.*

[17] C. A. Bronkhorst, S. R. Kalidindi, and L. Anand, "An experimental and analytical study of the evolution of crystallographic texturing in (fcc) materials", *Presented at International Conference on Texture of Materials, sept .,1990.*

[18] C. A. Bronkhorst, S. R. Kalidindi and L. Anand, "Polycrystalline plasticity and the evolution of crystallographic texture in fcc metals", *Phil Trans. R. Soc. Lond., p 443, 1992.*

[19] S. Brown, K. Kim and L. Anand, "An internal variable constitutive model for hot working of metals", *Int. J. Plast. , vol. 5, p. 95, 1985.*

[20] J. Casey, "On finitely deforming rigid-plastic materials", *Int. J. Plasticity, vol. 2, p. 247, 1986.*

[21] J. Casey, and P. M. Naghdi, "A Remark on the use of the decomposition F=EP in plasticity", *Trans. ASME, vol. 47, p. 672, 1980.*

[22] J. Casey, and P. M. Naghdi, "On the characterization of strain-hardening in plasticity", *J. App. Mech., vol. 48, p. 258, 1981.*

[23] Y. W. Chang and J. Asaro, "An experimental study of shear localization in aluminum-copper single crystals", *Acta. Metal., Vol. 29, P. 241, 1981.*

[24] A. Chandra, and S. Mukherjee, "Afinite element analysis of metal forming problems with an elastic-viscoplastic material model", *Int. J. for Numerical Methods in Eng. , vol. 20, p. 1613, 1984.*

[25] H. Cleveringa, E. Van der Giessen, A. Needleman, "A discrete dislocation analysis of bending", *Journal of Plasticity, Vol. 15, P. 837, 1999.*

[26] I. Cormean, "Numerical stability in Quasi-static Elasto-viscoplasticity" *Int. J. Numerical Methods in Eng. , vol. 9, p. 109, 1975.*

[27] Y. F. Dafalias, "Co-rotational rates for kinematic hardening at large plastic deformation", *J. Appl. Mech., vol. 50 , p. 561, 1983.*

[28] Y. F. Dafalias, and M. M. Rashid, "The effect of plastic spin on anisotropic material behavior", *Int. J. Plasticity, vol. 5, p. 227, 1989.*

[29] H. E. Deve and R. J. Asaro, "The development of plastic failure modes in crystalline mateials: shrear bands in (fcc) polycrystals" , *Metall . Trance, 20A, vol. 5, p. 59-593,1989.*

[30] J. K. Dienes, "On the analysis of rotation and stress rate in deforming bodies", *Acta Mechanica, vol. 32, p. 217, 1979.*

[31] H. Eggers and B. Kroplin, "Yielding of plates with hardening and large deformation", *Int. J. Numer. Methods Eng., vol. 12 , p. 739, 1978.*

[32] J. D. Embury, A. Korbel, V.S. Raghunathan and J. Rys, "Shear band formation in colled rolled Al-Cu single crystals", *Acta Metal., vol. 32, p. 1883, 1984.*

[33] Y. Estrin, L. P. Kubin, "Local strain hardening and non-uniformity of plastic deformation", *Acta metal., vol. 34, p. 2455, 1985*

[34] P. Gay, "The crystalline state: an introduction", *Oliver and Boyed, Edinburgh, 1970.*

[35] A. E. Green, P. M. Naghdi, "Plasticity theory and multipolar continuum mechanics", *Arch. Rat. Mech. Anal., vol. 1, p21, 1965.*

[36] S. V. Harren, H. E. Deve and R. J. Asaro, "Shear band formation in plane strain compression", *Acta Metal., vol. 36, p. 2435, 1988.*

[37] S. V. Harren, and R. J. Asaro, "Nonuniform deformations in polycrystals and aspects of the validity of the Taylor model", *J. Mech. Phys. Solids, vol. 37, p. 191, 1989.*

[38] S. V. Harren, T. C. Lowe, R. J. Asaro, and A. Needleman, "Analysis of large-strain shear in rate-dependent face-centered cubic polycrystals: correlations of micro- and macro-mechanics", *Phil. Trans. R. Soc. Lond. A328, p. 443, 1989.*

[39] M. Hatherly and A. S. Malin, "Shear bands in deformed metals", *Scripta Metall., vol. 18, p. 449, 1984.*

[40] R. Hill, "The essential structure of constitutive laws for metal composites and polycrystals", *J. Mech. Phys. Solids, vol. 15, p. 779, 1967.*

[41] R. Hill and J. R. Rice, "Constitutive analysis of elastic - plastic crystals at arbitrary strain", *J. Mech. Phys. Solids, vol. 20, p. 401, 1972.*

[42] R. Hill, J. R. Rice, "Elastic potentials and the structure of inelastic constitutive laws", *SIAM J. Appl. Math., vol. 25, p. 448, 1973.*

[43] A. Huber, E. Schmid, "Bestimmung der elastischen eigenschaften quasiisotroper vielkristalle durch mittelung", *Helv. Phys. Acta, vol. 7, p. 620, 1934.*

[44] T. Hughes, and J. Winget, "Finite rotation effect in numerical integration of rate constitutive equations arising in large-deformation analysis", *Intl. J. for Numerical Methods in Eng., vol. 15, p. 1862, 1980.*

[45] B. K. Kad, S. E. Schoenfeld, R. J. Asaro, C. G. McKamey, V. K. Sikka, "Deformation textures in Fe_3Al alloys: an assessment of dominant slip system activity in the 900-1325 k temperature range of hot working", *Acta Materialia, vol.45, p. 1333, 1997.*

[46] M. Kleiber, and B. Raniecki, "Elastic-Plastic materials at finite strain, in: A. Sawczuk, and G. Bianchi (eds.); Plasticity Today; Modeling, Methods and Applications", *Elsevier, p. 3, 1985.*

[47] A. Korbel, "The real nature of shear bands plastons?", *In proc. Intl. Symposium on Plastic Instability, Presses de l` Ecole nationale des ponts et chausees , Paris, p.325, 1985.*

[48] A. Korbel, J. D. Embury, M. Hatherly, P. L. Martin, and H. W. Erbsloh, "Microstructural aspects of strain localization in Al-Mg Alloys", *Acta. Metal., vol. 34, p. 1999,1986.*

[49] R. D. Krieg and D. B Krieg, "Accuracies of numerical solution methods for elastic-perfectly plastic model", *ASME Journal of Pressure Vessel Technology ,vol. 99, p. 510, 1977.*

[50] J. Kratochvil, "Finite strain theory of crystalline elastic-inelastic materials", *J. Appl. Phys., vol. 42, p. 1104, 1971.*

[51] J. Kratochvil, "On a finite strain theory of elastic-plastic materials", *Acta. Mech., vol. 16, p. 127, 1973.*

[52] E. Kroener, "Zur plastischen Verformung des Vielkristalls", *Acta Metall., vol. 9, p. 155.*

[53] T. G. Langdon, "Regimes of plastic deformation", *Academic Press Inc., 1985.*

[54] E. H. Lee, "Elastic-plastic deformation at finite strains", *J. Appl. Mech., vol. 36, p. 1, 1969.*

[55] J. Lemond, R. J. Asaro, and A. Needleman, "A numerical study of localized deformation in Bi-crystals", *Mech. materials, vol. 4, p. 417, 1985.*

[56] B. Loret, "On the effect of plastic rotation in the finite deformation of anisotropic elastic-plastic materials", *Mech. of Materials, vol. 2, p. 287, 1983.*

[57] V. A. Lubarda and E. Lee, "A correct definition of elastic and plastic deformation and its computational significance", *J. Appl. Mech., vol. 48, p. 35, 1981.*

[58] A. M. Lush, G. Weber and L. Anand, "An implicit time-integration procedure for a set of integral variable constitutive equations for isotropic elasto-viscoplasticity", *Int. J. Plasticity, vol. 5, p. 521-549, 1989.*

[59] J. Mandel, "Plasticite classique et viscoplasticite", *Courses and Lectures, No. 97, International Center for Mechanical Sciences, Udine, Springer, N.Y., 1971.*

[60] K. A. Mathur, and P. R. Dawson, "On modeling the development of crystallographic texture in bulk forming processes", *Int. Journal of Plasticity, vol. 5, p. 67, 1989.*

[61] J. Meixner, "Thermodynamische theorie der elastischen relaxation", *Zeitschrift fur Naturforschung, Bd. 9a, p. 654, 1954.*

[62] A. K. Miller, and C. F. Shih, "An improved method for numerical integration of constitutive equations of the work-hardening - recovery type", *ASME Journal of Engineering Materials and Technology, vol. 99, p. 275, 1977.*

[63] R. V. Mises, "Mechanik der plastischen formanderung von kristallen", *Zeitschrift fur angewandte Mathematik and Mechanik, vol. 8, p. 161, 1928.*

[64] A. Needleman, V. Tvergaard, "Analysis of a brittle-ductile under dynamic shear bending", *Int. J. of Solids and Structure, vol. 32, p. 2571, 1995.*

[65] A. Needleman, and M. Ortiz, "Effect of boundaries and interfaces on shear-band localization", *Int. J. of Solids and Structure, vol. 28, p. 859, 1991.*

[66] S. Nemat-Nasser, "Decomposition of strain measures and their rates in infinite deformation elastoplasticity", *Int. J. Solids Structure, vol. 15, p. 155, 1979.*

[67] S. Nemat-Nasser, and T. Iwakuma, "Finite elastic-plastic deformation of composites, in: Z. Hashin, and C. T. Herakovich", *Mechanics of Composite Materials , Recent Advances, Pergamon Press, vol. 47, p. 47, 1983.*

[68] H. Neuhauser, "Slip-line formation and collective dislocation motion", *Dislocations in Solids, F.R.N. Nabarro, (Ed.) North-Holland, Amsterdam, p. 319-440, vol. 6, 1983.*

[69] M. Ortiz, "Computational micro-mechanics", *Comp. Mech., Vol. 18, P. 321, 1996.*

[70] J. E. Paulun, and R. B. Pecherski, "Study of corotational rates for kinematic hardening in finite deformation plasticity", *Arch. Mech., Vol. 35, P. 6, 1985.*

[71] J. E. Paulun, and R. B. Pecherski, "On the application of the plastic spin concept for the description of anisotropic hardening in finite deformation plasticity", *Int. J. Plasticity, vol. 3, p. 303, 1987.*

[72] R. B. Pecherski, "Modelling of large plastic deformation on the mechanism of micro -shear banding. Physical foundation and theoretical description in plane strain", *Arch. Mech, vol. 44, p. 563, Warszawa 1992.*

[73] R. B. Pecherski, "A model plastic flow with an account of micro-shear banding", *ZAMM, 72, pp. T250-T254, 1992.*

[74] D. Peirce, R. J. Asaro and A. Needleman, "An analysis of non-uniform and localized deformation in ductile single crystal", *Acta. Metall., vol. 30, p. 1087, 1982.*

[75] D. Peirce, R. J. Asaro, and A. Needleman, "Material rate dependence and localized deformation in crystalline solids", *Acta. Metal., vol. 31, p. 1951, 1983.*

[76] D. Peirce, C. F. Shih, and A. Needleman, "A tangent modulus method for rate dependent solids", *Computers and Structures, vol. 18, p. 875, 1984.*

[77] P. Perzyna, "Fundamental problems in viscoplasticity", *Advan. Appl. Mech., Vol. 9, P. 243, 1966.*

[78] P. Perzyna, "Coupling of dissipative mechanisms of viscoplastic flow", *Arch. Mech., vol. 29, p. 607, 1977.*

[79] C. N. Reid, "Deformation geometry for materials scientists", *Pergamon Press, 1973.*

[80] J. Gil. Sevillano, P. Van Houtte and E. Aernoudt, "Large strain work hardening and textures", *Progress in Material Science, vol. 25, p. 69, Pergamon Press, 1981.*

[81] G. Sachs, "Zur ableitung einer fliessbedingung", *Z. Verein. Deut. Ing., vol. 72, p. 734, 1928.*

[82] E. Schmid, "Uber die schubverfestigung von einkristallen bei plastischer deformation", *Z. F. Physik, vol. 40, p. 54, 1927.*

[83] C. F. Shih, H. G. Delorenzi, and A. K. Miller, "A stable computational scheme for stiff time-dependent constitutive equations", *In Proceedings of the 4th International Conference on Structural Mechanics in Reactor Technology, paper L 2/2, 1977.*

[84] J. C. Simo and R. L. Taylor, "Consistent tangent operators for rate-independent elastoplasticity", *Comput. Meths. Appl. Eng., vol. 48, p. 101,1985.*

[85] J. C. Simo, J. G. Kennedy and S. Govindjee, "Non-smooth multisurface plasticity and viscoplasticity, loading /unloading condition and numerical algorithms", *Int. J. Numer. Methods Eng., vol. 26, p. 2161, 1988.*

[86] J. C. Simo, "A framework for finite strain elastoplasticity based on maximum plastic dissipation and the multiplicative decomposition. Part II: Computational aspects", *Computer Methods in Applied Mechanics and Engineering, vol. 68, p. 1, 1988.*

[87] G. I. Taylor, "Notes on the Navier effect", *Proc. Roy. Soc. Lond., vol. A116, p39, 1927.*

[88] G. I. Taylor, and M. A. Quinney, "The plastic distortion of metals", *Phil.Trans., Roy. Soc. London, A230, P. 323, 1932.*

[89] G. I. Taylor, "Mechanism of plastic deformation", *Proc. Roy. Soc. (London), A145, p. 363, 1934.*

[90] G. I. Taylor, and H. Quinney, "The latent energy remaining in a metal after cold working", *Proc. Roy. Soc. (London), Ser. A143, p. 307, 1934.*

[91] G. I. Taylor, Stephen Timoshenko 60th anniversary volume, *Lessels, J. M. (ed.), Macmillan , New York, 218, 1938.*

[92] G. I. Taylor, "Plastic strain in metals", *J . Inst . Metals , vol. 62, p. 307, 1938.*

[93] J. C. Telles, and C. A. Brebbia, "Elastic /viscoplastic problems using boundary elements", *International Journal of Mechanical Science, vol. 24 , p. 605, 1982.*

[94] D. Teramoto, Y. Tomita, H. M. Zbib, "Finite element simulation of localization behavior of crystals under plane strain condition", *Proc. JSME, vol. 1, p. 625, 1996.*

[95] V. Tvergaard, A. Needleman, "Shear band development in polycrystals", *Proc. R. Soc. Lond., vol. A443, p. 547, 1993.*

[96] V. Tvergaard, "Modelling of defects and fracture mechanics", *ed. G. Herrman, Springer-Verlag, Vienna, p. 119, 1993.*

[97] P. Van Houtte and F. Wanger, "Development of textures by slip and twinning", *Academic Press, Inc., 1985.*

[98] O. Watanabe, H. M. Zbib and E. Takenouchi, "Crystal plasticity: micri-shear banding in polycrystals using voronoi aessellation", *Int. J. Plasticity, in vol. 12 , p. 61, 1997.*

[99] G. Weber and L. Anand, "Finite deformation constitutive equations and a time integration procedure for isotropic hyperelastic-viscoplastic solids", *Comput. Appl. Mech. Eng., vol. 79, p. 173, 1990.*

[100] M. Wilkins, "Calculation of elastic - plastic flow", *Methods of Computational Physics, 3, Academic Press, New York, 1964.*

[101] K. J. William, "Numerical solution of inelastic rate problems", *Computers and Structures, vol. 8, p. 511, 1978.*

[102] R. O. Williams, "Shear textures in copper, brass, aluminum, iron, and zirconium", *Trans. Met. Soc. AIME 224, p. 129, 1962.*

[103] H. M. Zbib, "Instabilities and size effects in plasticity: Continuum and dislocation approach, in: Material instabilities in solids, ed. R. Borst and E. Van der Giessen and R. de. Borst. (IUTAH symposium on material instabilities) Delft, June 1997", *Wiley & Sons, p. 473, 1998.*

[104] H. M. Zbib, E. C. Aifantis, "On the localization and post-localization behavior of plastic deformation. Part I: on the initiation of shear band. Part II: On the evolution and thickness of shear bands. Part III: On the structure and velocity of the Portevin-Le Chatelier band", *Res Mechanica, vol. 23, p. 261, 1988*.

[105] H. M. Zbib, E. C. Aifantis, "On the structure and width of shear bands in finite elasto-plastic deformation", *in: Anisotropy and localization of plastic deformation, J. P. Boehler and A. H. Khan, eds., Elsevier Appl. Sci., p. 99, 1991.*

[106] H. M. Zbib, "Size effects and shear banding in visco-plasticity with kinematic hardening", *in: Material instabilities, R. Batra and H. M. Zbib, eds., AMD-VOL 183, MD-VOL 50, ASME, NY, p. 19, 1994.*

[107] H. T. Zhu, H. M. Zbib, and E. C. Aifantis, "Strain gradients and continuum modeling of size effect in metal matrix composites", *Acta Mechanica, vol. 121, p. 165, 1997.*

[108] M. Zhou, A. Needleman and R. J. Clifton, "Finite element simulations of shear localization in plate impact", *J. Mech. Phys. Solids, vol. 42, p. 423, 1994.*

[109] O. C. Zienkiewiez, and I. C. Comeau , "Viscoplasticity ,plasticity and creep in elastic solids –A unified numerical solution approach", *Intl. J. Numerical Methods in Eng., vol. 8, p. 821, 1974.*

[110] R. M. Zirin and E. Kremp, "A finite element time-integration method for the theory of viscoplasticity based on infinitesimal total strain", *ASME Journal of Pressure Vessel Technology , vol. 104, p. 136, 1982.*